FORMABILITY OF ADVANCED HIGH STRENGTH STEEL TUBES IN TUBE BENDING AND HYDROFORMING

by

Mikhail Sorine

A thesis
presented to the University of Waterloo
in fulfillment of the
thesis requirement for the degree of
Master of Applied Science
in
Mechanical Engineering

Waterloo, Ontario, Canada, 2007

I hereby declare that I am the sole author of this thesis. This is a true copy of the thesis, including any required final revisions, as accepted by my examiners.

I understand that my thesis may be made electronically available to the public.

Abstract

An investigation of the tube hydroforming process is conducted in order to understand the effect of pre-bending operation on formability in tube hydroforming and assess the application of the newly developed Extended Stress-Based Forming Limit Curve (XSFLC) method to the prediction of failure in tube hydroforming. Two sets of experiments on straight tube hydroforming and pre-bent tube hydroforming were conducted on tubes manufactured from three steel grades, namely DDQ, HSLA350 and DP600, which represent mild steel, high strength steel and advanced high strength steel, respectively. All tubes had the same outer diameter of 76.2 mm and the same nominal wall thickness of 1.8 mm, which enabled direct assessment of the effect of material strength on formability in tube hydroforming. For pre-bent tube hydroforming the tubes were bent to 90 degrees before hydroforming. The effect of the increased axial compressive load, termed the end-feed load, on tube formability in hydroforming was investigated.

All experiments were simulated using the explicit dynamic finite element code LS-DYNA in order to investigate the accuracy of numerical predictions in the tube hydroforming process. The numerical simulations, validated using the experimental data, were then utilized to investigate the prediction of necking in straight and pre-bent tube hydroforming using the XSFLC method.

The formability, burst pressure and corner-fill expansion in hydroforming of the pre-bent tubes was considerably less than that exhibited in hydroforming of the straight tubes. In both straight and pre-bent tube hydroforming, the application of the end-feed load postponed failure and significantly increased internal pressure and corner-fill expansion at burst.

The finite element models accurately predicted the results of the tube bending and tube hydroforming experiments. The straight tube hydroforming simulations, validated using the experimental results, enabled accurate prediction of the failure location and tube internal pressure at the onset of necking using the XSFLC method. In order to obtain the XSFLC for each alloy, strain-based FLCs were calibrated using the results of tube free expansion tests. The results of the tube free expansion tests and corresponding numerical simulations also served to validate the tube material properties for the FE models. Straight tube hydroforming simulations were utilized to investigate the effect of friction between the tube and the die on the hydroforming process parameters and necking predictions using the XSFLC method. The validated pre-bent tube hydroforming simulations captured the trends in the increase of tube internal pressure at the onset of necking with the increase of end-feed load using the XSFLC method.

Acknowledgements

I would like to thank my supervisor, Prof. Michael Worswick, for an opportunity to work on this project, his guidance through the research work and his help in setting up a positive start for my research and engineering career in Canada. I am grateful to Michael for his patience at the beginning, during my transition period, which was not easy for me. I would also like to thank Hari Simha for his advice and collaboration in the XSFLC part of my research work. I thank Dino Oliveira for his help with the experimental work and for editing my first technical paper. I wish to thank Rassin Grantab, Alex Bardelcik and Bruce Williams for their help in the labs. I would also like to acknowledge technical support from the lab technicians Ekhard Budziareck, Howard Barker, Richard Gordon, Tom Gawel and Andy Barber. I would like to thank my friend Oleg and all my office-mates.

I am grateful for the financial support provided to me by the Ontario Graduate Scholarship and the President of the University of Waterloo Scholarship. My research project was made possible through the support of the Auto21 project, the Canadian Auto21 Networks of Centers of Excellence, Dofasco Inc., Eagle Precision Technologies, D.A. Stuart, Nova Tube, Stelco and General Motors of Canada. I would like to thank Isadora van Riemsdijk and Bruce Farrand of Dofasco Inc. for their enthusiast support in every aspect of our collaboration within my research work and for sharing their ideas with me.

Finally, I would like to thank my family for their understanding and my friends outside the university, who made my transition into Canadian period of my life smoother and much more enjoyable.

To the memory of a metal forming specialist, a great man and my grandfather

Grigory Iosifovich Khesin

Table of Contents

List of tables

List of figures

Chapter 1
Introduction

The efficiency of the consumption of energy and resources is one of the main driving forces of the economy today. In industry it requires design and manufacturing improvement, reduction of environmental risks and waste, decrease of power losses, reuse and recycling. Being one of the world manufacturing leaders, the automotive industry has to constantly develop new methods and technology to increase its efficiency and global competitiveness. One of the ways to decrease fuel consumption, emissions and amount of utilized material is auto body weight reduction. Every 10% decrease of auto body weight contributes to an increase in fuel economy of 6%-8% [1]. Weight reduction can be realized through more extensive employment of lightweight structures and adaptation of higher strength/lower weight materials and alternative manufacturing processes [2,3]. Mild steels, traditionally used in automotive part production, are now often substituted by aluminum, magnesium, high-strength steel and composite materials.

Tube hydroforming has recently found a wide application in production of auto structures, replacing conventional stamping and forging operations. Tube hydroforming is a process of forming metal tube into complex shapes within a die cavity using simultaneous application of internal pressure and axial load. Although the first research on tube hydroforming dates back to 1940s [4], only recent advancements in machine design and controls have made it an economic alternative to various stamping processes [1,2,5,6]. In automotive applications it has only been for a decade [4,7].

A schematic diagram of the tube hydroforming process is shown in Figure 1. A tube is first enclosed within a die (Figure 1a) and end-plugs are inserted into both ends to maintain sealing for internal pressurization (Figure 1b). The end-plugs can be mounted on actuators, reacting the internal pressure and exerting the axial load on the ends of the tube. Under the action of the internal pressure and axial load, the tube deforms into the shape of the die (Figure 1c).

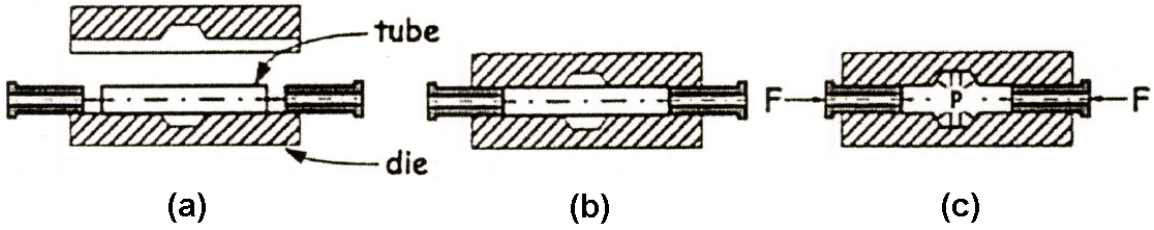

Figure 1: Schematic of a tube hydroforming process [8]

The main applications of tube hydroforming, currently fall within the automotive, aircraft, appliance and plumbing industries, as summarized by Koc *et al.* [1,7], Ahmetoglu *et al.* [5], Xia [6] and Dohmann *et al.* [9]. Automotive applications include [1,5-7, 9]:

- Exhaust system parts: engine tubes, catalytic converters, pressure tubes, tail pipes, connectors and manifolds;
- Chassis parts: frame rails, engine sub-frames (cradles), roof rails and bows, instrument panels, rear axle frames and radiator frames;
- Engine and power train components: suspension cross members, hollow camshafts, drive shafts and gear shafts;
- Body and safety parts: windshield parts, A/B/C pillars, space frame components, seat frames and shock absorber housings.

The benefits of tube hydroforming, compared to conventional stamping and welding processes, include part consolidation, weight reduction, improved stiffness and strength, tighter dimensional tolerances, fewer secondary operations and reduced cost [1,2,4-16]. To better illustrate the benefits of tube hydroforming over conventional stamping operations, a comparison of cost, weight and numbers of parts required to produce the engine cradle shown in Figure 2b is summarized in Figure 2a [13].

Part type	No. of parts	Mass (kg)	Tool cost ($)	Part cost ($)
1) Stamping (steel)	34	24.56	5359 090	51.00
2) Hydroforming (steel)	30	20.50	3721 636	42.83
3) Hydroforming (aluminum, cold)	30	14.41	3891 727	73.17
Savings	4 parts	(2:1)=16% (3:1)=41%	(2:1)=30% (3:1)=27%	(2:1)=16% (3:1)=−43%

(a)

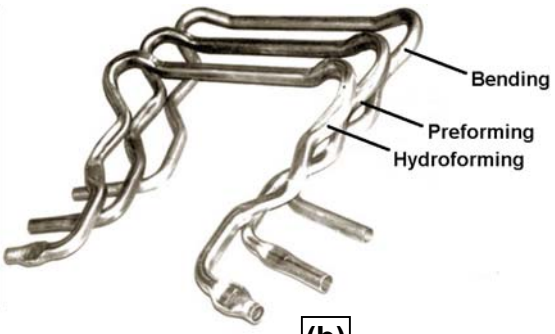

(b)

Figure 2: (a) comparison of hydroforming and stamping processes for an engine cradle (1 – steel stamping, 2 – steel hydroforming, 3 – aluminum hydroforming) [1]; (b) hydroforming of engine cradle [13]

Some of the disadvantages of tube hydroforming process include slow cycle time and expensive equipment [16]. The novelty of tube hydroforming technology compared to conventional metal forming processes represents another drawback due to an insufficient existing knowledge base for process and tool design [2,4,5,11,15,17]. Therefore, a growing need for the expertise that would satisfy industrial demands and establish systematic approaches exists in this area [2,5,7,9-1,19-23]. Ongoing research of the hydroforming process currently spans full range of problems including determination of tube properties; optimization of process parameters and pre-forming operations; investigation of forming limits for different failure modes; characterization of friction conditions and their simulation [1,11,1,18].

In the early days, hydroforming was mainly a one step process, producing a final part in a single operation. Nowadays, a sequence of bending, pre-forming and hydroforming is commonly utilized to obtain geometrically complicated large parts (Figure 2b) [1,8,9].

Hydroforming try-outs require hard tooling and subsequent major improvements are expensive and time-consuming [2,5]. Therefore, finite element analysis (FEA) of tube hydroforming through the sequence of bending, pre-forming and hydroforming simulations has become a standard practice utilized to optimize design and process parameters and obtain accurate predictions of formability, thickness and strain distributions [2,5-7,9,1-15,17,18,22,23,26-32].

An overview of available published results concerning various aspects of tube hydroforming is presented in the current chapter. Advanced high strength steel tube materials and methods of their characterization, the effect of material properties, friction and process parameters on tube bending and hydroforming operations and particular tube hydroforming applications are discussed in detail. A separate section is dedicated to the discussion of the application of tube failure prediction methods based on forming limit curves.

1.1 Tube material and its characterization

General guidelines for the selection of material for successful tube hydroforming are summarized by Koc *et al.* [7,10] and include high and uniform elongation, high strain-hardening exponent, low anisotropy, close mechanical and surface properties of the seam weld relative to the base material, good surface quality and close dimensional tolerances. The following discusses various aspects of tube materials pertinent to tube hydroforming.

1.1.1 Advanced High Strength steels

New generations of high strength steels (HSS) and multi-phase advanced high strength steels (AHSS) provide an opportunity to address the industrial demand for light-weight structures. At the same time, their utilization requires broad research and thorough optimization of corresponding forming processes due to the inherent lower formability of these materials. A schematic summary of steel classification according to its strength, formability (total elongation) and metallurgical designation is shown in Figure 3 and provides insight into the benefits of new AHSS over more conventional HSS and mild steels. It is evident that in general for a given strength AHSS have higher ductility compared to HSS.

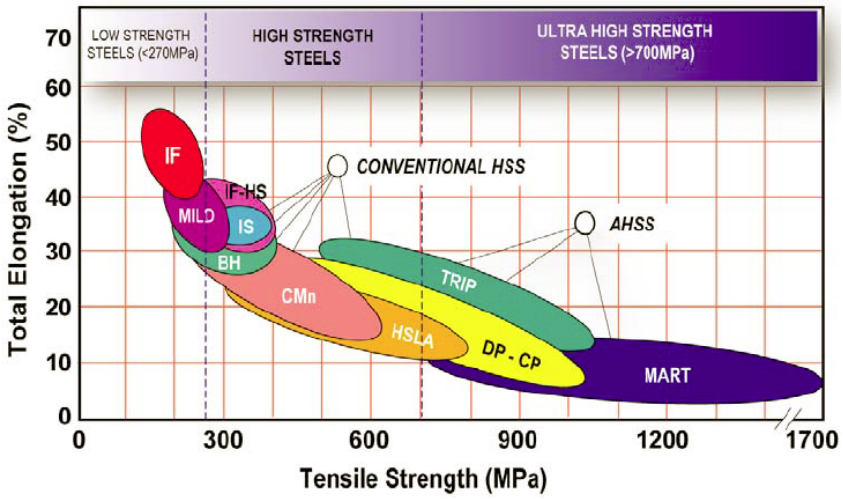

Figure 3: Strength-elongation relationship for low strength, conventional high strength and advance high strength steels [40]

Dual phase steel is an example of AHSS that consists of soft continuous ferrite matrix containing a hard martensite second phase in the form of islands [40]. The soft ferrite phase provides higher ductility, while the harder martensite islands increase the strength and promote the higher work-hardening rate exhibited by AHSS. To better illustrate these effects, a comparison of quasi-static stress-strain behavior of HSLA and DP600 is presented in Figure 4

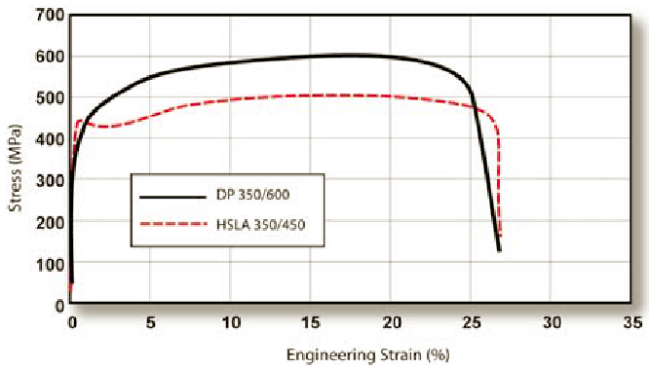

Figure 4: Quasi-static stress-strain behavior of HSLA and DP600 steels [40]

Together with higher elongation at given strength, the advantages of DP steels compared to conventional HSS include increased energy absorption in a crash event; higher n-values at strain levels below 5% which promote more uniform deformation; and better fatigue capabilities for a given yield strength level [40]. At the same time, the drawbacks of DP steels compared to HSLA include higher springback and curl, both of which increase with yield strength, requiring modification of forming tools and process parameters.

1.1.2 Tube material property determination

Tube material properties, such as yield and ultimate strength, ductility, anisotropy, composition, weld type and thickness variation, affect hydroforming process parameters, deformation capability and the properties of the final part. They are highly sensitive to the tube rolling, welding and annealing operations utilized in tube making process [35]. For the same steel grade, tube material properties vary from manufacturer to manufacturer, from coil to coil produced by the same manufacturer and within the coil from the lead to the trail and across the width [36]. The robustness of the tube hydroforming process, post-processing and final part performance to these variations should be evaluated at the component design stage [11].

Due to the rolling, welding and sizing processes during the tube making process, the tube material properties are different from the properties of the source sheet [5,10,25,33,35]. Levy *et al.* [35] compared sheet and tube material properties for AKDQ and HSLA steels. The tube fabrication process decreased the tube material n-value by 10%-20% and uniform elongation by 2%-4% strain, compared to the corresponding sheet material properties of both alloys. The effective pre-strain due to tube fabrication was 2%-4% and varied with respect to the direction in tube material. This study confirms that material properties should be measured directly from the tube material in order to account for the effect of the tube making process [7,10,21,22,33].

To obtain tube material properties Oliveira *et al.* [23], Bardelcik *et al.* [21,22] and Dyment [41] utilized quasi-static uni-axial tensile tests on specimens machined along the longitudinal direction of the tube at several locations around the circumference. The extracted material properties provided a good agreement between measured and predicted using FEA strain and thickness distributions after tube bending and hydroforming processes [21-23,41]. A major drawback of such material property determination was the low strain attained at the onset of necking in the uni-axial tensile test compared to the strain achieved in tube bending and hydroforming experiments. Therefore, when tensile test data was utilized in FE tube bending and hydroforming simulations it had to be extended beyond the point of UTS by assuming a terminal n-value for the material [21-23].

Fuchizawa *et al.* [42], Koc *et al.* [10], Ahmetoglu *et al.* [5], Sokolowski *et al.* [33], Strano *et al.* [18,34], Groche *et al.* [16,38] and Altan *et al.* [43] advocate use of the tube free expansion (bulge) test to evaluate tube material properties for hydroforming applications. In this test the ends of the tube were closed and the tube was pressurized to burst from the inside. Axial force could be applied if necessary to vary the stress state. Material property determination using the tube bulge test is more attractive for tube hydroforming applications because it reflects the stress state, encountered in the hydroforming process. The tube material in the die cavity is usually subjected to bi-axial or even tri-axial stress states and rarely to the uni-axial stress state [5,10,33,34,42-44]. Also, if the tube free expansion test is conducted with compressive axial load, the tube can potentially achieve higher strain levels at the onset of necking than in the uni-axial tensile test. Nevertheless, there is not much published data on tube material property determination using the tube bulge test with additional axial load, while most of the cases consider tube bulge tests with zero axial load and a nearly plane-strain loading path [42]. Strain levels achieved in such cases are comparable to those in the standard uni-axial tensile test, which is disappointing due to much higher complexity and cost of tube bulge testing [10,34].

In the biaxial case of tube bulging, the stress-strain curve cannot be directly obtained during the experiment. To extract stress-strain relationships from the tube bulge test, several methods were developed including a simple stress balance equation method [10,16,33,38,42,43], an analytical inverse energy method [34] and a method based on iterative adjustment of the stress-strain relationship through FEA simulations to fit experimental expansion and thickness data [10,33,43]. The first two analytical methods require radii of curvature of the bulge in the hoop and longitudinal directions, internal pressure, axial load and tube thickness to be obtained experimentally or assumed analytically. According to Koc *et al.* [10], in ideal circumstances all parameters should be measured “online” during the test, which was rarely the case due to the complexity and high cost of some of the measurements. Fuchizawa *et al.* [42] conducted a series of tube bulge tests on annealed aluminum, copper, brass and

titanium tubes and obtained the stress balance equation analytical method, based on the "online" measurements. The material properties of aluminum, copper and brass, analytically obtained using this method and those extracted from the uni-axial tensile test were almost identical. Only for titanium the stress-strain curve was experimentally obtained at higher strain levels using tube bulge test, compared to the uni-axial tensile test. It showed the benefits of tube bulge test for material property determination.

Koc *et al.* [10] and Sokolwski *et al.* [33] developed an "offline" variation of the same method, for which only the tube expansion and tube internal pressure were measured experimentally, while the other parameters were estimated analytically. Although, both studies presented good agreement between measured and predicted tube wall thickness data [10], the adopted assumptions were ambiguous, particularly if material anisotropy had to be considered. Another analytical technique suggested by Strano *et al.* [34] required similar assumptions and utilized iterative minimization of a deformation energy function.

To overcome the limitations of analytical methods, an inverse iterative technique using FE simulations and the Downhill Simplex optimization method [45] was considered to adjust a stress-strain curve with a FE simulation to match the experimental tube bulge expansion [10,33,43]. Such method utilized FEA for the curve fitting of the material property input, rather than measuring experimental stress-strain curve.

As a result, it can be concluded that for the low strain levels the uni-axial tensile test is an easy and reliable alternative to the tube bulge test for experimental material property determination. To obtain an experimental stress-strain curve for strains beyond the uni-axial UTS strain level, tube bulge tests should be conducted with additional compressive axial load and "online" measurements. Such testing is not always readily available.

1.2 Tube bending

The success of tube hydroforming process is largely determined by the preceding forming operations. Pre-bending operation is commonly needed to shape a tube to fit within a hydroforming die. The effect of pre-bending operation, which changes the strain and thickness in the tube, should be well understood in order to improve the amount of residual ductility for the subsequent tube hydroforming operation [23].

Tube bending can be achieved using three main techniques: compression bending, press bending and rotary-draw bending, as shown in Figure 5 [46]. In compression bending the tube is clamped to a bend die and a slide block is rotated around the static bend die. In press bending a ram die forces the tube against opposing wing dies. Press bending has a high production rate and is widely accepted in industry in massive production, while its major drawback is cross-sectional distortion of the tube.

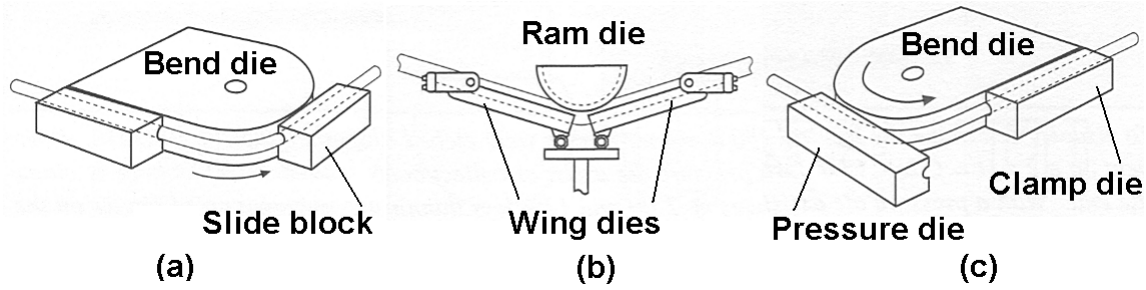

Figure 5: Schematics of (a) compression bending; (b) press bending; (c) rotary draw bending [46]

Rotary-draw tube bending provides consistent bends with repeatable thickness and strain distributions, which is particularly important for the success of subsequent hydroforming procedure [1,5,19-23]. Three main tools of the rotary-draw tube bender include the clamp die, bend die and pressure die, shown in Figure 6. The clamp die grips the tube end against the bend die. Both dies rotate together drawing the tube around the bend die. The pressure die reacts the bending moment created by the clamp and the bend die. The pressure die translates tangent to the bend die along the axis of the tube. For the bends with tight radius and small tube wall thickness two optional tools, the mandrel and the wiper die, are utilized to prevent cross-sectional collapse and wrinkling on the inside of the bend. The following sections describe important parameters controlling the rotary-draw tube bending process.

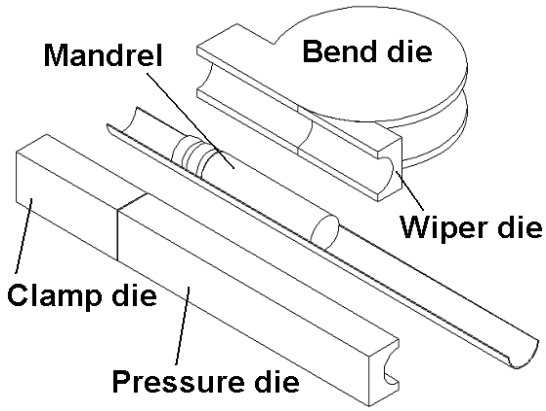

Figure 6: Rotary-draw tube bending dies [46]

1.2.1 Rotary-draw tube bending

R/D ratio

R/D ratio is a ratio between the centerline radius (R) of the bend and the outer diameter (D or OD) of the tube. A decrease of the R/D ratio together with an increase in the ratio between the tube OD and tube wall thickness is indicative of an increased bend severity [1,19,22,47]. Severe bends require optional tools like mandrel and wiper die and determine the complexity of these tools [47].

According to the numerical parametric study conducted by Yang *et al.* [30], smaller bend radii produced larger thinning of the tube on the outside of the bend and higher levels of the cross-sectional distortion. Therefore one of the ways to increase residual formability after the bending operation is to reduce bending strains through the increase of the R/D ratio. At the same time, R/D ratio is often constrained by the shape requirements of the final part and in real applications there is not that much room for the adjustment of this parameter.

Pressure die and bending boost

The pressure die not only reacts the bending moment from the clamp and bend dies, but also controls the amount of the material pushed into the bend. An axial force, known as the boost force, acts on the pressure die along the direction of the tube motion. It pushes more material into the bend region. This technique is called bending boost. Dwyer *et al.* [31] determined numerically that for a given R/D ratio, bending boost had the most significant effect on the post-bending thickness and strain distribution. Higher pressure die clamping load increased friction between the pressure die and the tube, allowing extra material to be pushed into the bend (Figure 7a). Pressure die slip limits the amount of boost load that can be applied to the tube using friction between the tube and the pressure die. Dwyer *et al.* [19] and Dyment *et al.* [20] suggested a boost block, attached to the end of the pressure die, or an independent follower, pushing directly on the tube end, as shown in Figure 7b,c. The boost block ensured zero pressure die slip, eliminating friction limit on the boost load. The new limit for the maximum boost load using this approach became wrinkling of the tube at the inside of the bend.

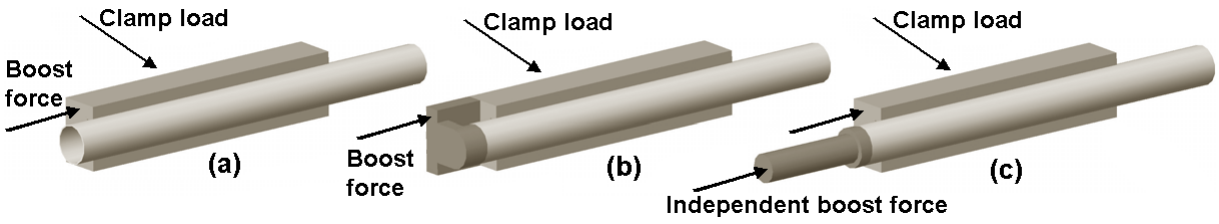

Figure 7: Boost configurations: (a) friction push; (b) boost block; (c) independent boost [20]

Bending boost is usually determined as a ratio between the velocity of the center-line of the tube and the tangential velocity of the bend die [20,21,22]. It also can be expressed as a ratio between the tube displacement and corresponding arc length of the center-line of the bend.

$$bending\ boost = \frac{tube\ displacement}{arclength\ of\ bend} \cdot 100\%$$

Inoue *et al.* [47], Dwyer *et al.* [19], Oliveira *et al.* [23] and Bardelcik *et al.* [21,22] showed that bending boost promoted a shift of the neutral axis of the bend towards the outside, reducing the axial strain and thinning on the outside of the bend. Dyment *et al.* [20,41] and Bardelcik *et al.* [21,22] investigated the effect of bending boost on thickness and strain distributions of pre-bent IF, AKDQ and DP600 steel tubes. Comparison of tubes bent with low (95%), medium (100%) and high (105%) boost levels confirmed that the increased boost had an overall positive effect, increasing thickness around the circumference of the tube and decreasing strains on the outside of the bend. The major engineering strain along the outside of the R/D=2.0 bend reduced about 8% with the increase from low to high boost level. Also, higher boost reduced bend head torque and mandrel drag load in tube bending.

Wiper die and wrinkling

Inoue *et al.* [47], Dwyer *et al.* [31], Dyment *et al.* [20,41], Yang [30] and Oliveira *et al.* [23] emphasized the importance of the wiper die for suppressing wrinkles on the inside of the bend, especially for small radii bends. The wiper reacts the load applied by the pressure die and helps to control the amount of the material pushed into the region at the inside of the bend. The friction between the wiper die and the tube retards material flow into the bend region reducing excessive thickening.

Inoue *et al.* [47] studied tube bending of stainless steel tubes with the R/D ratios of 1.5, 2.5 and 4.0. The first two bends required a wiper die on the inside of the bend, while at R/D=4.0, acceptable bends were obtained without a wiper die. Yang *et al.* [30] investigated an effect of clearance between the tube and the wiper die on elimination of wrinkling.

Mandrel and cross-sectional distortion

Rotary-draw tube bending of thick-walled tubes can be conducted without a mandrel or with a simple solid mandrel, while thinner-walled tube bending requires a ball mandrel [47]. Yang *et al.* [30] determined that the mandrel reduced cross-sectional distortion, producing an excellent circular cross-section of the bend and increased thinning as opposed to tubes bent without a mandrel or using press bending with a bend die only. According to Inoue *et al.* [47] a bent tube underwent the highest straining in the portion that passed over all mandrel balls. It lowered in the regions of the tube that did not fully

pass over the mandrel at the beginning or the end of the bend. Trana [25] showed using FEA that flexible mandrel helped to achieve failure-free pre-bending, pre-forming and hydroforming of an A-pillar, while use of a rigid cylindrical mandrel in the same process resulted in failure.

The effect of friction in tube bending

Gao *et al.* [32] determined through FEA simulations that a better lubricant with lower friction coefficient reduced thinning in the bending operation. Oliveira *et al.* [23] experimentally investigated this effect in steel and aluminum tube bending. The process variables, including bend die torque, pressure die feed load and mandrel load, appeared to be very sensitive to the type of lubricant used, significantly decreasing when better lubricant was applied. Conversely, the variation of the thickness distribution in tube bending was less sensitive to friction condition for both materials. Inoue *et al.* [47] observed the same trend, investigating experimentally the effect of lubricant in stainless steel tube bending.

1.2.2 Tube bending simulations

Dwyer *et al.* [19] studied the interaction between the tube bending tools and concluded that strain and thickness distributions in the bend couldn't be predicted well by bending theory. When predicting general trends [48], analytical approximations couldn't account for the particular tube bender setup, which had a significant effect. These approximations can be utilized for initial studies, while FEA should be conducted in order to optimize tube bending parameters and investigate their effect on the residual formability of a pre-bent tube.

A large amount of work on FEA of the tube bending process has been done by Gao *et al.* [32], Dwyer *et al.* [19], Dyment *et al.* [20,41], Oliveira *et al.* [23] and Bardelcik *et al.* [21,22]. Their studies concerned FEA of the effects of material properties, process parameters and die setup configuration in rotary-draw tube bending. Bardelcik *et al.* [21] investigated the effect of element formulation in tube bending simulation, considering plane-stress shell elements and solid elements to model the tube. Both shell and solid models accurately predicted the trends of reduced major strain on the outside of the bend and increased thickness at higher bending boost.

In order to accurately simulate the tube hydroforming process the results of pre-bending and pre-forming operations should be utilized as an input for the hydroforming process. Finite element analysis provides this opportunity through a simulation sequence, modeling the process from bending to pre-forming and hydroforming. Thickness, strain and residual stress histories and final geometry of the part at the end of each step in this sequence must be carried forward to the next step [5,7,19-23,31].

1.2.3 Tube pre-bending effect in hydroforming

Koc [7], Yang *et al.* [30], Trana [25], Dwyer *et al.* [31], Dyment *et al.* [20,41], Bardelcik *et al.* [21,22] and Oliveira *et al.* [23] showed that ability of the tube to be hydroformed was severely reduced by the pre-bending operation. According to Dwyer *et al.* [19], after the bending operation the tube formability was largely consumed and possibilities to optimize hydroforming operation in the remaining "formability window" were limited. Therefore the designer should use every opportunity to reduce strains and thinning in pre-bending operations. According to Dwyer *et al.* [19] and Dyment *et al.* [20], changes in strain paths from bending to hydroforming made the interaction between these processes more complex and a small change in bending strains could significantly increase formability in hydroforming.

1.3 Tube hydroforming

In the tube hydroforming process a tube must be shaped to conform to the internal surface of the die by the combined action of internal pressure and axial loading. The success of the hydroforming operation can be verified against two criteria, suggested by Dohmann *et al.* [1]: the quality of the contact between the final part and the die and the quality of tube wall thickness distribution in the final part. In other words, the hydroforming process should be designed to achieve maximum contact between the tube and the die, while maintaining thickness variation in certain limits.

Hydroforming tooling systems consist of die holders, dies, inserts, punches, sealing systems, optional counterpunches and movable inserts. Die inserts are utilized to broaden the number of products that can be created using the same die [2]. General guidelines [7] for hydroforming tooling include high strength against stresses due to large internal pressure and axial loading; good surface finish to minimize friction; flexibility through use of interchangeable inserts; good guiding systems; balanced design minimizing the closing force requirements.

Presses in tube hydroforming process are utilized to open and close the dies, provide clamping load during hydroforming and prevent die separation. Hydroforming presses up to 10 000 ton are currently in operation at plants around the world [7]. The maximum available press clamping load and part dimensions define the limit of the allowable internal pressure.

Water and hydroforming oil are conventional hydroforming pressure mediums, while low-melting-point alloys or liquid solutions can also be used [4]. Ahmetoglu *et al.* [2] employed a viscous polymeric material as a pressure medium in hydroforming experiments due to its benefits over fluid, including

increased sealing qualities and short deceleration distance, especially important in cases of unexpected bursting or leaking.

Axial punches in hydroforming provide sealing and apply additional axial load to the ends of the tube, referred to as an end-feed. Tube formability can be increased by feeding additional material into the die cavity in a controlled manner simultaneously with internal pressurization. The loading limits in the tube hydroforming process are imposed by three main failure modes of buckling, wrinkling and bursting, shown schematically in Figure 8 [9,1,26,49-52]. These modes can be postponed or avoided through the adjustment of tube material properties, friction, process control parameters and tool design.

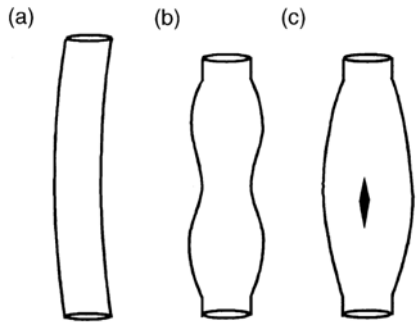

Figure 8: Common failure modes of (a) buckling; (b) wrinkling; (c) bursting [26]

Buckling is especially dangerous at the initial stages of hydroforming process, when high axial load might not be accompanied by a sufficient increase of section modulus of the tube [4,1]. The risk of buckling increases for longer tubes with thicker walls. To avoid buckling, simple estimations of permissible load for the corresponding free length of the tube can be made based on analytical assumptions [1,26].

Wrinkling is usually observed during both initial and intermediate stages of hydroforming and is not related to the length of the tube. Its likelihood increases with a decrease in tube wall thickness [4,26]. Wrinkles are sometimes unavoidable in the intake regions of the die, but can later be eliminated by the increased internal pressure. Nevertheless, some wrinkles cannot be ironed out or could require substantially higher internal pressure, which might not be attainable due to limited press clamping load capability [1].

Bursting occurs when a tube reaches a critical amount of expansion. It usually starts with necking when deformation and thinning localize, preventing further distribution of strain in the tube. This process is highly sensitive to friction between the tube and the die wall. High friction can lock up the material,

decreasing its flow into the deformation zone, triggering localization of deformation, necking and subsequent splitting of the material.

1.3.1 Straight tube hydroforming

A final part in straight tube hydroforming is usually obtained through expansion in an axially symmetric a concentric die or concentric die with counterdraft elements, as shown in Figure 9a-c [4,1]. Protrusions, connected to the tube through the part of tube surface, having similar cross-section (T-, Y-shapes), shown in Figure 9d, can also be formed from straight tubes [2,1,15,53]. Such parts with branches find wide application as exhaust connector components [53].

Straight tube hydroforming can utilize an opened die with a transverse joint face (Figure 9a) or a closed die with longitudinal joint face (Figure 9b) [4,9,1]. During hydroforming in the opened die, a tube is pushed on the ends and forced to expand, while two halves of the die are closing. The tube walls come in contact with the die only towards the end of the process as the die is closed fully. This avoids relative motion and friction between the tube and the die wall during the most of the process, although there exists a significant danger of buckling. During hydroforming in a closed die, the die is first closed and the tube is pressurized, while an axial load is provided by axially moving punches, pushing on the tube ends. In such case tube burst would be a predominant failure mode due to friction between the tube and the die. More advanced hydroforming processes can utilize die segment movement perpendicular to the tube longitudinal direction, producing bent or gooseneck geometries [1].

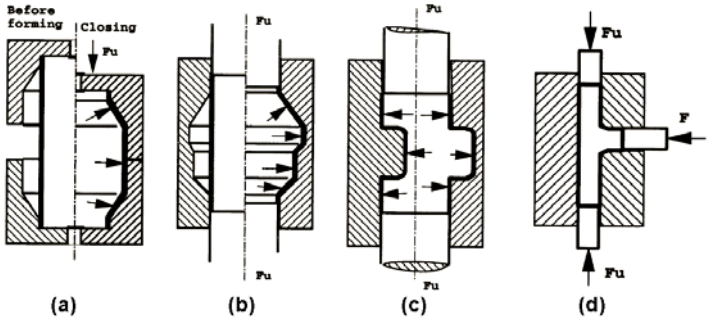

Figure 9: Primary cases of straight tube hydroforming [4]: (a) axially symmetric die with transverse joint face; (b) axially symmetric die with longitudinal joint face; (c) concentric die with counterdraft elements; (d) hydroforming of tube branch elements

Another variation of tube hydroforming is often referred to as low-pressure tube hydroforming. In this case the tube is pressurized to relatively low pressure, while the die is closing, introducing compressive stresses perpendicular to tube walls [9]. Such a process enables sharp corner radii to be formed with small thickness reduction. The perimeter of the cross-section of the die in this case is usually the same

as the initial perimeter of the tube. The concept behind such a forming process is changing of shape of the tube cross-section rather than tube expansion.

A wide range of work has been done on different aspects of straight tube hydroforming. Li *et al.* [44] analytically investigated the stress states encountered by the tube during hydroforming within different zones inside the hydroforming die. Ahmetoglu *et al.* [2] experimentally investigated low carbon steel and aluminum 6061-T6 undergoing axisymmetric bulge hydroforming and obtained good agreement between predicted and experimental thickness distributions. Manabe *et al.* [28] numerically investigated the effects of material properties, process parameters and friction coefficient on tube hydroforming in a straight die with square cross-section.

Koc *et al.* [15] and Ahmetoglu *et al.* [2] conducted experimental and FEA studies of T-shape protrusion hydroforming and concluded that FEA simulations could well predict the bulge height. Koc *et al.* [15] determined that the limiting protrusion height increased with the decrease of the distance between the expanding region and the feeding end of the tube. Jirathearanat *et al.* [53] optimized process parameters in Y-shape tube hydroforming, using iterative FE simulations. A shorter tube length had a beneficial effect on the achievable Y-shape protrusion height due to decreased contact area and lower net friction force, which led to increased material flow into the expanding zone.

Hwang *et al.* [3] numerically investigated straight tube hydroforming in a rectangular die and compared tube expansion in the die (Figure 10a) with one incorporating tube pre-forming and then crushing by the closing die (Figure 10b). Although the pre-forming and crushing process utilized extra dies, the maximum internal pressure required to fully form the tube in this case was 20 times smaller than in case of the tube expansion process. The thickness variation in the crushing case was also more uniform than in the expansion case.

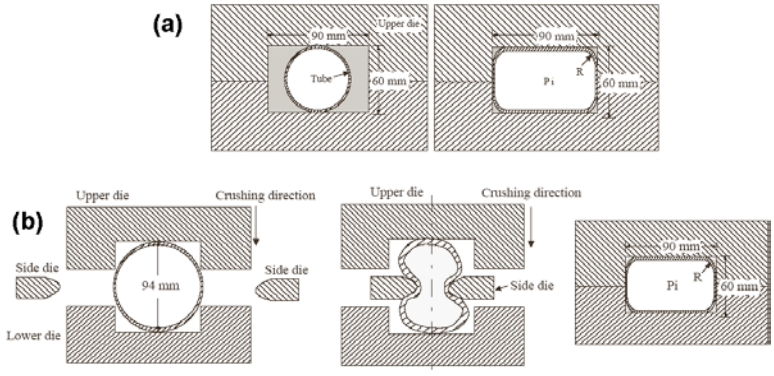

Figure 10: Hydroforming in rectangular die sequences: (a) expansion process; (b) pre-forming/crushing process [3]

1.3.2 Pre-bent tube hydroforming

For many applications a tube is pre-bent at multiple locations and then crushed prior to the hydroforming process, as shown in Figure 11. For example, for a rear axle support automotive component a tube is pre-bent in three planes to satisfy the spatial constraints of the final part [9]. The pre-forming operation changes the thickness and strain distributions in the tube, which must be taken into account to ensure sufficient residual formability for a successful hydroforming operation [9,13,19-22].

Figure 11: Typical pre-bent, crushed and hydroformed part [1]

Sometimes when only a section of the hydroformed part is assumed to carry most of the load, a tube can be tailor-welded from multiple tubes with different wall thickness and the same outer diameter prior to bending and hydroforming. This technique offers potential weight savings.

A large amount of work has been performed by Koc [1,7], Yang *et al.* [30], Trana [25], Gao *et al.* [32], Dwyer *et al.* [31], Dyment *et al.* [20,41] and Bardelcik *et al.* [21,22] to investigate various aspects of pre-bent tube hydroforming. Gao *et al.* [32] numerically investigated 90-degree pre-bent stainless steel tube hydroforming and suggested die design improvements to reduce thinning of the final part. Bardelcik *et al.* [22] numerically investigated the effect of increased end-feed on hydroforming of pre-bent DP600 steel tubes. Negative corner-fill expansion was detected in pre-bent tube hydroforming, when, during pressurization, the tube moved away from the inside radius of the die as deformation initiated at the outside of the bend. Feeding of 20 mm of the tube end into the die cavity produced a 30% increase in corner-fill expansion compared to the zero end-feed case. Overall, the effect of end-feed on tube burst pressure and corner-fill expansion in pre-bent tube hydroforming was more pronounced and beneficial than the effect of bending boost.

1.3.3 Effect of material properties in tube hydroforming

Carleer *et al.* [29], Manabe *et al.* [28], Chu *et al.* [50-52], Kim *et al.* [49] and Xia [6] investigated the effect of material properties (n-value, strength coefficient, amount of pre-strain and material anisotropy (r-value)) on formability in tube hydroforming. Based on these studies, material anisotropy (r-value) and strain hardening exponent (n-value) were determined to have the most significant effect on tube formability.

Carleer *et al.* [29] conducted analytical, FEA and experimental studies to determine the effect of material r-value and n-value on hydroformability of the tube in a free expansion test. Experimental results for steels ranging from low to high strength showed that high n-value and r-value together with low yield strength produced the highest major and minor "safe" strains. FEA simulations and analytical studies confirmed that higher r- and n-values resulted in more uniform strain distributions due to higher material flow (Figure 12a). Higher r-value reduced the slope of the strain path in the strain space resulting in tube burst occurring at higher compressive strain (Figure 12b). Other parameters, like pre-strain and strength coefficient, had negligible effects on strain distribution.

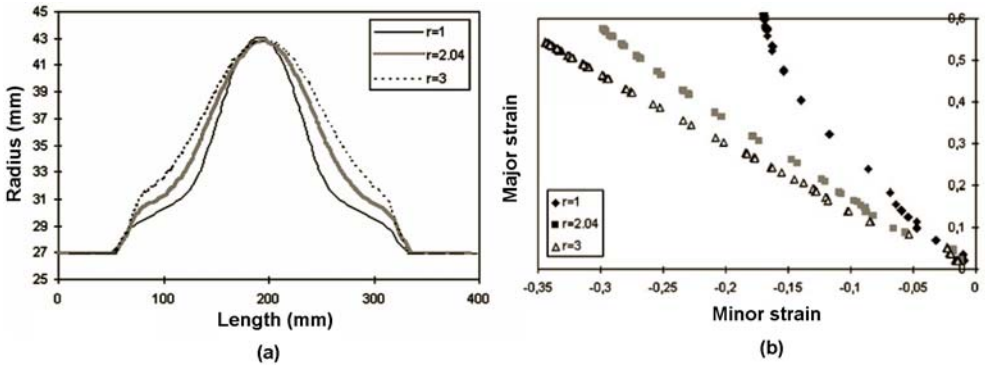

Figure 12: Effect of r-value on (a) tube profile; (b) strain distribution [29]

Kridli *et al.* [24] experimentally and numerically investigated the effect of material n-value in straight tube hydroforming and determined that material with higher n-values could be formed to smaller die corner radii than material with a lower n-value.

Koc [1,11] numerically investigated the effect of material n-value on tube expansion in the free expansion test. An increase of n-value from 0.16 to 0.22 produced only a 7% increase of expansion ratio. Koc [1,11] experimentally confirmed the robustness of a structural frame rail tube hydroforming process to variation in material properties due to different heat treatment of the tubes after the rolling operation.

Xia [6] analytically studied the effect of r-value on the bursting and wrinkling limits in free expansion hydroforming of straight DDQ steel tube, shown in Figure 13. Tubes with lower r-values appeared to exhibit lower bursting pressures and to wrinkle more easily due to higher deformation in through-thickness direction of the tube.

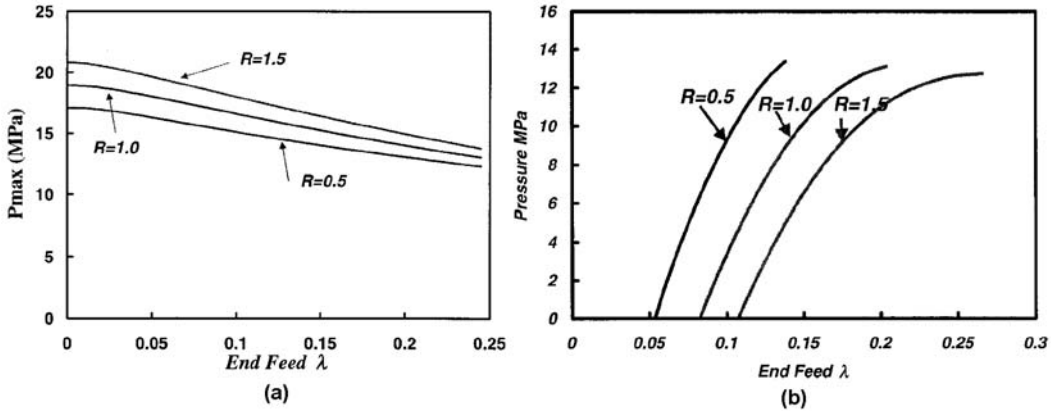

Figure 13: Effect of r-value on (a) tube bursting limit; (b) tube wrinkling limit [6]

Chu *et al.* [50,51,52] and Kim *et al.* [49] analytically investigated the effect of r-value and n-value on the wrinkling, buckling and bursting limits in tube free expansion hydroforming. Higher r- and n-values expanded the "window" of failure-free paths in internal pressure versus axial load plane (Figure 14), confirming the trends obtained by Carleer *et al.* [29] and Xia [6]. Increased strain-hardening exponent (Figure 14b) had a more significant effect on postponing all failure modes than increased r-value [49,52].

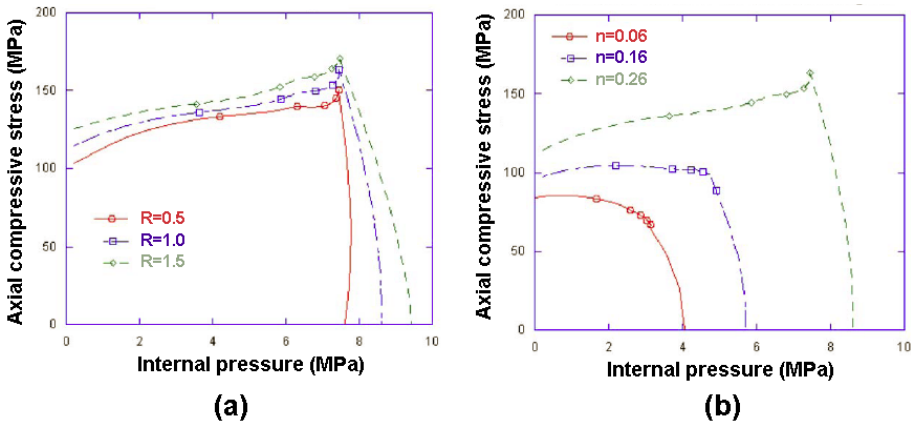

Figure 14: (a) effect of r-value on the process window diagram; (b) effect of n-value on the process window diagram [52]

1.3.4 Effect of friction in tube hydroforming

Substantial changes of the cross-section of the tube occur in the tube hydroforming process at high internal pressure. High pressure produces high interfacial pressure between the tube and the die wall and high retarding friction forces, preventing uniform strain distribution and resulting in localized thinning, necking and splitting of the material. Manabe *et al.* [28] used FEA of straight tube hydroforming to show that an increase of thinning occurred with an increase in friction coefficient. Friction after the r-value of tube material had the largest effect on formability in tube hydroforming according to Carleer *et al.* [29].

The problem of tube/die contact interaction is difficult because different regions of the tube inside the die experience different types of contact in terms of surface pressure, stress state and sliding velocity. Koc *et al.* [1,7,8], Ahmetoglu *et al.* [5] and Strano *et al.* [18] isolated three main friction regimes in three corresponding zones inside the hydroforming die, shown in Figure 15. In the guided zone, the tube experienced a large amount of rapid motion relative to the die, while the expansion of the tube was constrained. In the transition zone, material movement was slower and the tube material was under a three-dimensional stress state. In the expansion zone, the axial movement was negligible and slow circumferential stretching of the material was dominant.

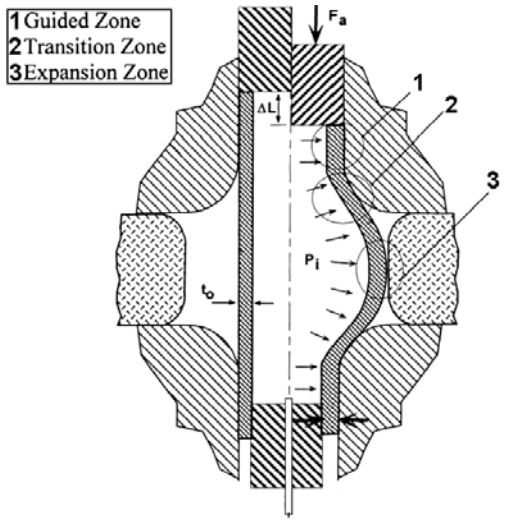

Figure 15: Friction zones [7]

Lubricant selection enables a decrease in sliding friction, local sticking or galling and reduces tool wear, axial forces and thinning [1,5,7,8,18,28,29]. According to Koc *et al.* [1,7,8] and Ahmetoglu *et al.* [5], hydroforming lubricant should be selected based on the following criteria: lubricity to reduce sliding friction between tooling and tube surface; durability under high pressure; minimum abrasivity to

reduce tool wear; compatibility with the pressure medium and environmental requirements; and ease of application and removal. Several types of lubricants exist, depending on their composition, including solid film lubricants (dry), wet lubricants (solutions, emulsions and synthetics) and pastes, soaps and waxes [5,7,8]. All of these types have their respective advantages in terms of performance, application, compatibility, removal and cost. Koc [1,8] experimentally studied the performance of dry, wet and paste lubricants on formability of a structural automotive frame rail involving pre-bending and hydroforming. Dry lubricant produced the least amount of thinning and thickness variation as well as highest axial feeding capability, requiring the least amount of axial force.

1.3.5 Load schedule design effect in tube hydroforming

The success of failure-free hydroforming depends on proper coordination between simultaneously applied internal pressure and axial load [1,2,4,11,16,17,26,28,32,53]. Ahmetoglu *et al.* [2] determined that controlled adjustment of axial load versus internal pressure schedule improved tube formability. Manabe *et al.* [28] investigated the optimal ratio between axial stress and internal pressure that produced more uniform thickness distribution in straight tube hydroforming. Gao *et al.* [17] suggested a classification of tube hydroforming processes based on their sensitivity to internal pressure or axial load. Several tools based on analytical models, FEA simulations and experiments were developed to determine the process window for failure free hydroforming [1,6, 9,11,1,14,17,18,26,28,53].

Koc *et al.* [1,11,26], Jirathearanat *et al.* [53] and Rimkus *et al.* [14] utilized simple analytical methods to obtain initial values of yielding, maximum pressure and axial feeding for the loading path design. Koc *et al.* [26] developed an analytical "first-step-tool" using plasticity and membrane theories and thin- and thick-wall tube assumptions to determine internal pressure, buckling- and wrinkling-free axial forces and counter force limits. Using these models Koc [1,11] developed a loading schedule for simple T-shape hydroforming, which was later evaluated using FEA, to assess the effect of loading path on the protrusion height and thickness variation. Feeding more material at the earlier stages of hydroforming, when internal pressure was low, produced less thinning in the expanding zone and increased bulge height. Jirathearanat *et al.* [53] analytically estimated the initial set of process parameters for Y-shape tube hydroforming, optimized it using FEA, and confirmed that higher material feeding at the initial stages of hydroforming was beneficial.

Dohmann *et al.* [1] calculated process parameters for straight tube hydroforming of an axially symmetric shape based on membrane theory. The results were presented as an axial load versus internal pressure failure diagram, shown in Figure 16a, enabling selection of failure-free combinations of the loading parameters. Xia [6] and Kim *et al.* [49] similarly obtained analytical equations, determining the

onset of bursting and wrinkling in tube free expansion hydroforming. Xia [6] presented failure diagrams for DDQ, DQAK and 6061-T4 aluminum (Figure 16b). Chu *et al.* [50,51,52] developed advanced mathematical models for the concept of a "process window diagram", determining the limits of wrinkling, buckling and bursting for the general case of tube hydroforming.

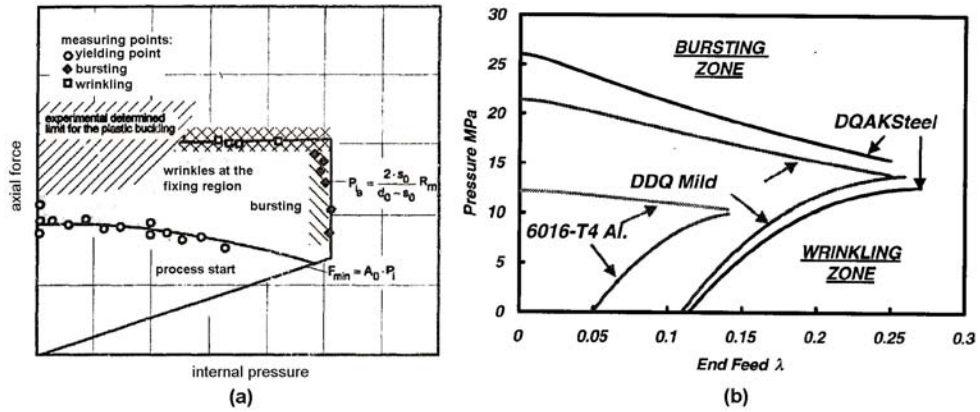

Figure 16: (a) failure diagram for hydroforming of axisymmetric shapes with straight axis [9]; (b) failure diagram for DDQ, DQAK and aluminum 6061-T4 [6]

A number of studies have been conducted to evaluate the optimal internal pressure versus axial load path for a given part type, shape, material and lubrication using FEA simulations [1,11,17,18].

One of the techniques, referred to as "self-feeding" [18], provided good results for most structural and frame parts, having limitations for non-axisymmetric applications. In the first step of the technique, hydroforming simulation was carried out with zero friction and zero applied axial load to determine the displacement of tube ends due to self-contraction. In the next step, iterative simulations with real friction conditions were performed, while tube end displacement attained in the first step was scaled and applied to decrease thinning of the part.

Another approach, adaptive simulation [1,11,17,18], was implemented through incremental hydroforming simulations. A software module scanned the part for failure spots at each time step and predicted the load path for the next time step based on the defect trend. Such an algorithm optimized the loading schedule within a single simulation, producing a part without wrinkles and excessive thinning [17].

While buckling and wrinkling in tube hydroforming can be predicted by FEA simulations and iterative techniques have been developed to adjust process parameters to avoid them, prediction of the onset of necking in tube hydroforming process remains a challenge. A number of methods have been developed

in order to predict the onset of necking in sheet and tube metal forming using Forming Limit Diagram (FLD) [52,54-62], as described in the following section.

1.4 Forming Limit Curves

The forming limit of sheet or tube material determines the state when localization of deformation and thinning of the material initiates during the forming operation.

Keeler developed the first strain-based Forming Limit Curve (FLC) and expressed it in terms of critical major and minor in-plane components of engineering strain. If critical levels of strain were attained in the forming process, necking and subsequent splitting of the material occurred [55,56]. Although this method could be easily utilized directly on the press-shop floor for die and process optimization, it suffered from a number of issues. When applied to secondary forming operations involving pre-strain and non-linear loading paths, it failed to predict failure [60,61]. This often resulted in premature failure of the part far below the FLC. In other cases, strains far above the FLC were attained without necking.

The stress-based FLC method, proposed by Stoughton [57], offered a common forming limit curve in stress space, which was independent of the amount of pre-strain and appeared to be a universal characteristic of the material behavior. It was expressed in terms of principal major and minor in-plane components of stress. This criterion helped to overcome the limitations of the conventional strain-based FLC and could be used in the analysis of non-proportional paths and multi-stage forming processes.

Unfortunately, none of the above methods can be utilized for the failure prediction in straight and pre-bent tube hydroforming because both strain- and stress-based FLCs were derived according to through-thickness plane stress assumptions. When a tube is expanded within a hydroforming die, the through-thickness component of cannot be neglected, making the stress state three-dimensional and invalidating application of strain- and stress-based FLCs. Simha *et al.* [58,59,62] suggested the extended stress-based FLC (XSFLC), which was applicable to the prediction of necking under three-dimensional stress states.

1.4.1 Strain-Based forming Limit Curve

The first work on the strain-based FLC was started by Keeler in 1957 [56]. The goal was to investigate the existence of measurable limits that defined practical forming limits of sheet material. A single FLC, portraying the maximum strain that the material could undergo before the onset of necking, was found to exist. This new systematic method helped to predict the utility of new materials or suggest improvements for die design without press-shop trials.

While Keeler worked on the tension-tension portion of FLC (right side), Goodwin in 1968 presented the results for the tension-compression portion (left side) of the FLC. The combined Keeler-Goodwin data provided the first published strain-based FLC [56], shown in Figure 17.

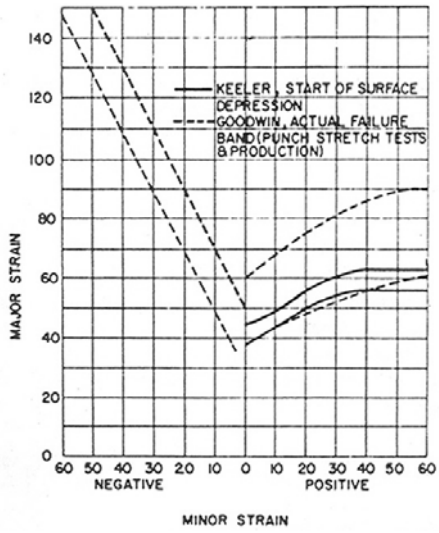

Figure 17: Combined Keeler-Goodwin FLCs [56]

A major improvement to the FLC method was introduced by Hecker, who developed the way of obtaining the strain-based FLC from large negative to large positive strains (Figure 18a), using strips of different width (Figure 19), stretched over a hemispherical punch (Figure 18b) [56].

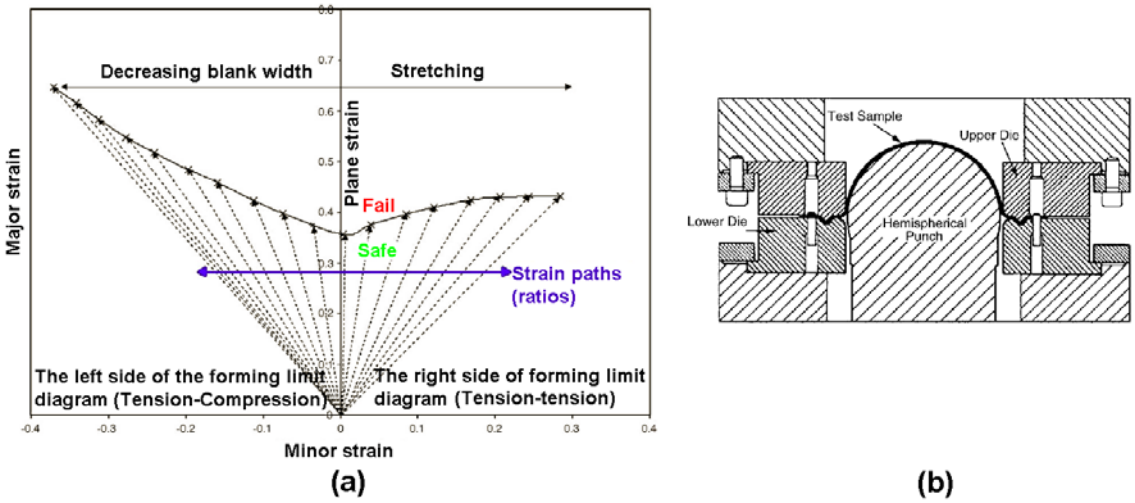

Figure 18: (a) schematic of forming limit diagram; (b) FLC test setup [63]

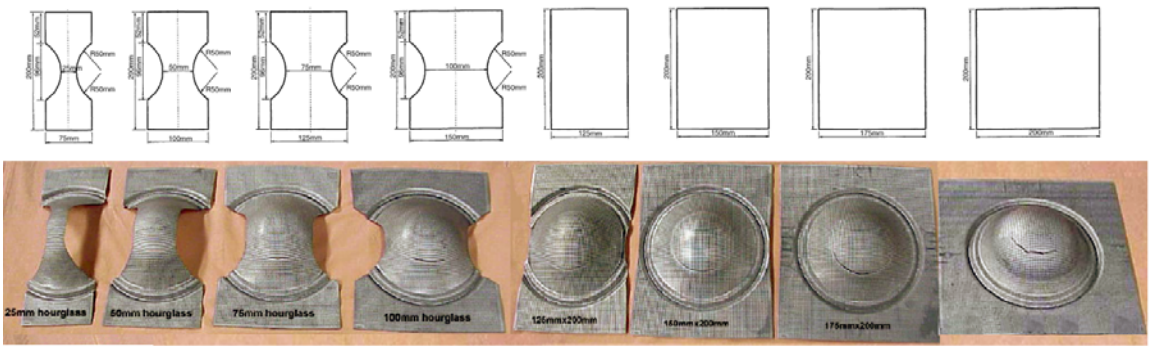

Figure 19: Test sample geometries and deformed test specimens [63]

Keeler and Brazier [55] continued the investigation of the strain-based FLC and experimentally determined that for several low-carbon steel sheets there existed a standard shaped FLC that had to be shifted to a certain level along the plane strain axis. The level of the plane strain intercept was determined by the thickness of the material and its n-value. The right side of the standard-shaped curve was the same as the original Keeler curve. The left side of FLC could be described by a line with a slope of unity in true principal strain space and intersecting the plane strain axis at the same value as the right side of the curve. These curves, verified by the laboratory hemispherical dome tests accurately predicted the onset of necking in production stampings [55]. For most steel sheets once terminal n-value was known from the tensile test, the plane strain intercept could be determined and the FLC could be obtained by shifting the standard-shaped FLC.

The limitations of strain-based FLCs included the assumptions of linear proportional loading and path dependence. Path dependence revealed itself in secondary forming operations, when forming limits could be significantly raised or lowered depending on the nature of the pre-strain path [60,61]. Graf and Hosford [60] investigated the effect of strain path change on FLC of Al 2008-T4. Bi-axial tension appeared to lower the entire FLC, decreasing, formability, while uni-axial tension raised the right side of the FLC without appreciable effect on the left side. Pre-straining in plane strain increased forming limits on both sides of FLC. Ghosh and Laukonis [61] investigated the effect of bi-axial pre-strain on the FLC of steel sheet. They observed that strain-based FLCs of the pre-strained material were not only shifted down, but also changed their shape at higher levels of pre-strain compared to the FLC of as-received material.

1.4.2 Stress-Based Forming Limit Curve

Stoughton [57] presented a detailed derivation of the equations for the transformation of a strain-based FLC into the true principal stress space for several constitutive models. According to Stoughton [57],

path dependence of the strain-based FLC was only a consequence of the nature of strain space where it was initially obtained.

Adoption of a path independent stress-based FLC simplified the assessment of forming severity. At the same time, unlike strain, the stress state couldn't be directly measured during the experiment, providing a challenge for its utilization in the press-shop. In FEA forming simulations, such problem disappears since stress state is determined together with the strain state.

Stoughton [57] used the results obtained by Ghosh and Laukonis [61] and Graf and Hosford [60] on path dependence of strain-based FLCs to show that regardless of the pre-strain, all forming limit curves mapped onto the same curve in the stress space, corresponding to the as-received material. Moreover, if the stress-based FLC of as-received material was mapped back into the strain space with different amounts of pre-strain, it agreed reasonably well with the experimental strain-based FLCs [60,61].

1.4.3 Extended Stress-Based Forming Limit Curve

Based on experimental results, Simha *et al.* [58] showed that in supported tube hydroforming, the tube necked in the regions that were in contact with the die. The third or through-thickness component of stress in those regions could not be neglected.

Neither strain- nor stress-based FLCs take into account triaxiality of stress state, since they were developed for plane stress cases. Proposed by Simha *et al.* [58], the XSFLC method could be applied to failure prediction under three-dimensional loading conditions. The XSFLC was obtained from the strain-based FLC, which was transformed into principal stress space and then, with additional assumptions, was transformed into invariant stress space, expressed in terms of mean stress and effective stress.

The key assumption in the XSFLC method was that the same invariants of the stress tensor that exist at the onset of necking under plane stress loading, result in necking initiation under three dimensional stress states. Simha *et al.* [62] verified that assumption, using FEA, obtaining XSFLC from the simulation under plane stress loading and then testing it for the same material under three-dimensional loading conditions. Stress tensor invariants at the onset of necking under tri-axial loading appeared to be well predicted by the XSFLC obtained from the plane stress computations. Additional assumptions [58] were developed for multi-stage forming cases when the material was loaded along different axes or compression-tension change of loading occurred.

The XSFLC failure criterion accurately predicted necking location in various cases of aluminum and steel tube hydroforming [58]. Predictions of the internal pressure at necking using the XSFLC were within 10% of the experimental results.

Application of the XSFLC method started with the strain-based FLC. Consequently, any ambiguity associated with strain-based FLC was transmitted to the XSFLC. While strain-based FLC for sheet material is well understood, the tube FLC is not. The uncertainties associated with the input strain-based FLC introduced additional challenge in the investigation of necking prediction in tube hydroforming using the XSFLC.

1.4.4 Strain-based FLC for tube material

A survey of available limited number of published data on tube FLC by Groche *et al.* [16,38], Green *et al.* [64], Chu *et al.* [52] and Chen *et al.* [54] revealed no consensus as to how strain-based FLC should be obtained and applied to the prediction of the onset of necking in tube hydroforming. The approaches range from the application of sheet FLC and the Keeler-Brazier approximation in tube hydroforming [54,64], to the determination of a special tube FLC, different from the sheet FLC, using the tube free expansion test [16,38,52]. The tube free expansion test with various ratios between the axial load and internal pressure provided different strain paths in strain space (Figure 20) and could be used both for validation of FLCs for tube applications and for establishing original tube FLCs. To obtain plane strain conditions in the middle cross-section of the tube, a tube with fixed ends and zero axial load should be pressurized, while for the left and right sides of the FLC compressive and tensile axial loads should be applied to the tube ends, respectively (Figure 21).

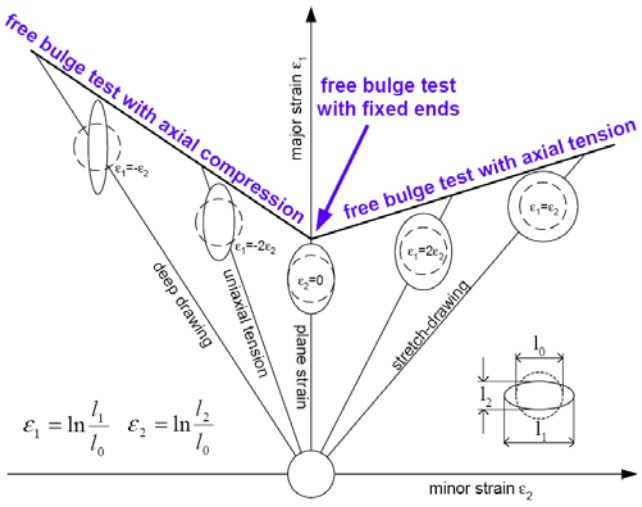

Figure 20: Forming limit diagram with characteristic regions [16]

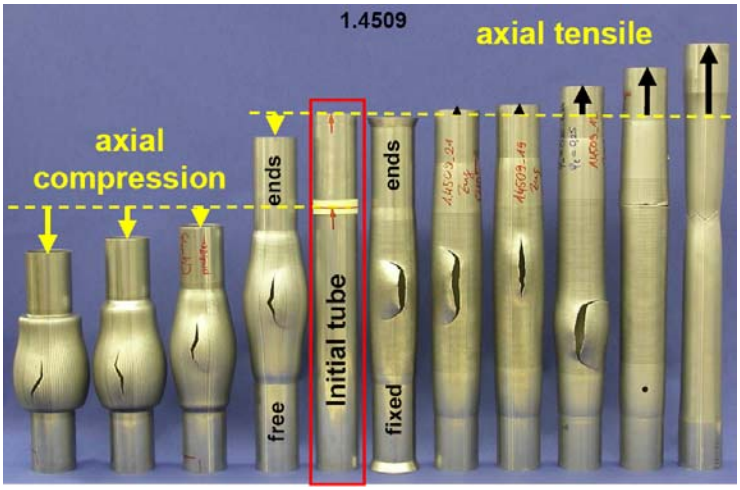

Figure 21: Tube specimens tested to obtain tube FLC [39]

It should be noted that no agreement exists in the interpretation of the results of the tube free expansion test for the purpose of tube FLC determination. The reason for the differences mainly comes from local versus global approaches to the strain at the onset of necking that should be utilized to generate tube FLC.

The sheet FLC concept implied that the strain in the region adjacent to the neck at the onset of necking be utilized as the necking strain of the material for a given loading path. Sometimes such approach is misrepresented by measuring strain next to the neck during necking and not at the onset of necking. If such approach was utilized for tube hydroforming, the obtained FLC would have limited or no application to failure prediction using FE simulations. This can be illustrated by the results presented by Groche *et al.* [16,37] and Green *et al.* [64]. Groche *et al.* [16,37] utilized the strain next to the failure location to determine the FLC of 1.4301 stainless steel tube using the tube free expansion test. The tube FLC and corresponding experimental internal pressure versus tube expansion curves are shown in Figure 22. The tube FLC had a plane strain intercept of 35%, resulting in a radial expansion of 12.6 mm at the onset of necking for the tube with 60 mm OD. From the pressure versus expansion curves of the 60mm OD and 1mm wall thickness tube, it was evident that maximum radial expansion at tube burst was between 10 mm and 12 mm (Figure 22b). Therefore, the local strain approach produced higher predictions for the tube expansion at the onset of necking. The sheet FLC for the same material, shown in Figure 22a, was higher than tube FLC and would produce even higher over-prediction of the tube expansion if utilized for the prediction of the onset of necking in the tube free expansion test (Figure 22a).

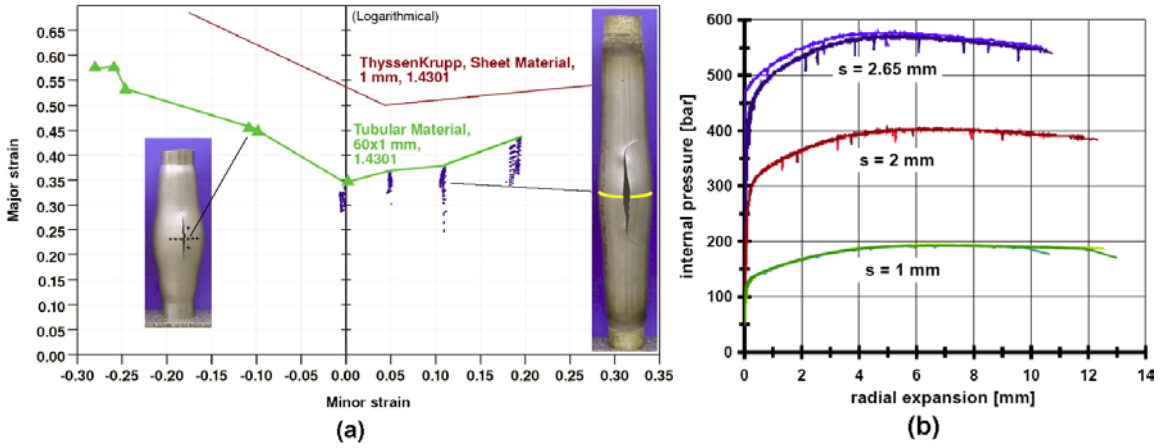

Figure 22: (a) 1.4301 stainless steel sheet versus tube FLCs (local formability approach for tubes); (b) experimental pressure versus expansion curves for 1.4301 stainless steel tubes with fixed ends [37]

Green *et al.* [64] also utilized local strain at the neck during necking or at burst to generate the tube FLC, providing further illustration of the disadvantages of the local strain approach. Obtained by Green *et al.* [64], the tube FLC agreed well with the Keeler-Brazier approximation that utilized the tube thickness and tube terminal n-value (Figure 23a). At the same time, corresponding strain distributions around the circumference of the tube showed that the high levels of strain utilized to generate the FLC were measured at the neck in the region next to the weld seam (Figure 23b). The average strain around the circumference of the tube in the same cross-section away from the weld and the neck was much lower. The obtained FLC was not of a practical interest for FE simulations, because predicted expansion and internal pressure at the onset of necking would always significantly over-predict experimental results. Without additional assumptions, the tube free expansion simulation would not indicate any strain localization and necking would be predicted by FEA only when strain everywhere around the circumference of the tube reached the high value of strain measured at the neck in the experiment. A more reasonable approach in this case would be to utilize the strain away from the weld and from the neck to establish the tube FLC. The corresponding FLC would be significantly lower than the one presented in Figure 23a, following the trend presented by Groche *et al.* [16,37].

Chen *et al.* [54] conducted FEA of an AKDQ steel tube free expansion test with the strain-based FLC obtained using Keeler-Brazier approximation, which resulted in 50% over-prediction of the experimental radial expansion at the onset of necking (20.3 mm predicted over 12.9 mm measured). This result confirmed that tube FLC should be lower than the one established using the Keeler-Brazier approximation or corresponding sheet FLC.

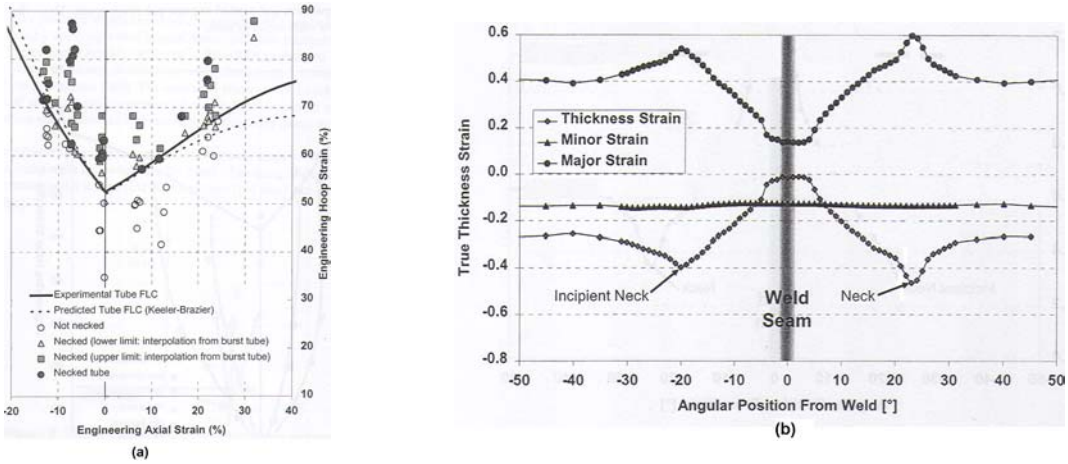

Figure 23: (a) AKDQ tube FLC; (b) AKDQ tube strain distribution [64]

Groche *et al.* [38] showed that the FLC based on the local strains next to the failure location would not reflect tube expansion at the onset of necking, making such an FLC inapplicable for the prediction of necking in tube hydroforming FE simulations. The tube FLC for 1.4509 stainless steel [38] was generated based on the mean major and minor strains around the circumference of the tube [38] (Figure 24). Such an FLC provided information about global and not local formability of the tube and portrayed the levels of average strain that had correlation with the expansion of the tube at the onset of necking. The global FLC had a plane strain intercept twice lower than the plane strain intercept of corresponding sheet material.

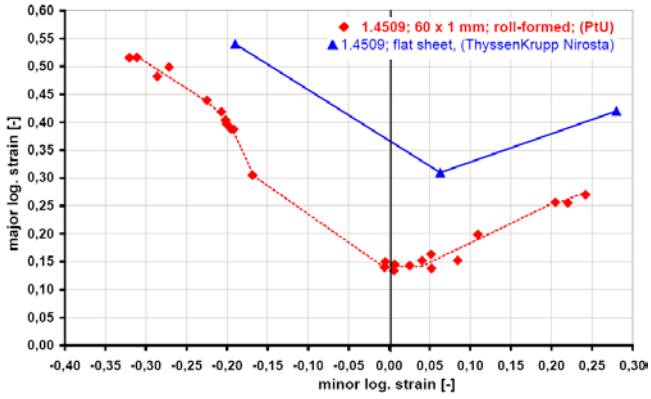

Figure 24: 1.4509 stainless steel sheet versus tube FLCs (global formability approach for tubes)

Chu *et al.* [52] showed both analytically and experimentally that for an aluminum tube the FLC should be one half of the sheet value (Figure 25a). A series of tube free expansion tests on extruded 6061-T4 aluminum tubes with axial load confirmed this analytical result (Figure 25b).

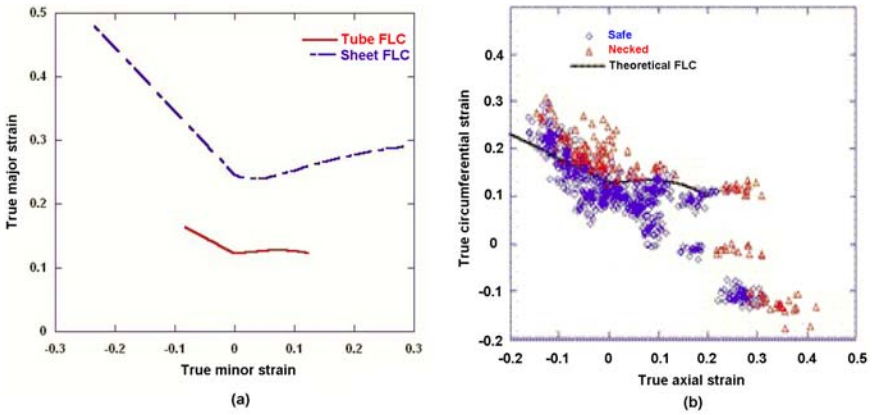

Figure 25: (a) analytically obtained aluminum sheet and tube FLCs; (b) experimental results for tube FLC [52]

As a result of the foregoing, some general guidelines for the tube FLC determination can be summarized: the sheet FLC leads to significant over-predictions of expansion if utilized in tube hydroforming applications; over-prediction of tube expansion at the onset of necking might also be a result of use of a local strain approach in tube FLC generation, if the strain at the neck was utilized.

The last comment on tube FLC should be made regarding the determination of the moment of necking initiation in tube free expansion tests. The internal pressure vs. radial expansion curve, presented in Figure 22b, had a peak after which expansion continued to grow, while internal pressure decreased. Analytical solutions based on simple assumptions and FEA simulations [6,49,54,65-67] confirmed the existence of the peak and subsequent decrease of internal pressure required to continue the expansion. The relationship between the internal pressure and radial expansion was shown to be nonlinear according to the analytical solution [65]. The non-linearity was the source of the peak on the curve. At the same time, Chu *et al.* [52], Xia [6] and Marciniak *et al.* [65] utilized this peak as an indicator of instability and necking initiation [6,65], regarded as maximum pressure criterion. Such assumption would be desirable due to its apparent simplicity, while its nature was wrong. Chen *et al.* [54] experimentally showed that in free expansion testing, tubes did not neck at the maximum pressure. This occurred between the point of maximum pressure and the point of burst on the internal pressure versus radial expansion curve.

1.5 Current research

The major goals of the current research include the investigation of the effect of pre-bending operation on tube formability, the effect of increased end-feed load in straight and pre-bent tube hydroforming, and the assessment of the XSFLC method for the prediction of failure in tube hydroforming. For this purpose, tubes with the same outer diameter and wall thickness fabricated from mild steel (DDQ), high

strength steel (HSLA350) and advanced high strength steel (DP600) are hydroformed in straight and pre-bent tube hydroforming dies with several levels of end-feed. Both straight and pre-bent tube hydroforming are simulated using the dynamic explicit finite element code LS-DYNA. Finite element simulations of straight and pre-bent tube hydroforming, validated using the experimental results, are utilized to investigate the aspects of failure prediction using the newly developed XSFLC method.

The balance of this thesis is organized as follows. Chapters 2 and 3 discuss the details of the experimental procedures and FE models, respectively. Chapter 4 describes the estimation of the tube XSFLC for the failure prediction using the numerical models. Chapters 5 and 6 present the experimental and numerical results. Discussion of the results is provided in Chapter 7. Chapter 8 contains conclusions and recommendations for future work.

Chapter 2

Experimental procedure

This chapter describes the tube bending and hydroforming experiments on the straight and pre-bent tube. The fundamental characterization experiments to determine the tube material properties and friction coefficients are also described.

Three different steel grades were examined in this research: a draw-quality mild steel (DDQ), a high-strength low-alloy steel (HSLA350) and a dual-phase advanced high strength steel (DP600). The DP600 and HSLA350 steels were cold-rolled and galvannealed, while the DDQ steel was hot-rolled without any galvanizing treatment. All tubes were seam-welded and had a 76.2 mm (3 inch) outer diameter. The nominal tube wall thickness was 1.88 mm. The actual tube wall thickness was manually measured around the circumference of two tubes per alloy in several cross-sections of the tube using a digital micrometer. The maximum tube wall thickness deviation from 1.880 mm was determined to be 0.015 mm for the DDQ, 0.030 mm for the HSLA350 and 0.022 mm for the DP600 tubes.

2.1 Material characterization

The engineering stress versus engineering strain data for the DDQ, HSLA350 and DP600 sheet and tube materials was extracted from the quasi-static tensile tests performed by van Riemsdijk *et al.* [36]. Tube and sheet specimens for those tests were cut from the same coils as those used to roll form the tubes for the bending and hydroforming experiments. The sheet material tensile specimens were machined along three orientations with respect to the sheet rolling direction: 0^0, 45^0 and 90^0. The

tube tensile specimens were cut from three locations around the circumference of the tube: 3, 6 and 9 o'clock with respect to the weld seam, as shown in Figure 26. Three tensile tests were conducted for each sheet orientation and each location around the tube circumference. The results from three tests were averaged for each case and are shown in Figure 27. The scatter between the results obtained from three tests for each case was less than 1% for the three alloys.

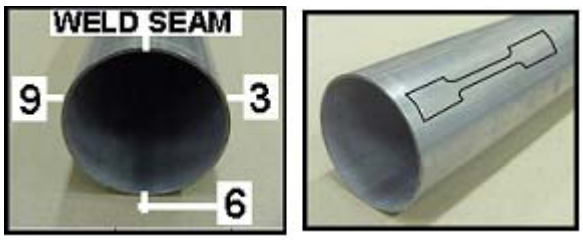

Figure 26: Tube specimens for quasi-static tensile test

Among the three alloys, the HSLA350 sheet material demonstrated the highest discrepancy between the stress-strain curves obtained from the specimens machined parallel to and perpendicular to the rolling direction. The ultimate tensile strength (UTS) of the HSLA350 specimens cut perpendicular to the rolling direction was about 4% higher than the UTS of the specimens parallel to the rolling direction. For the DP600 material this difference was 2.5%, while for DDQ it was less than 1%. These results provided insight into the degree of in-plane anisotropy of the sheet material utilized to roll form the tubes.

The variation in the stress-strain curves as a function of position around the tube circumference was less than 1% for both the DDQ and DP600 tubes. Therefore the effect of the tube forming operation on the material property variation around the circumference of the tube was considered to be uniform. HSLA350 specimens corresponding to the 6 o'clock location had a lower ductility and higher yield strength compared to 3 and 9 o'clock specimens. The tube fabrication effect on the material properties around the circumference of the HSLA350 tubes was less uniform than for the DDQ and DP600 tubes.

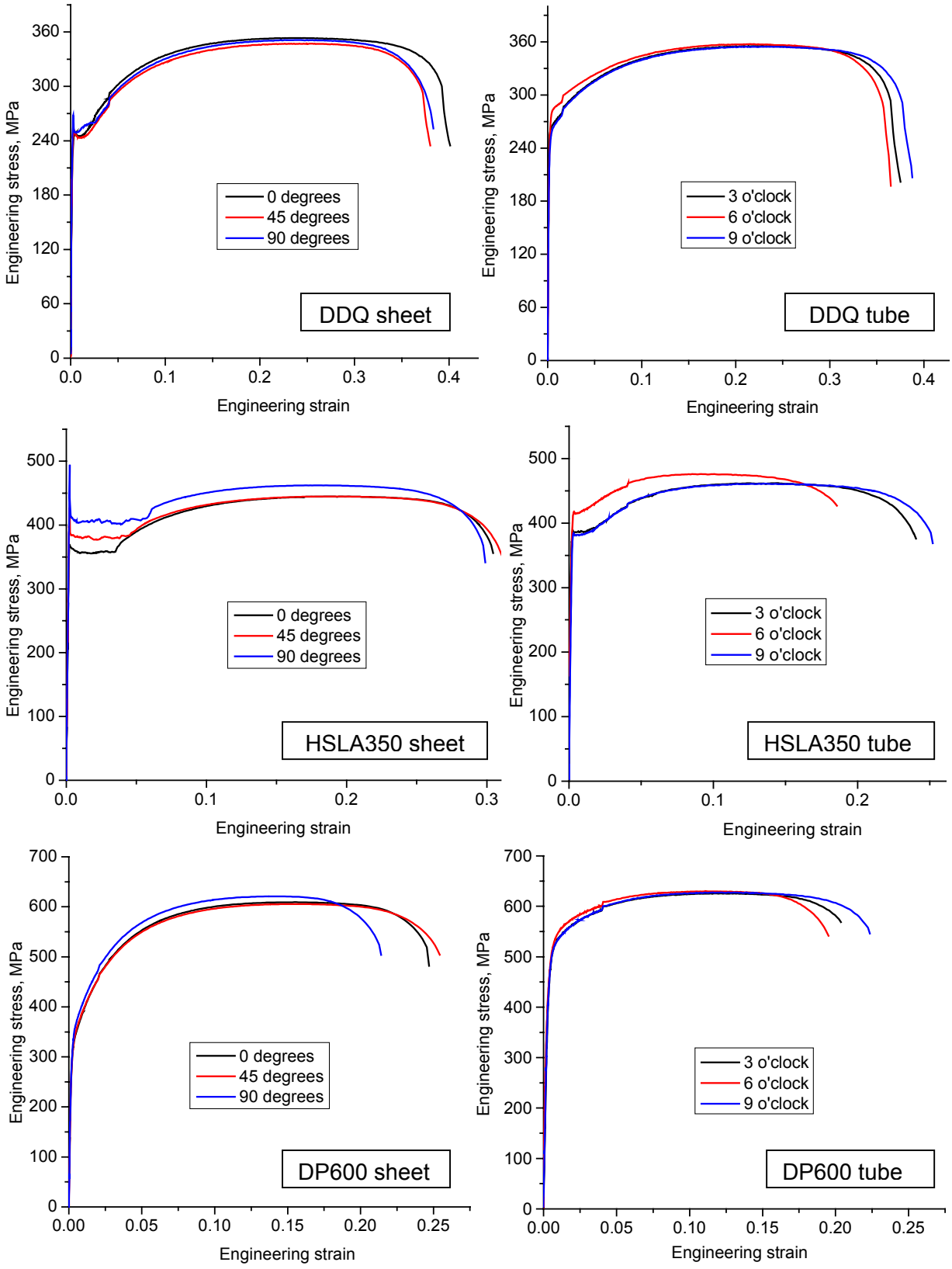

Figure 27: DDQ, HSLA350 and DP600 sheet and tube material properties

A summary of the averaged DDQ, HSLA350 and DP600 sheet and tube material properties is tabulated in Table 1 and shown in Figure 28. The tube material data, shown in the figure, was further utilized to develop material models for the FE tube bending and hydroforming simulations.

Table 1: Summary of sheet and tube material properties

	Sheet		Tube	
	Yield strength, MPa	Ultimate tensile strength, MPa	0.2% offset, MPa	Ultimate tensile strength, MPa
DDQ	250	351	262	356
HSLA350	388	452	396	467
DP600	340	610	471	628

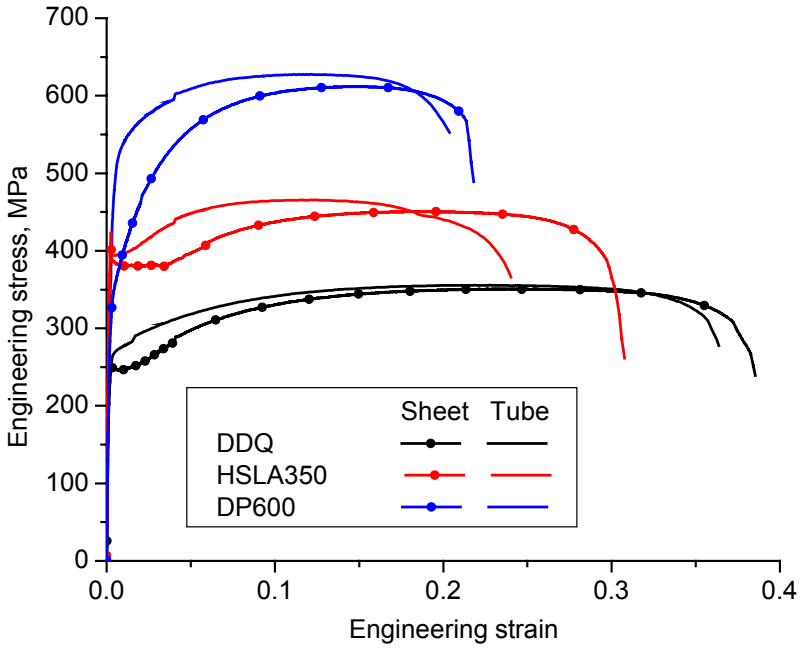

Figure 28: Average engineering stress versus engineering strain curves for DDQ, HSLA350 and DP600

2.2 Tube bending experiments

The tube bending experiments were conducted at the University of Waterloo using an Eagle Precision Technologies EPT 75 mandrel rotary-draw tube bender, shown in Figure 29. A PC-based control and data acquisition system for the tube bender was developed by Dyment [41]. During the test, the system monitored process parameters, including bend die torque, mandrel load and pressure die feed load, and tracked input parameters, including bend die rotation angle, mandrel displacement, pressure die clamping load, pressure die clamp and feed displacements.

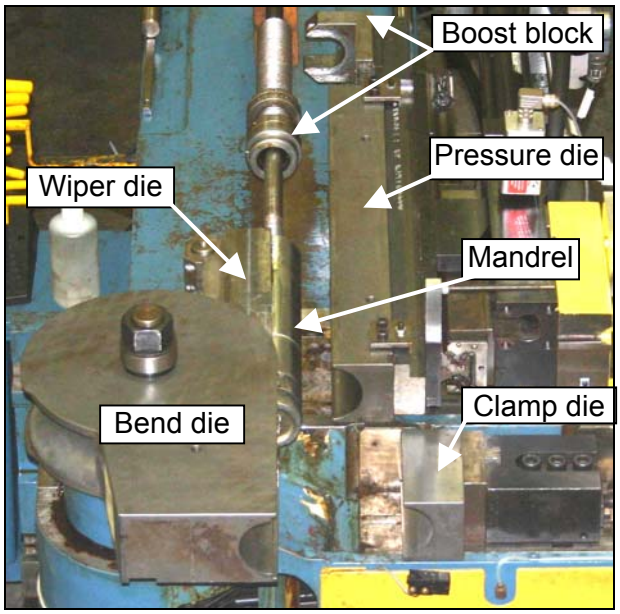

Figure 29: Mandrel rotary-draw tube bender at the University of Waterloo

In the experiments, tubes were bent to a nominal bend angle of 90 degrees. The R/D ratio considered on the experiments was 2.0. The center-line radius of the bend, for R/D=2.0 and tube outer diameter of 76.2 mm (3 in), was 152.4 mm (6 in). To obtain such a bend radius and compensate for radial springback, the center-line radius of the bend die was reduced to 150.4mm (5.921").

A two-ball mandrel was utilized to minimize cross-sectional distortion of the tube during bending. The front edge of the mandrel post was positioned about 0.2 mm behind the point of tangency to reduce excessive material stretching over the mandrel. Before the end of the test the mandrel was retracted to the specified location to eliminate bumps at the end of the bend. Several setup trials were conducted for each alloy to evaluate optimal mandrel position parameters, summarized in Table 2.

A two-piece wiper design, described by Dyment [41], was used in the experiments. The tip of the wiper die was positioned slightly behind the point of tangency. Several trials were conducted for each alloy to determine a wiper die positive rake angle that avoided wrinkling, as summarized in Table 2.

A boost block and a boost block holder attached to the end of the pressure die, as shown in Figure 30, were utilized to prevent pressure die slip. The holder moved together with the pressure die, pushing on the boost block. The shoulder of the boost block pushed on the tube edge so that the tube end moved together with the pressure die. All experiments were conducted at 100% boost level, meaning that pressure die velocity and instantaneous tangential velocity of the center-line of the bend were the same.

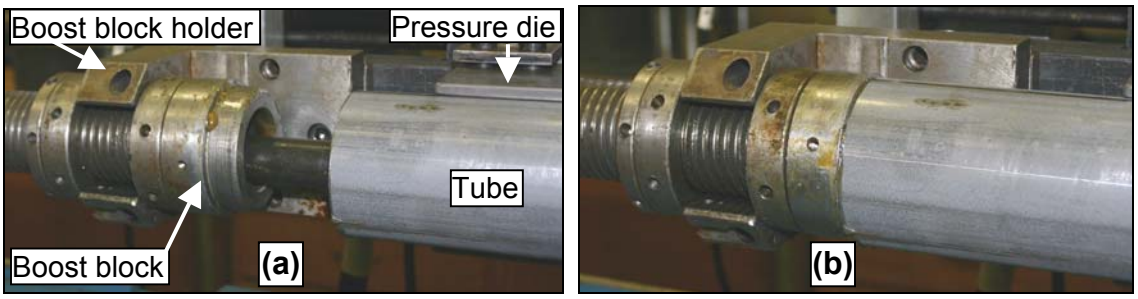

Figure 30: Boost block design: (a) tube retracted; (b) tube engaged with boost block

Springback changed the angle and the radius of the bend after tube bending operation. To account for the radial springback the radius of the bend die was reduced, as mentioned earlier. To compensate for the angular springback, tubes were over-bent to an angle higher than 90 degrees. Several trials for each alloy were conducted to evaluate final bend die rotation angle, producing 90-degree bends after the springback. The values of the bend angle are summarized in Table 2.

After the test each tube was examined to verify the bend angle and to confirm that the pre-bent tube would fit in the hydroforming die. The tube was placed into a template that had the same dimensions as R/D=2.0 pre-bent hydroforming die. If the tube didn't fit in the template, it was rejected and another test was conducted.

2.2.1 Tube bending process parameters

All tubes were bent in 4 seconds. Higher strength steel tubes were over-bent to greater angles due to their inherent higher springback. Higher strength steel grades also required increased pressure die clamping load. The values of pressure die clamping load, bend die rotation angle, mandrel and wiper die position parameters were determined iteratively during several setup trials for each alloy. A summary of the final process parameters adopted for the DDQ, HSLA350 and DP600 tube bending experiments is presented in Table 2.

Table 2: Tube bending process parameters

	DDQ	HSLA350	DP600
Bend time (s)	4	4	4
Prescribed bend angle (degrees)	91.5	92.0	93.0
Approximate bend angle after springback (degrees)	90	90	90
Constant pressure die clamp load (kN)	55	65	75
Pressure die boost (%)	100	100	100
Wiper die rake angel (degrees)	0.2	0.2	0.2
Mandrel location with respect to tangency (mm)	-0.2	-0.2	-0.2
Angle mandrel begins to retract (degrees)	85	85	80
Final mandrel position at max bend angle (mm)	-40	-40	-45
Number of acceptable trials	30	43	40

2.2.2 Tube bending sequence

Before the tube bending test, a liquid lubricant, D.A. Stuart Hydrodraw 615, was manually applied on the outside of the tube in the area of contact with the wiper die. The parts of the tube that were in contact with the clamp, pressure and bend dies were kept dry to increase friction and reduce slip.

The tube was placed over the mandrel and pushed against the shoulder of the boost block, as shown in Figure 30a,b. The tube weld seam was positioned vertically so it remained along the neutral axis of the bend during the test. This ensured a minimum stress level acting onto the weld during the test and reduced the effect of the weld on the results. The clamp die was closed, followed by the pressure die, as shown in Figure 31a. To measure tube slip relative to the clamp die after the end of the test, the tube edge position with respect to the edge of the clamp die was measured at that moment. Hydrodraw 615 lubricant was pumped through the hollow shaft of the mandrel rod through the lubricating channels in the mandrel post, providing lubrication of the inside of the tube and reducing the drag force on the mandrel. The tube was then bent to the prescribed bend angle. The bend die and the clamp die rotated together and the pressure die translated forward, as shown in Figure 31b. The mandrel was set to retract automatically at the end of the bend. After the bend, the tube edge position relative to the edge of the clamp die was measured again to determine clamp die slip. Then, the clamp die was opened, followed by the pressure die, as shown in Figure 31c, and the tube was removed from the tube bender

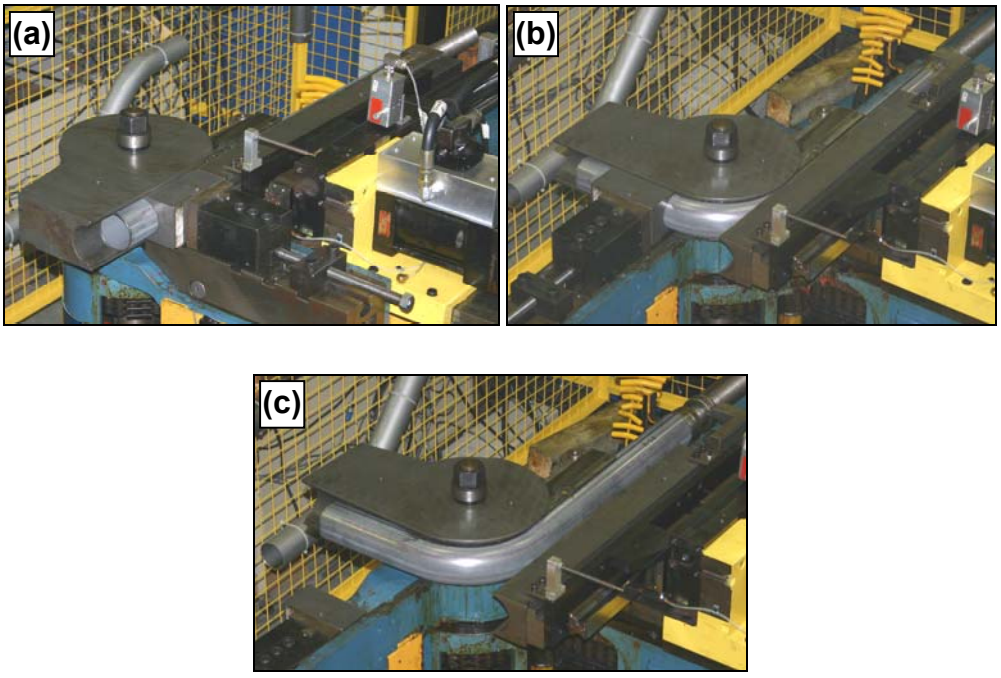

Figure 31: Tube bending sequence (a) after clamping; (b) after rotation of the bend die; (c) after retraction of the bend die, clamp die and pressure die

2.3 Tube hydroforming experiments

Two sets of hydroforming tests were carried out:

- Straight tubes were hydroformed into a square cross-section without any pre-forming;
- Pre-bent tubes were hydroformed into a square cross-section to investigate the effect of pre-bending operation on tube hydroforming.

The Macrodyne 1000-tonne hydroforming press and two 1112 kN (250kip) actuators, utilized in the tube hydroforming experiments, are shown in Figure 32. During the test, a PC-based control and data acquisition system imposed a prescribed axial load versus internal pressure schedule, measured tube corner expansion and monitored die movement, press clamping load, end-feed actuator load and displacement.

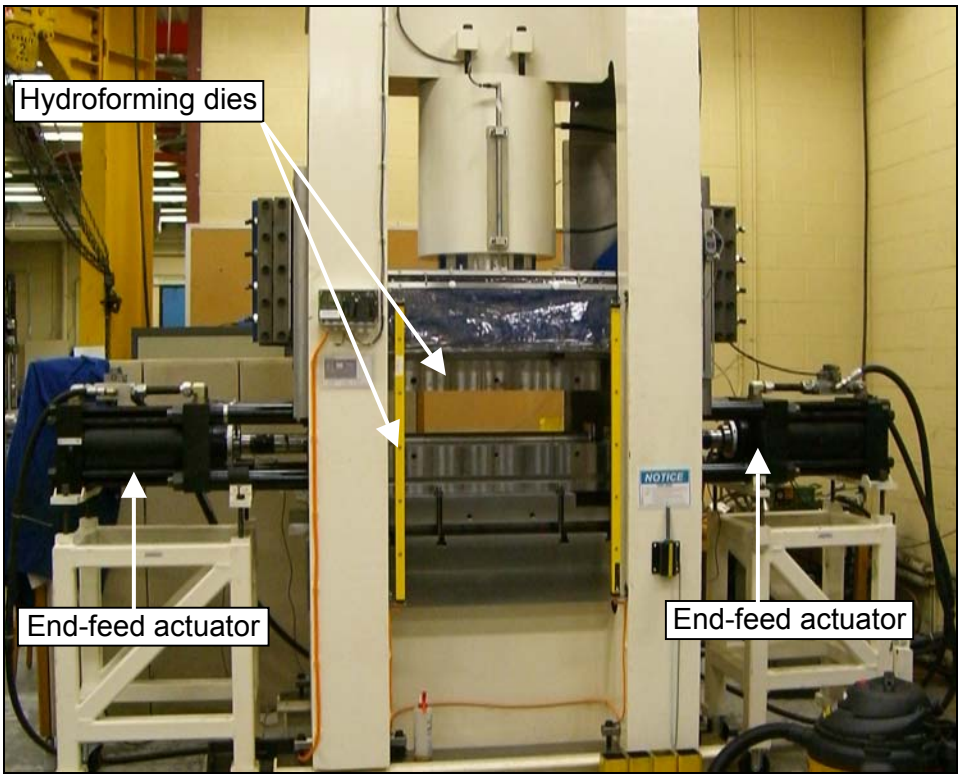

Figure 32: Hydroforming press and end-feed actuators configured for straight tube experiments

Both straight and pre-bent tube hydroforming dies were produced from P20 hardened tool steel. The dies had a square cross-section with corner radii of 6.0 mm and 3.2 mm for the straight and pre-bent hydroforming dies, respectively. To accommodate end-plugs, the dies had two sections of circular

cross-section at each end (Figure 33, Figure 34). The clearance between the tube and the die in both cases was 0.51mm (0.02 in).

Linear variable differential transducers (LVDTs) were utilized to measure tube expansion during the test. In the straight hydroforming die, one LVDT was located in the mid-section and oriented 45 degrees to the top of the die, as shown in Figure 33. In the pre-bent tube hydroforming die, one LVDT was located on the outside of the bend and one on the inside of the bend in the cross-section defined by the bend angle of 45 degrees, as shown in Figure 34.

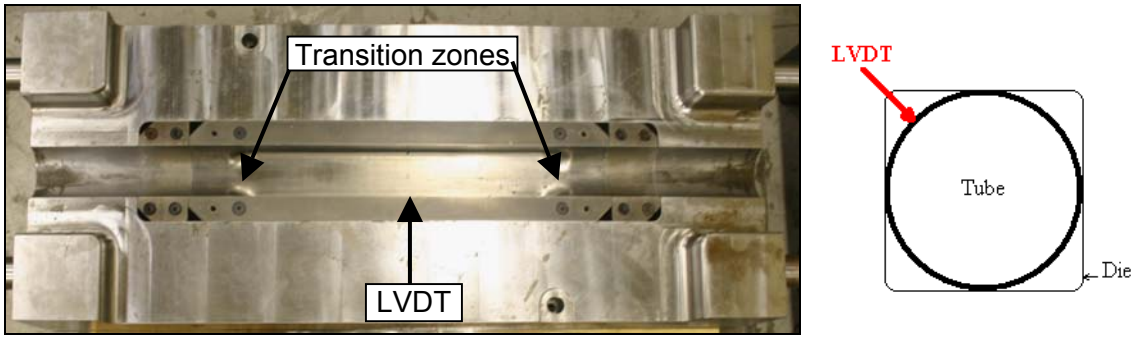

Figure 33: Straight tube hydroforming die and schematic of LVDT location

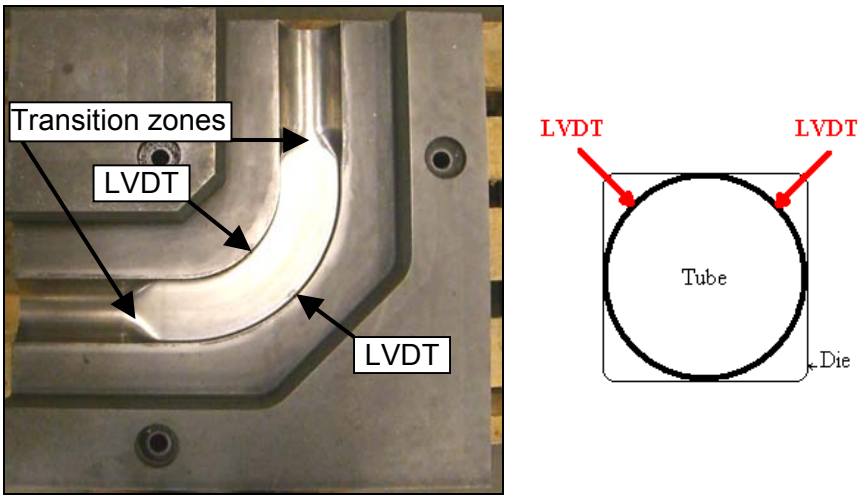

Figure 34: Pre-bent tube hydroforming die and schematic of LVDT location

Tube end-plugs, shown in Figure 35, were mounted on the end-feed actuators, providing sealing of the tube and applying axial load on the tube ends. Parker Polypak O-ring elastomer seals, incorporated in the end-plugs, maintained sealing of the tube. The shoulder of the end-plug exerted the end-feed load directly on the tube edge. The shoulder did not perform any sealing function, because there was no water pressure in the tube end between the shoulder and the O-ring seal.

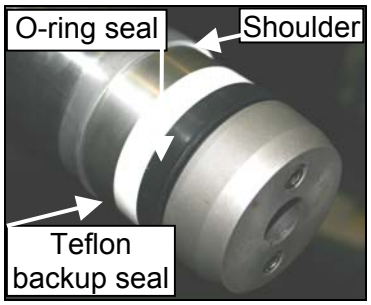

Figure 35: Tube end plug

2.3.1 Tube hydroforming sequence

Before the beginning of straight and pre-bent tube hydroforming tests, the tube was trimmed to fit in the die and a solid film lubricant, D.A. Stuart Hydrodraw 625, was applied on the outside of the tube. After the lubricant dried, the tube was enclosed between the hydroforming dies within the press. End-plugs, mounted on the end-feed actuators were inserted into the tube ends. To ensure initial contact between the shoulder of the plug and the tube edge, an axial force of 4.5 kN (1 kip) was applied to the tube end through the end-plugs. A vacuum was created inside the tube prior to filling the tube with water. The tube was then pressurized either to burst or to the specified internal pressure according to the axial load versus internal pressure schedule. After the end of the test, pressure was relieved from the tube, the end-feed actuators were retracted and the dies were opened. The tube was then removed from the die.

2.3.2 Process parameters and load scheduling

The maximum permissible tube internal pressure in straight and pre-bent tube hydroforming experiments was 151.7 MPa (22 000psi). This limit was imposed by the clamping load capacity of the press. An experiment was interrupted if the tube did not burst at the internal pressure of 151.7 MPa.

An axial load applied in tube hydroforming could be divided in two parts. The first part was required to counteract the internal pressure and prevent the end plugs from being forced out of the tube ends. Additional load, the end-feed force, could also be applied to increase material flow into the expanding zone. While the first part of the axial load was defined by the internal pressure and cross-sectional area of the tube end, the end-feed part could be adjusted to obtain an optimal axial load versus internal pressure schedule for failure-free tube hydroforming.

The first sets of straight and pre-bent tube hydroforming tests were conducted with zero end-feed to examine tube formability without any additional end-feed load. The end plugs were inserted into the

tube ends to maintain sealing and stayed stationary during the test, while the internal pressure was linearly increased.

Several end-feed load versus internal pressure schedules were utilized in higher end-feed tube hydroforming experiments. The schedules incorporated two major principles, outlined in Chapter 1: higher end-feed load should be applied at the initial stages of hydroforming process when the retarding friction forces were lower; while it should be applied with care since early excessive end-feed might cause buckling. As a result, in the straight tube hydroforming experiments, the tube was pre-pressurized without extra end-feed load up to the point when it started to expand. At that moment, the additional end-feed load was applied fully and pressurization continued. This approach is presented schematically in Figure 36.

In zero end-feed straight tube hydroforming of the DDQ, HSLA350 and DP600 tubes, corner expansion initiated when the internal pressure was about 5% of the yield strength of the material. Therefore in higher end-feed straight tube hydroforming all of the tubes were pre-pressurized to 5% of the material yield strength prior to application of the end-feed load.

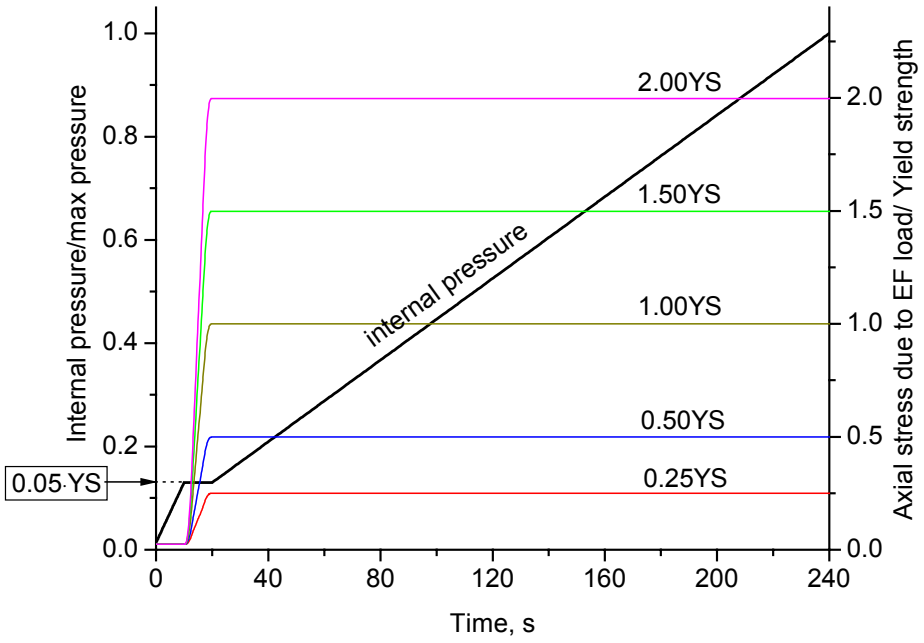

Figure 36: Internal pressure and end-feed load versus time schedules for straight tube hydroforming

Several levels of end-feed load, corresponding to an axial stress level of 0.25, 0.5, 1.0, 1.5 and 2.0 times the yield strength of tube material, were tested for each alloy. These levels are tabulated in Table 3 and are denoted as 0.25YS, 0.50YS, 1.00YS, 1.50YS and 2.0YS.

Table 3: End-feed load for DDQ, HSLA350 and DP600 tube hydroforming

	Yield Strength, MPa	Endfeed load, kN				
		0.25YS	0.50YS	1.00YS	1.50YS	2.00YS
DDQ	262.3	30.2	60.4	120.8	181.2	241.6
HSLA350	395.7	45.7	91.3	182.6	273.9	365.2
DP600	471.0	54.3	108.6	217.2	325.8	434.4

The set of axial load schedules considered for the HSLA350 straight tube hydroforming experiments are shown in Figure 37. At zero end-feed level, the axial load corresponded to the load required to counteract the tube internal pressure only. For higher end-feed cases, additional end-feed load was added at the moment when the tube internal pressure reached 5% of tube yield strength (Figure 37a). The PC-based control system at the University of Waterloo did not allow maintaining internal pressure and end-feed load schedules versus time during the experiment. It could only follow axial load versus internal pressure schedules, presented for HSLA350 straight tube hydroforming in Figure 37b.

The axial load versus internal pressure schedules presented for HSLA350 were similar to those used for the DDQ and DP600 straight tube hydroforming. The actual values of end-feed load for the other alloys were evaluated based on the material yield strength and are tabulated in Table 3. For pre-bent tube hydroforming of DDQ, HSLA350 and DP600 tubes, the same load schedules were utilized as for the straight tube hydroforming.

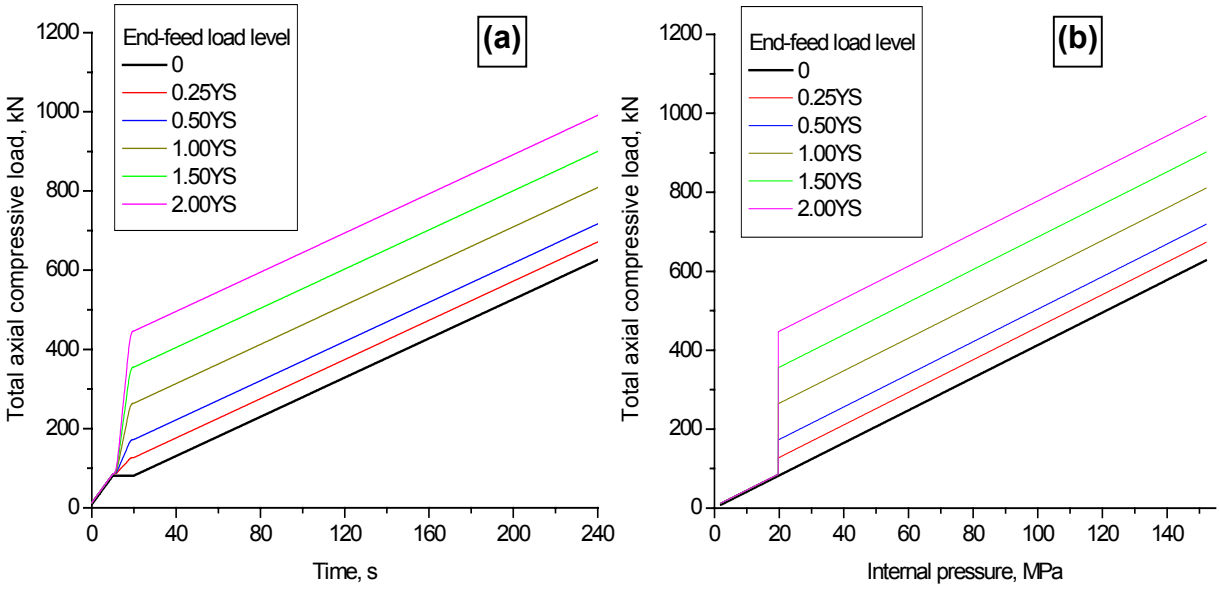

Figure 37: Total axial compressive load schedules for HSLA350 tube hydroforming

2.4 Tube sample preparation

Tubes were cut to 787.4 mm (31 in) for straight hydroforming and to 1016 mm (40 in) for pre-bent hydroforming. After cutting, all tubes were deburred. About one-half of the tubes were electrochemically etched with 2.54 mm (0.1 in) diameter circle grids for post forming strain measurements. The etching technique is discussed in detail by Dyment [41]

For the strain measurements, an image of the circle at the location of interest was captured by a micro-CCD video probe after the tube bending and hydroforming operations. An in-house developed code compared the initial diameter of the circle with the measured major and minor axes of the ellipse after deformation. The ratio of the axes provided the major and minor in-plane components of the engineering strain at the location of the grid. The accuracy in the strain measurement process was roughly ±3% strain [41]. To determine the through-thickness component of strain, an ultrasonic thickness gauge was utilized [41].

Several paths along the directions of the most severe strain and thickness change were chosen for strain and thickness variation measurements, as shown in Figure 38. After bending, these paths included the outside and the inside of the bend, where the most tension/thinning and compression/thickening occurred. In hydroforming, the tubes were mostly expanding circumferentially. Therefore after the hydroforming operation, strains and thickness were measured around the circumference of the tube in the middle cross-section of the straight tube and in the 45-degree bend angle cross-section of the pre-bent tube. To obtain the change in strain and thickness from bending to hydroforming, strains and thickness were measured around the circumference of the tube after the bending operation as well.

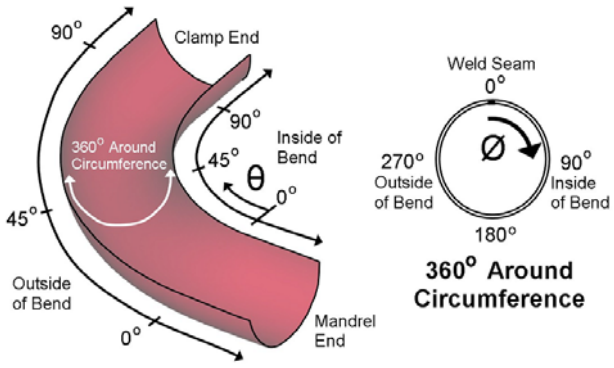

Figure 38: Schematic of strain and thickness measurements for pre-bent tube

After tube bending every second grid was measured along each path. After hydroforming, every grid was measured around the circumference of the tube in order to capture abrupt changes in strain and

thickness distributions. Three tubes were measured per case after bending (9 tubes totally) and only two tubes were measured per case after hydroforming due to the increased number of cases (25 straight and 22 pre-bent tubes).

2.5 Twist compression test

A set of twist compression tests (TCT) was conducted to estimate coefficients of friction (COF) between the tube and the tube bending and hydroforming dies. During a TCT, the sheet material was pressed against a rotating flat tool steel cylinder, as shown in Figure 39a,c. The torque transmitted from the rotating annular cylinder to the lubricated flat sheet specimen was measured (Figure 39b). The contact pressure and relative velocity in the TCT were adjusted to reproduce tribological conditions of corresponding bending or hydroforming process.

DDQ, HSLA350 and DP600 sheet specimens for TCT were cut from the same coils as were utilized to roll form the tubes. The tool steel cylinders mimicked the material of corresponding dies. A summary of contact pairs examined for tube bending and tube hydroforming is presented in Table 4 and Table 5. Several TCT were conducted for each contact pair at different interfacial pressures. Three repeatable tests were carried out for each pressure level. Once the cylinder was used it was reground prior to the next test.

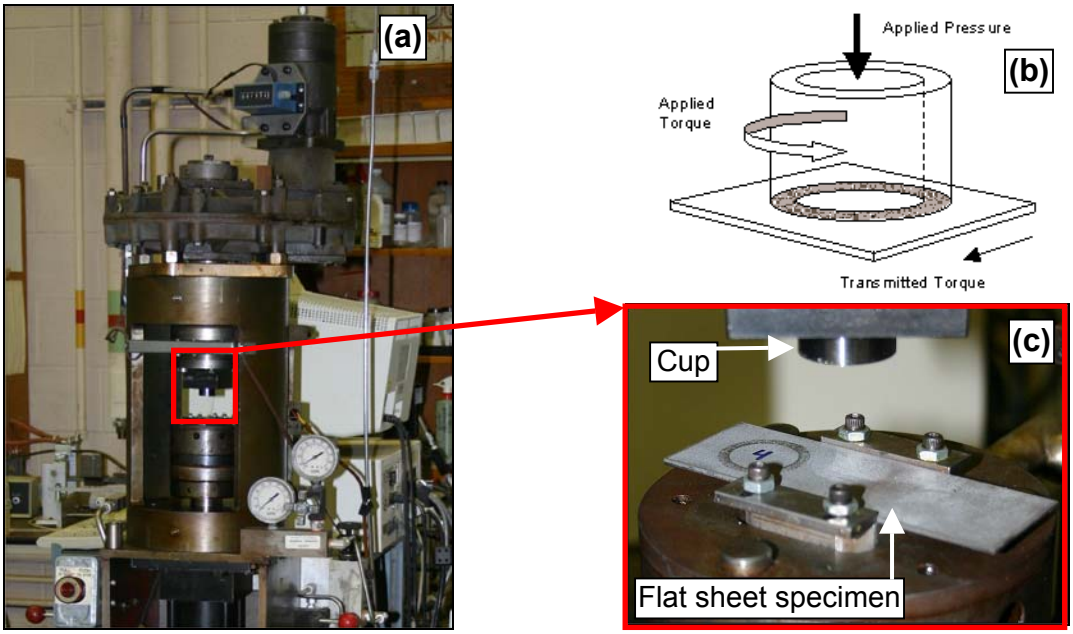

Figure 39: (a), (c) twist compression test setup; (b) schematic of twist compression test

COF versus relative displacement curves for DDQ and HSLA350, representing the tribological conditions of the tube hydroforming test, are shown in Figure 40. Each curve in Figure 40 is an average

of the results obtained from three repeatable tests. The specimens were lubricated with solid film D.A. Stuart Hydrodraw 625 lubricant. Tool steel cups were made of P20 untreated tool steel. Relative velocity was 1 rotation per minute.

The peak at the beginning of the curves corresponded to the static COF. Dynamic COF was estimated based on the averaged COF after the peak. Relative displacement over which the COF was averaged reflected the approximate amount of relative displacement in the corresponding forming process. In the tube hydroforming experiments, the amount of relative displacement between the tube and the die was small, therefore the dynamic COF was estimated based on COF values averaged right after the peak. These values are summarized in Table 4. Due to the limited availability of tool steel cylinders, the COF for tube hydroforming were experimentally determined only for DDQ and HSLA350. The value of dynamic COF for DP600 was obtained by Bardelcik *et al*. [68] and is included in Table 4.

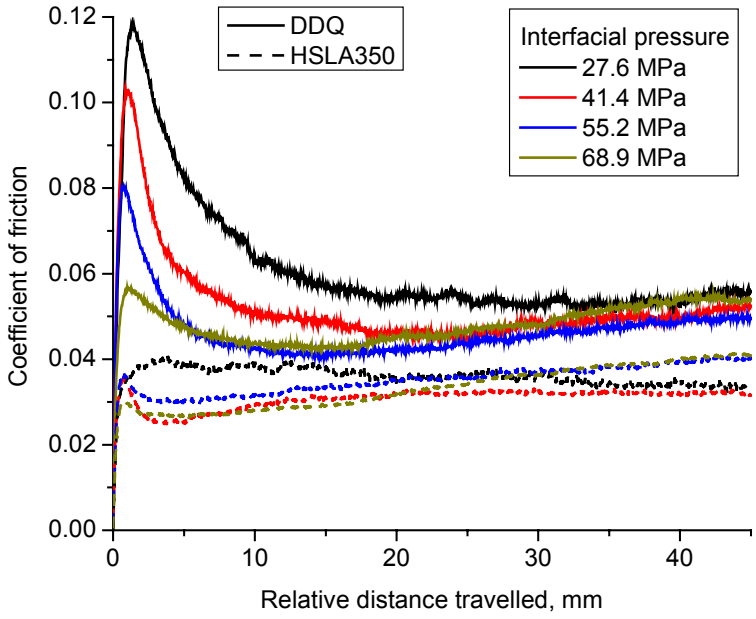

Figure 40: Coefficient of friction for DDQ and HSLA350 tube hydroforming, solid film lubricant

Table 4: Dynamic coefficient of friction for hydroforming die, solid film lubricant

Type of the Die	Material	Lubricant	DDQ	HSLA350	DP600
Hydroforming Die	untreated P20 toolsteel	HydroDraw 625	0.05	0.03	0.035

The COF for tube bending experiments were measured for HSLA350 tube and pressure, clamp, bend and wiper dies. COF for DP600 were obtained by Bardelcik *et al*. [68]. A summary of dynamic COF values for tube bending is presented in Table 5. The solid film lubricant, utilized in tube hydroforming,

significantly decreased friction between the tube and the die compared to the liquid lubricant, utilized in tube bending, or dry contact when no lubricant was applied.

Table 5: Dynamic coefficient of friction for bending dies

Type of the Die	Material	Lubricant	HSLA350	DP600
Pressure/Clamp/Bend Die	untreated 4130HD toolsteel	no	0.14	0.08
Wiper Die	nitrided 4130 toolsteel	HydroDraw 615	0.10	0.04
Mandrel	nitrided 8620 toolsteel, hard chromed	HydroDraw 615	-	0.06

It should be noted that although the presented COF were obtained experimentally, it remained unclear if the values extracted from TCT can be directly related to the COF in tube bending or tube hydroforming due to difference of contact in TCT and tube bending and hydroforming.

Chapter 3
Numerical simulations

This chapter describes the finite element (FE) models utilized in the simulations of the tube bending and straight and pre-bent tube hydroforming operations. All simulations were performed using the commercial explicit dynamic FE code LS-DYNA.

3.1 Material models

A piecewise linear plasticity model [69] was utilized to define the DDQ, HSLA350 and DP600 tube material properties for the FE simulations. Required parameters for this model included the elastic properties and a piecewise linear true effective stress versus true plastic strain curve.

The elastic material properties of the DDQ, HSLA350 and DP600 tubes were specified as follows: Young's modulus $E = 208GPa$ and Poisson's ratio $\nu = 0.29$. The density for the three alloys was $\rho = 7887kg/m^3$.

The effective stress versus true plastic strain curves for DDQ, HSLA350 and DP600 tube material were obtained based on the engineering stress-strain curves, extracted from the quasi-static tensile tests, presented in Figure 28 (Chapter 2). Average tube engineering stress-strain curves were first transformed to obtain the true stress versus true strain data, shown in Figure 41.

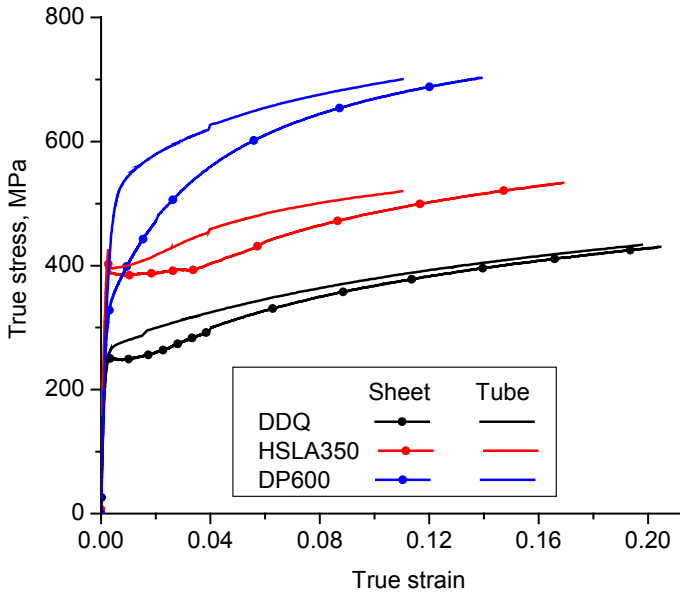

Figure 41: DDQ, HSLA350 and DP600 average true stress versus true strain curves

The tube material stress-strain curves were extrapolated beyond the point of UTS in uni-axial tensile test using tube material terminal n-value. To determine the tube material terminal n-value, true equivalent stress versus true plastic strain curves were plotted in logarithmic scale, as shown in Figure 42a. The slope of the straight line, fit to the experimental data sets in the range of plastic strain in excess of 0.05, determined the tube material terminal n-value. The power law (Equation 1) provided an acceptable fit for DDQ, HSLA350 and DP600 in the higher strain range, but deviated from the experimental data for plastic strains below 0.05, as shown in Figure 42b.

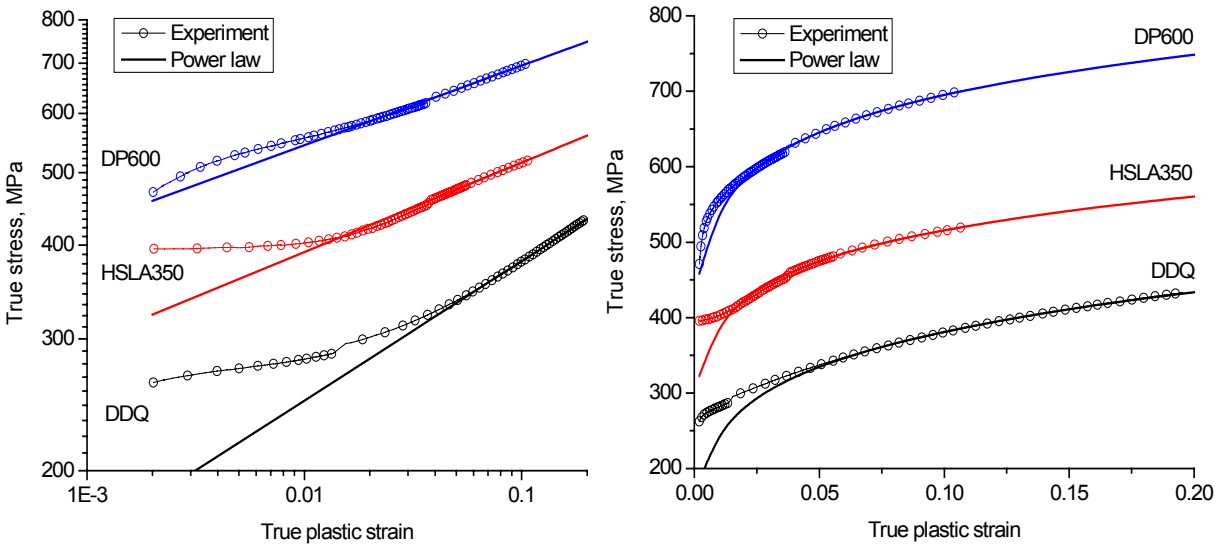

Figure 42: Power law fit for experimental tube true stress versus true plastic strain curves (a) in logarithmic scale; (b) in linear scale

$$\sigma = K\varepsilon^{n} \tag{1}$$

Therefore, for the DDQ, HSLA350 and DP600 piecewise linear plasticity models, true equivalent stress versus true plastic strain curves assumed power law with terminal n-value in the plastic strain range over 0.05. In the plastic strain range below 0.05, corresponding values of stress were based directly upon the experimental data so that at zero plastic strain, the equivalent stress was equal to the yield strength of the tube material, as shown in Figure 43.

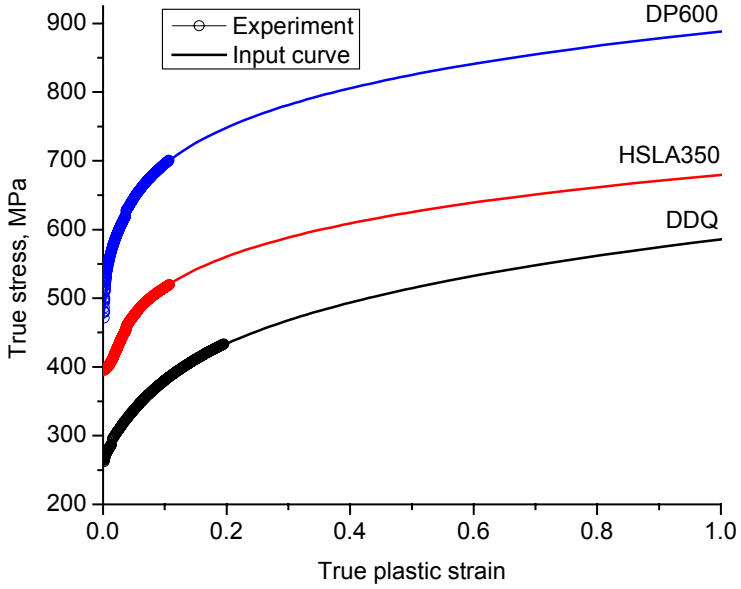

Figure 43: DDQ, HSLA350 and DP600 true equivalent stress versus true plastic strain input curves

A summary of yield strength, K and n-values for DDQ, HSLA350 and DP600 sheet and tube material is presented in Table 6.

Table 6: DDQ, HSLA350 and DP600 sheet and tube material properties

	Sheet			Tube		
	YS, MPa	K, MPa	n	.2% offset, MPa	K, MPa	n
DDQ	250.4	610.9	0.219	262.3	585.6	0.187
HSLA350	387.8	751.6	0.189	395.7	679.5	0.120
DP600	339.6	981.0	0.165	471.0	888.1	0.106

3.2 Tube bending model

The tube bending model utilized in current research was initially developed by Dyment [41]. After the explicit dynamic tube bending simulation, an implicit static springback simulation was carried out. A file containing node information, element connectivity, the effective plastic strains and stress tensors, was written after the bending simulation and further served as an input for the springback simulation. At the end of the springback simulation another forming history file was obtained and transferred to trimming and die closure simulation, which preceded tube hydroforming.

3.2.1 Finite element discretization

The tube bending finite element mesh is shown in Figure 44. The tube bending dies were modeled as rigid bodies using four-noded shell elements. The tube was modeled using 8-noded solid elements with five layers of elements through the thickness of the tube wall. The tube weld seam was not considered in the simulation, therefore only one-half of the model was taken into account with corresponding symmetry boundary conditions. An aspect ratio of solid elements for the tube was between 1:4:4 and 1:5:5. The total number of elements utilized for the tube was 127,500. The total number of elements in the model was 138,465. Compared to using conventional shell elements, the adoption of solid elements significantly increased the computational cost of the simulations. However, the XSFLC method used for failure prediction required the through-thickness component of stress, which is neglected by plane-stress shell elements.

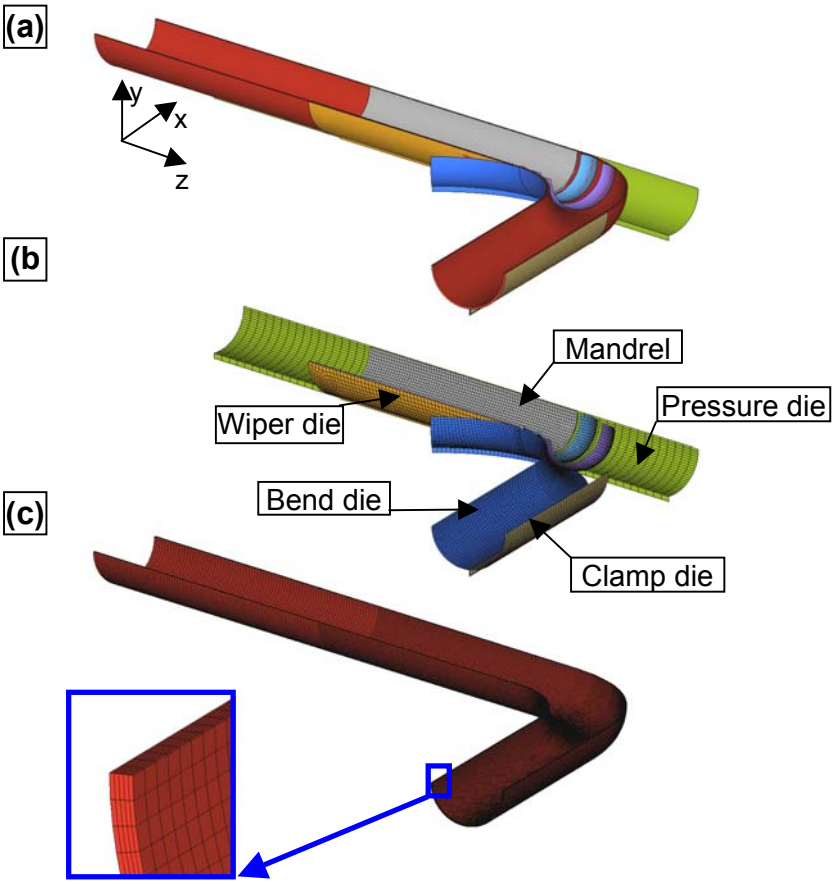

Figure 44: (a) tube bending model; (b) FE mesh of tube bending tooling; (c) FE mesh of the tube

3.2.2 Constraints and loading

Due to the explicit dynamic nature of the solver, the tube bending simulation was accelerated in time to reduce computational cost. For the tube bending simulation a duration of 30 milliseconds was shown by Dyment [41] to be the shortest time that didn't introduce dynamic effects on the predicted strain and thickness in the pre-bent tube.

The boundary conditions and loading schedule utilized in the tube bending simulation corresponded to those in the experiments. In addition, symmetry boundary conditions were applied to all the nodes of the tube in the symmetry plane. The degrees of freedom for each of the tools in the simulation, with respect to the axes shown in Figure 44, are summarized in Table 7. The tube had only symmetry constraints and the end of the tube was prescribed to move together with the pressure die at 100% boost level.

Table 7: Degrees of freedom in tube bending

Tool	DOF
Bend die	Y-rotation
Pressure die	X, Z-translation
Clamp die	X-translation, Y-rotation
Wiper die	fully fixed
Mandrel	free

The loading and displacement curves, utilized for various dies in tube bending, are presented in Figure 45. The clamp die was closed under displacement control in the x-direction within the first 3 milliseconds, as shown in Figure 45a. The pressure die was closed and the clamp load was applied in the x-direction within the first six milliseconds of the simulation (Figure 45b). The bend and the clamp dies started to rotate about the y-axis at 6 milliseconds (Figure 45c) and the pressure die translated along the z-axis to match the bend die rotation at a boost level of 100% (Figure 45d). The bend was completed in a period of 24 milliseconds. The mandrel started to retract when the rotation of the bend reached the angle, corresponding to the angle when the mandrel was retracted in the experiments (Figure 45e). The loading and motion curves presented in Figure 45 were utilized for the DDQ tube bending simulation. These curves were typical for the HSLA350 and DP600 tube bending operations. The particular values of maximum displacement, rotation angle, and load utilized in the DDQ, HSLA350 and DP600 tube bending simulations corresponded to the experimental values summarized in Table 2.

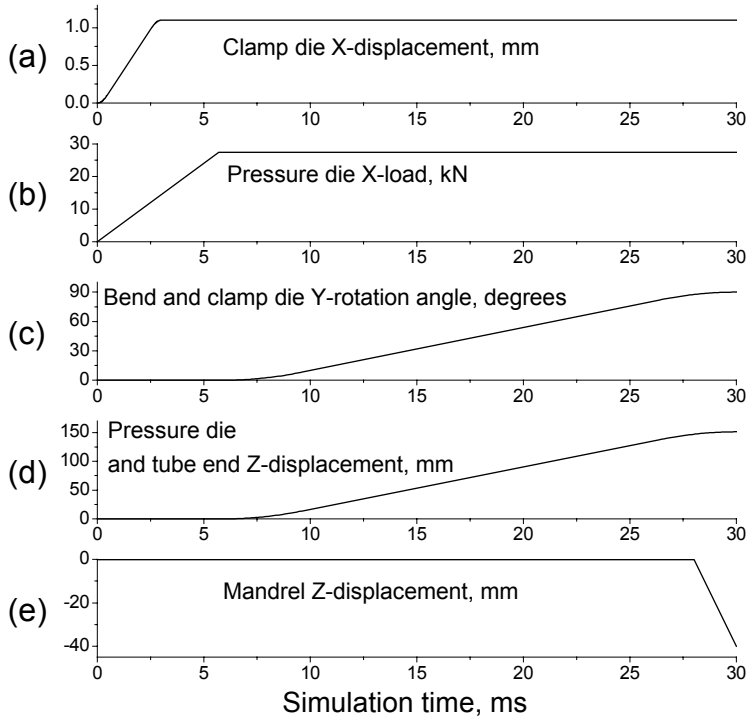

Figure 45: Motion and loading schedule of dies in tube bending simulation

3.2.3 Contact and friction

A penalty stiffness-based surface-to-surface contact algorithm in LS-DYNA [69] was utilized to model contact interaction between the tube and rigid tooling. This algorithm required prescribed dynamic and static coefficients of friction (COF), which were assumed to be equal. Two sets of COF (Table 8), based on the results of the TCT, conducted on HSLA350 and DP600 specimens, as described in Chapter 2 (Table 5), were utilized in the DDQ, HSLA350 and DP600 tube bending simulations to evaluate the effect of increased COF in tube bending simulations. Although the COF between the tube and the mandrel was not obtained experimentally for the higher COF set due to the shortage of corresponding tool steel cylinders, a value of 0.10 was assumed in order to demonstrate the effect of a higher COF.

Table 8: Higher and lower sets of COF utilized in tube bending simulations

Type of the Die	Higher COF (HSLA350)	Lower COF (DP600)
Pressure/Clamp/Bend Die	0.14	0.08
Wiper Die	0.10	0.04
Mandrel	0.10	0.06

3.3 Tube hydroforming models

Straight tube hydroforming required a one-step simulation. The pre-bent tube hydroforming model utilized a multi-step simulation that used a file with the tube forming history, transferred from the bending, springback and die closure simulations. Elements, corresponding to the ends of the tube trimmed after the bending operation in the experiments, were manually deleted from the forming history file before the die closure operation. An output file from die closure step was used as an input for the hydroforming simulation.

3.3.1 Finite element discretization

The straight and pre-bent tube hydroforming dies and end-feed plugs were modeled as rigid bodies using four-noded shell elements.

In straight tube hydroforming, the tube was modeled using 8-noded solid elements with five layers of elements through the thickness of the tube wall. The tube weld seam was not considered in the simulation, and only one-eighth of the model was taken into account, with corresponding symmetry boundary conditions. The aspect ratio of solid elements of the tube was between 1:4:4 and 1:5:5. The total number of elements utilized for the tube was 105,000. The total number of elements in the model was 133,594.

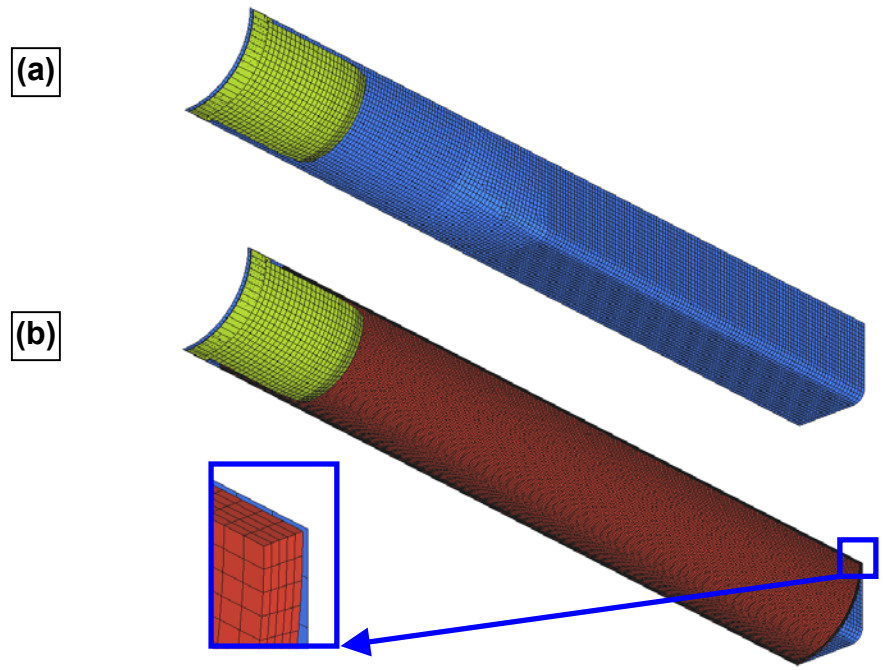

Figure 46: (a) hydroforming die and end-feed plug mesh; (b) tube, die and end-feed plug mesh

In the pre-bent tube hydroforming simulation the tube, hydroforming die and end-feed plug mesh were extracted from the output of the die closure simulation. The sequence of the results after the springback and die closure simulations is presented in Figure 47. After the springback (Figure 47a) the tube was trimmed to fit within the hydroforming die (Figure 47b). Then the die was closed, and end-feed plugs were inserted in the tube ends (Figure 47c,d). The tube forming history was transferred through the sequence of the simulations to the hydroforming simulation.

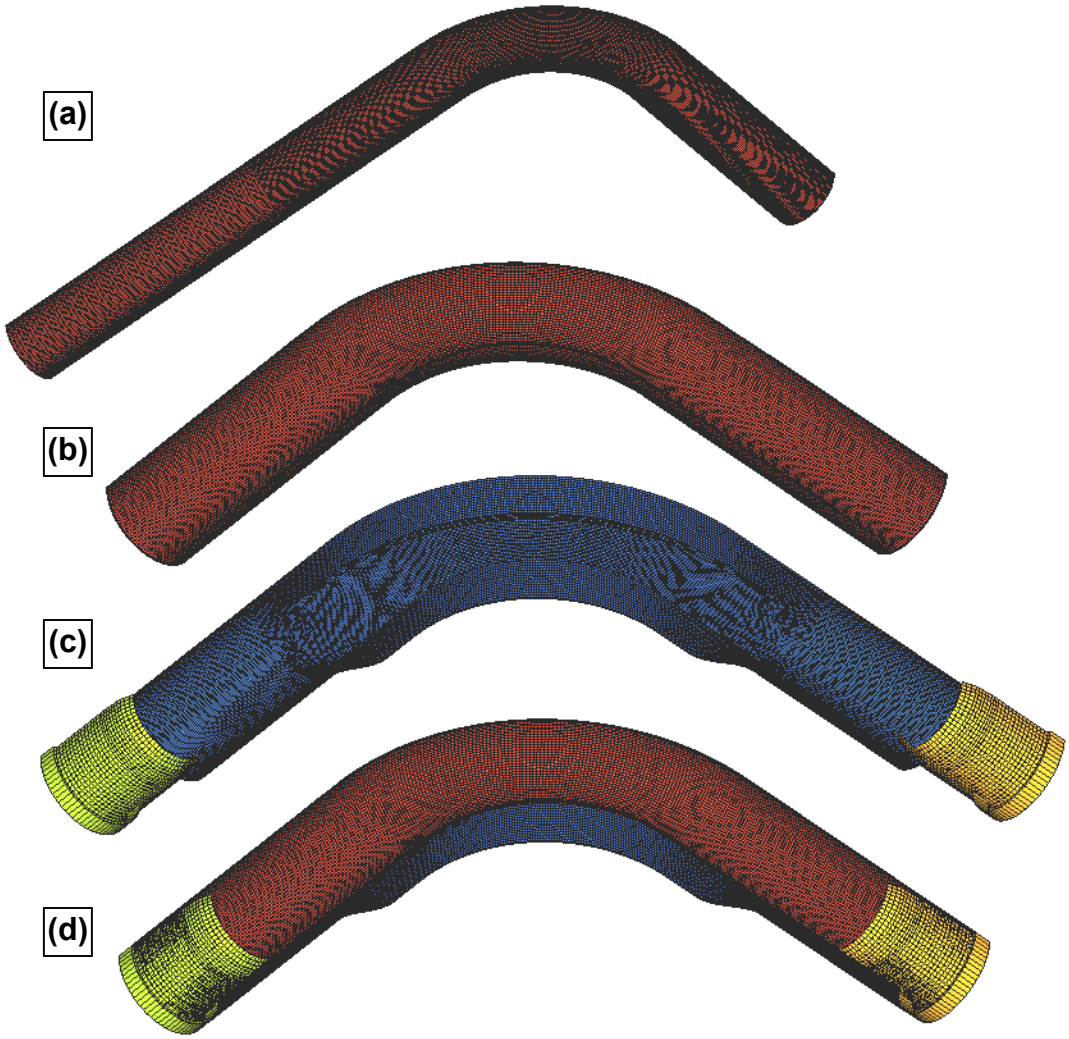

Figure 47: (a) tube after springback; (b) trimmed tube before die closure; (c) hydroforming die and end-feed plugs; (d) tube after die closure and before tube hydroforming

3.3.2 Constraints and loading

Due to explicit nature of the solver, the straight and pre-bent tube hydroforming simulations were accelerated. The end-feed versus internal pressure loading schedule, utilized in the experiments and presented in Figure 36, was scaled over 25 ms and utilized in the simulations.

The boundary conditions applied in the simulations corresponded to the experimental constraints. The straight and pre-bent tube hydroforming dies were fully constrained, while the end-feed plugs were allowed to translate in the axial direction of the tube. All nodes of the tube in the symmetry planes were constrained using symmetry boundary conditions.

3.3.3 Contact and friction

A penalty stiffness-based surface-to-surface contact algorithm in LS-DYNA [69] was utilized to model contact interaction between the tube and rigid tooling. The dynamic and static COFs in the contact algorithm were assumed to be equal. The effect of friction coefficient between the tube and the hydroforming die was investigated in the straight tube hydroforming simulations. Values of COF between 0.01 and 0.04 were simulated for HSLA350 and DP600 and between 0.01 and 0.05 for DDQ straight tube hydroforming. As a result, the effect of COF on predicted tube end displacement, tube corner expansion and failure prediction using the XSFLC method was obtained parametrically. In addition, the correlation between the COF required for the contact algorithm in the simulation and that measured using the TCT was analyzed. Based on this analysis, the COFs for the pre-bent tube hydroforming simulations were determined.

Chapter 4

Determination of Tube Extended Stress-Based Forming Limit Curve

In the current chapter strain-based FLCs are estimated for the DDQ, HSLA350 and DP600 tubes based on the results of tube free expansion testing. The estimated strain-based FLCs are transformed into XSFLCs [58,59,62], which are further utilized for failure prediction in FE tube hydroforming simulations.

4.1 Tube free expansion test and simulation

Tube free expansion tests were performed by van Riemsdijk *et al.* [36] on the tubes fabricated from the same coils as utilized for the hydroforming experiments. The tubes had 76.2 mm (3 in) outer diameter and were cut to a length of 469.9 mm (18.5 in) to allow 152.4 mm (6 in) of tube length to expand between the grips (Figure 48). The tubes were pressurized from the inside to failure. Three tubes per alloy were tested and tube radial expansion versus internal pressure data was recorded. The experimental procedure and tooling are described in detail by Chen *et al.* [54].

FE simulation of the tube free expansion tests considered one eighth of the expanding part of the tube with corresponding symmetry boundary conditions, as shown in Figure 48. The tube was modeled using 8-noded solid elements with five layers of elements through the thickness of the tube. The aspect

ratio of solid elements was 1:4:4. Along the edge, where the tube was gripped in the experiments, all nodes were fully constrained.

The tube internal pressure was applied using a control volume option available in LS-DYNA [69]. This feature allows prescribing either pressure or volume control boundary conditions. Under the pressure control volume option, the tube internal pressure was an input parameter and was increased linearly with time. Under volume control, the mass inflow rate of the pressure medium was an input parameter and was held constant, while the internal pressure became an output parameter. The volume control approach better reflected the experimental process, where the inflow rate was physically controlled in the hydraulic system.

In the tube free expansion experiments, the internal pressure increased to a maximum and then decreased, being lower at burst. The simulations under volume control captured the peak in the internal pressure versus radial expansion curve. Under pressure control this was impossible since the loading became unstable after the peak pressure was reached. The measured and predicted internal pressure versus radial expansion curves using both types of control are presented in Figure 49 and Figure 50.

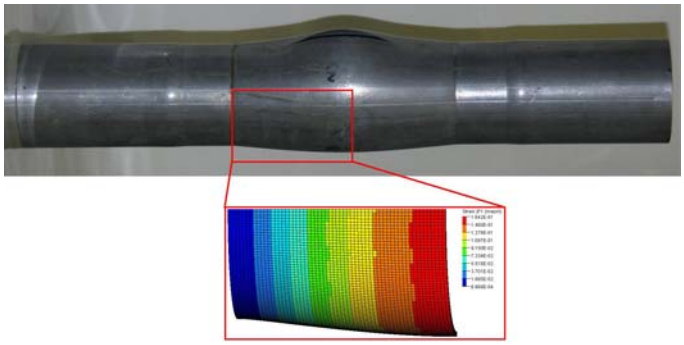

Figure 48: HSLA350 tube after tube free expansion burst test and corresponding plastic strain distribution from FE simulation

The predicted maximum pressure using the volume control approach was within 1% of the measured value for all three alloys. The predicted tube radial expansion at the peak pressure was slightly under-estimated. However the existence of the plateau in the measured and predicted internal pressure versus radial expansion curves prevented determination of the exact radial expansion corresponding to the maximum pressure. A summary of the measured and predicted peak pressure and corresponding radial expansion for the DDQ, HSLA350 and DP600 tube free expansion tests is tabulated in Table 9.

Comparison of the predicted and measured results from the tube free expansion tests enabled validation of the material stress-strain input data for further tube bending and tube hydroforming simulations. In

the tube free expansion test simulations, the stress-strain curve was the only input characteristic of the material. The material properties utilized in these models produced good agreement between predicted and measured tube expansion for DDQ, HSLA350 and DP600 and therefore could be further used in other tube forming simulations.

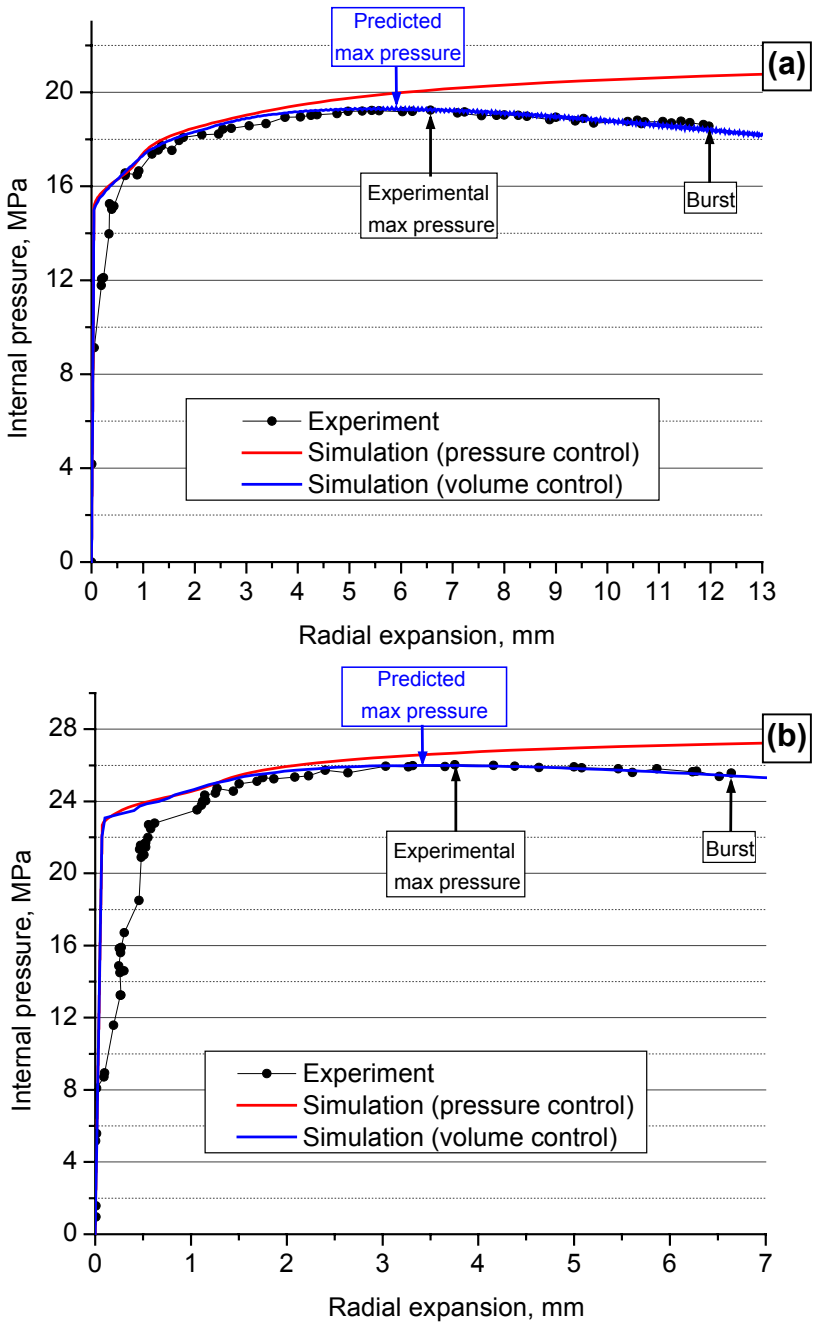

Figure 49: (a) DDQ and (b) HSLA350 tube internal pressure versus radial expansion in tube free expansion test

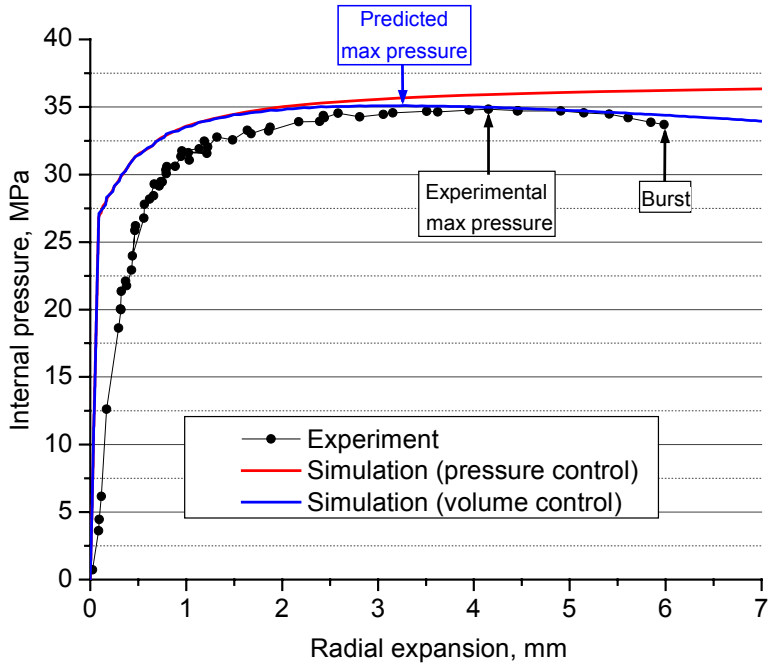

Figure 50: DP600 tube internal pressure versus radial expansion in tube free expansion test

Table 9: Experimental and predicted tube maximum pressure and corresponding radial expansion

	Radial expansion, mm		Maximum pressure, MPa	
	Experimental	Predicted	Experimental	Predicted
DDQ	6.57	5.91	19.2	19.1
HSLA350	3.76	3.43	26.0	26.0
DP600	4.15	3.28	34.8	35.1

4.2 Estimation of tube strain-based FLC

In the tube free expansion tests, failure occurred in the middle cross-section of the tube. At the onset of necking, the strain in the tube corresponded to the intersection point between the strain path of the material and the tube strain-based FLC. This strain at the onset of necking corresponds to the average strain in the middle cross-section around the circumference of the tube.

The tube free expansion tests were carried out with "nearly-constrained" ends of the tube. Chen *et al.* [54] experimentally measured the axial strain in the middle cross-section of the tube in the free expansion test, conducted using the same experimental setup and the same constraints as in current research. The axial strain appeared to be negligible during the tests, being less than 0.7% strain at burst, as shown in Figure 51. This confirmed that the tube material in the middle cross-section of the tube follows a "near-plane strain" path.

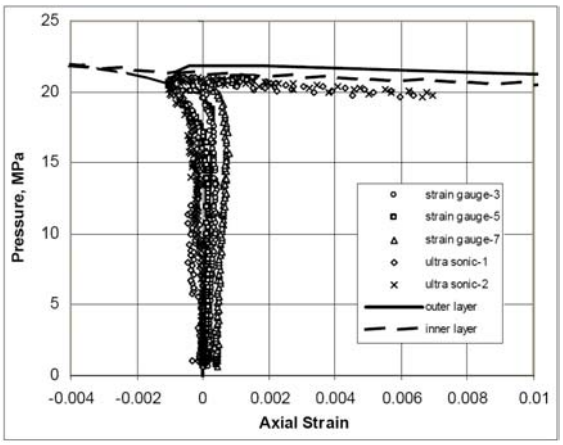

Figure 51: Axial strain in tube free expansion test [54]

The strain at the onset of necking in the tube free expansion tests then corresponded to the plane strain intercept of the strain-based FLC for the tube. Unfortunately, strain measurements at the onset of necking in the tube free expansion test were not conducted by van Riemsdijk *et al.* [36]. Therefore direct calibration of the tube strain-based FLC using the results of the tube free expansion tests was not possible in the current work. Instead, the tube internal pressure versus radial expansion curves, measured during the tests, were used to estimate the lower and upper bounds for the average strain in the mid-section of the tube at the onset of necking. The lower limit was taken as the strain attained at the peak pressure, because a neck could not initiate before the peak pressure. The upper limit corresponds to the strain attained at burst, because necking would initiate prior to burst.

To obtain lower and upper limits for the major strain in the mid-section of the tube at the onset of necking, the circumferential strain was extracted from FE simulations of the tube free expansion tests. The strain, predicted at the time step when radial expansion in the simulation was equal to the measured expansion at peak pressure, produced the lower limit for the major strain at the onset of necking. The circumferential strain predicted when the tube expansion in the simulation was equal to the measured expansion at burst pressure, produced the upper limit. The measured radial expansions at both peak and burst pressures, together with the corresponding predicted circumferential strains, are tabulated in Table 10.

Table 10: Experimental tube expansion at maximum pressure and at tube burst and corresponding predicted true major strains

	Experimental radial expansion, mm		Predicted True major strain, %		
	at max pressure	at burst	at max pressure	at burst	Keeler-Brazier approximation
DDQ	6.57	11.97	16.3	27.9	36.7
HSLA350	3.76	6.64	9.7	16.5	25.0
DP600	4.15	5.99	10.6	15.0	22.6

For all three tube materials, DDQ, HSLA350 and DP600, the shape of the strain-based FLC was assumed to be the same as that obtained using the Keeler and Goodwin [55] approximation, while the level of the tube FLC was determined by the lower and upper limits for the plane strain intercept based on the tube free expansion tests. The calculated upper and lower limits of the tube FLC for three alloys are presented in Figure 52, Figure 53 and Figure 54. The predicted strain path of the elements in the mid-section of the tube is also presented in the graphs.

A third FLC was also calculated utilizing with the plane strain intercept based on Keeler-Brazier approximation [55], using the tube wall thickness and tube terminal n-value, and is also included in the graphs for each alloy. Although the Keeler-Brazier approximation is a conventional approach utilized for sheet steel, it can be seen that when applied to predict the tube free expansion it significantly over-predicts the strain and radial expansion at the onset of necking. The values of plane strain intercept, predicted by the Keeler-Brazier approximation for all three alloys are also tabulated in Table 10.

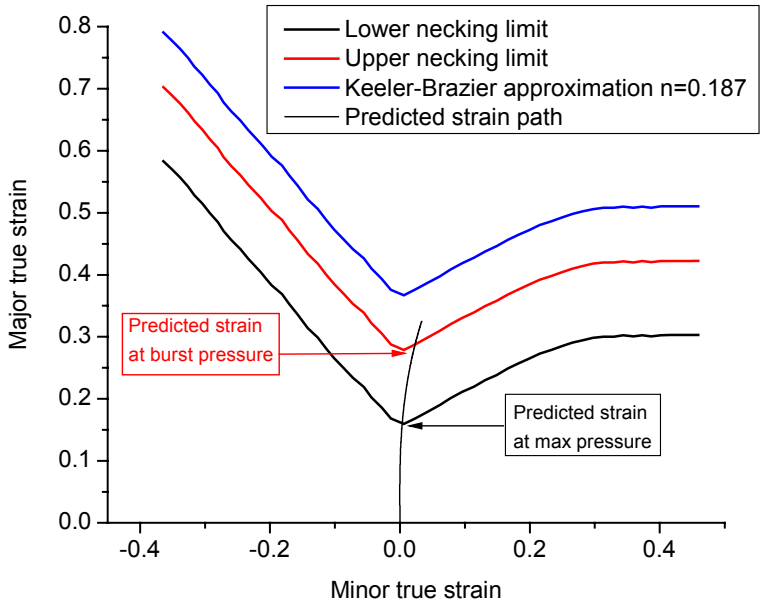

Figure 52: Upper and lower limits for DDQ tube strain-based FLC

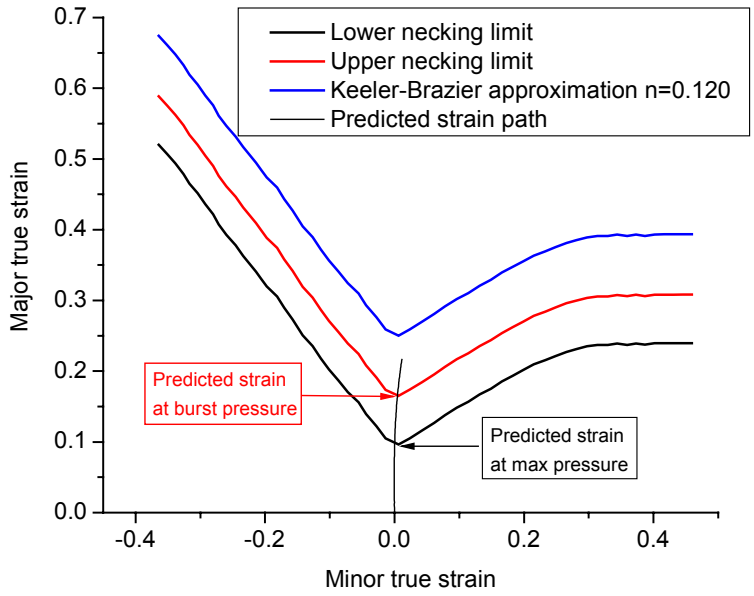

Figure 53: Upper and lower limits for HSLA350 tube strain-based FLC

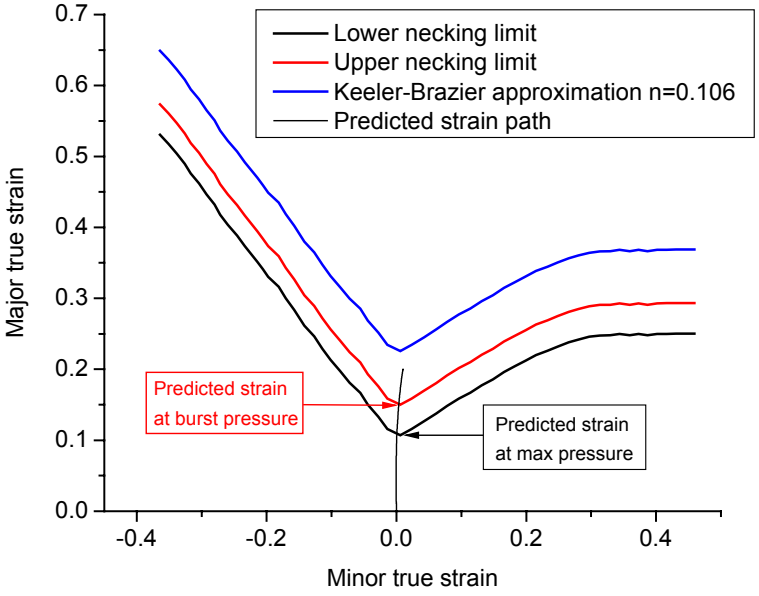

Figure 54: Upper and lower limits for DP600 tube strain-based FLC

4.3 Tube Extended Stress-Based Forming Limit curves

The upper and lower limits of the tube FLC for each alloy were transformed into principal stress space according to the procedure presented by Stoughton [57], as shown in Figure 55. Stress-based FLCs were then transformed into invariant stress space to obtain XSFLCs according to the procedure proposed by Simha *et al.* [58], as shown in Figure 56. These XSFLCs were further utilized to determine the onset of necking in tube hydroforming simulations. Note that forming limits utilizing the Keeler-

Brazier plane strain intercepts were well above the upper limit curves from the tube free expansion experiments and were not considered further in this research.

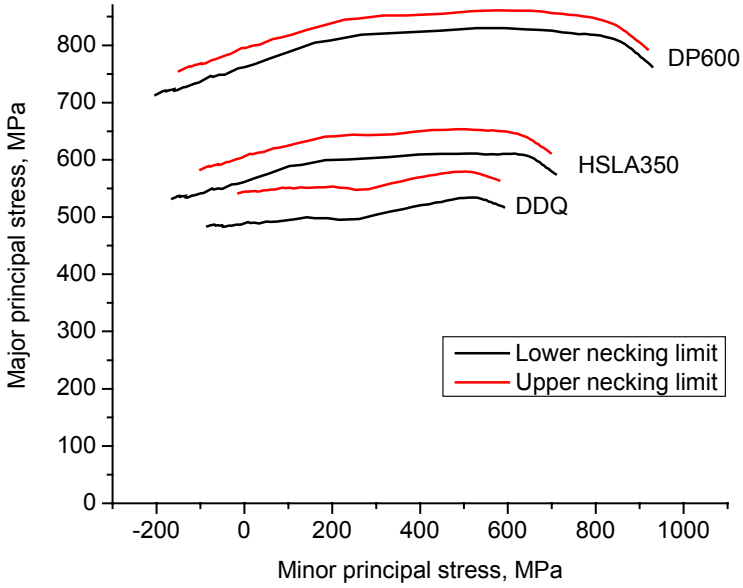

Figure 55: Stress-based FLCs for DDQ, HSLA350 and DP600 tubes

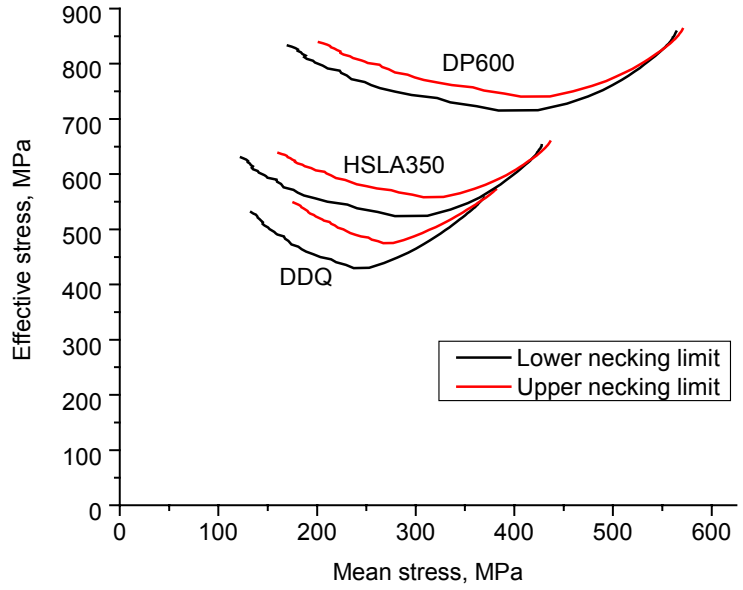

Figure 56: XSFLCs for DDQ, HSLA350 and DP600 tubes

Chapter 5
Results from the tube bending and hydroforming experiments

In this chapter, the results of the tube bending and straight and pre-bent tube hydroforming experiments are presented. The effect of increased end-feed load on resulting tube formability, as well as strain and thickness distributions in tube hydroforming is discussed in detail.

5.1 Tube bending experimental results

5.1.1 Process parameters

The process parameters monitored during the DP600 tube bending tests are presented in Figure 57 to demonstrate repeatability of the experiments. The bend die torque, pressure die boost load and mandrel load histories summarize the results obtained from 40 experiments. The low level of scatter for the DP600 tube bends was typical for the DDQ and HSLA350 tube bending (not shown for brevity). Therefore, average curves were calculated and utilized to compare process parameters for the three alloys.

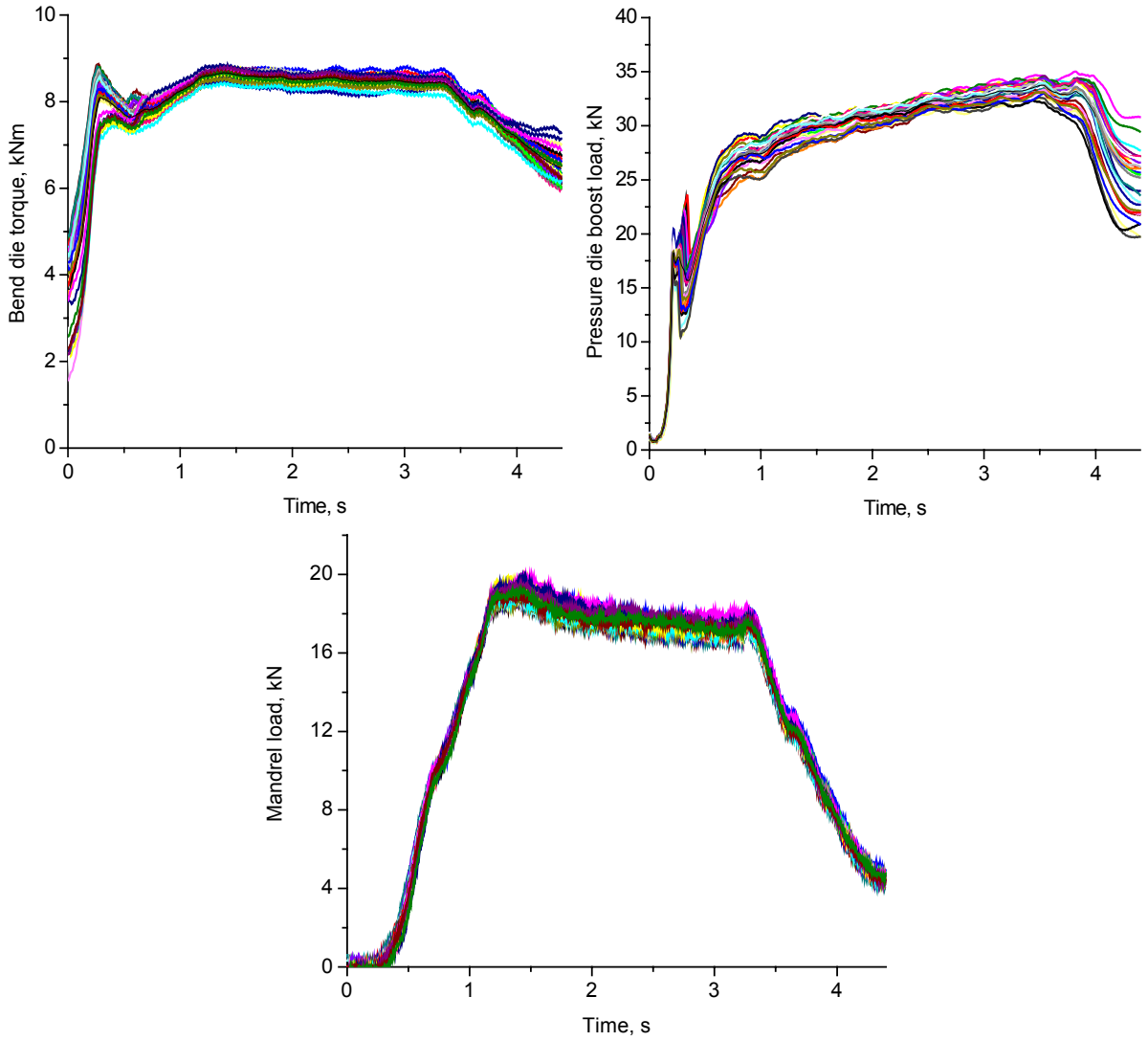

Figure 57: Process variables for DP600 tube bending

Averaged bend die torque, pressure die boost load and mandrel load curves for DDQ, HSLA350 and DP600 tube bending are shown in Figure 58. The curves labeled “dry run” are the loads required to move the dies without a tube and represent the level of frictional loss in the apparatus. The increase of material strength from DDQ to DP600 had a significant effect on the increase of bend die torque and pressure die boost load. The boost block and boost block holder, attached to the end of the pressure die to eliminate slip (Section 2.2), accounted for the increase of pressure die boost load towards the end of the experiment. Without a boost block, pressure die slip would increase during the test and would limit the level of pressure die boost force.

The tube mandrel load primarily depended on the pressure die clamping load and friction between the mandrel and the inside of the tube. Higher clamping load reduced the clearance between the tube and the mandrel, decreasing the thickness of lubricant layer and increasing friction. The DDQ, HSLA350

and DP600 bends utilized the same lubricant and had the same initial clearance between the mandrel and the tube, while the pressure die clamping load was 55 kN, 65 kN and 75 kN correspondingly. The hot-rolled DDQ tubes had a rougher surface finish and higher friction, compared to the cold-rolled HSLA350 and DP600 tubes. Therefore, the cumulative effect of higher friction and lower pressure die clamping load for DDQ bends resulted in the same amount of mandrel load in the DDQ and HSLA350 experiments.

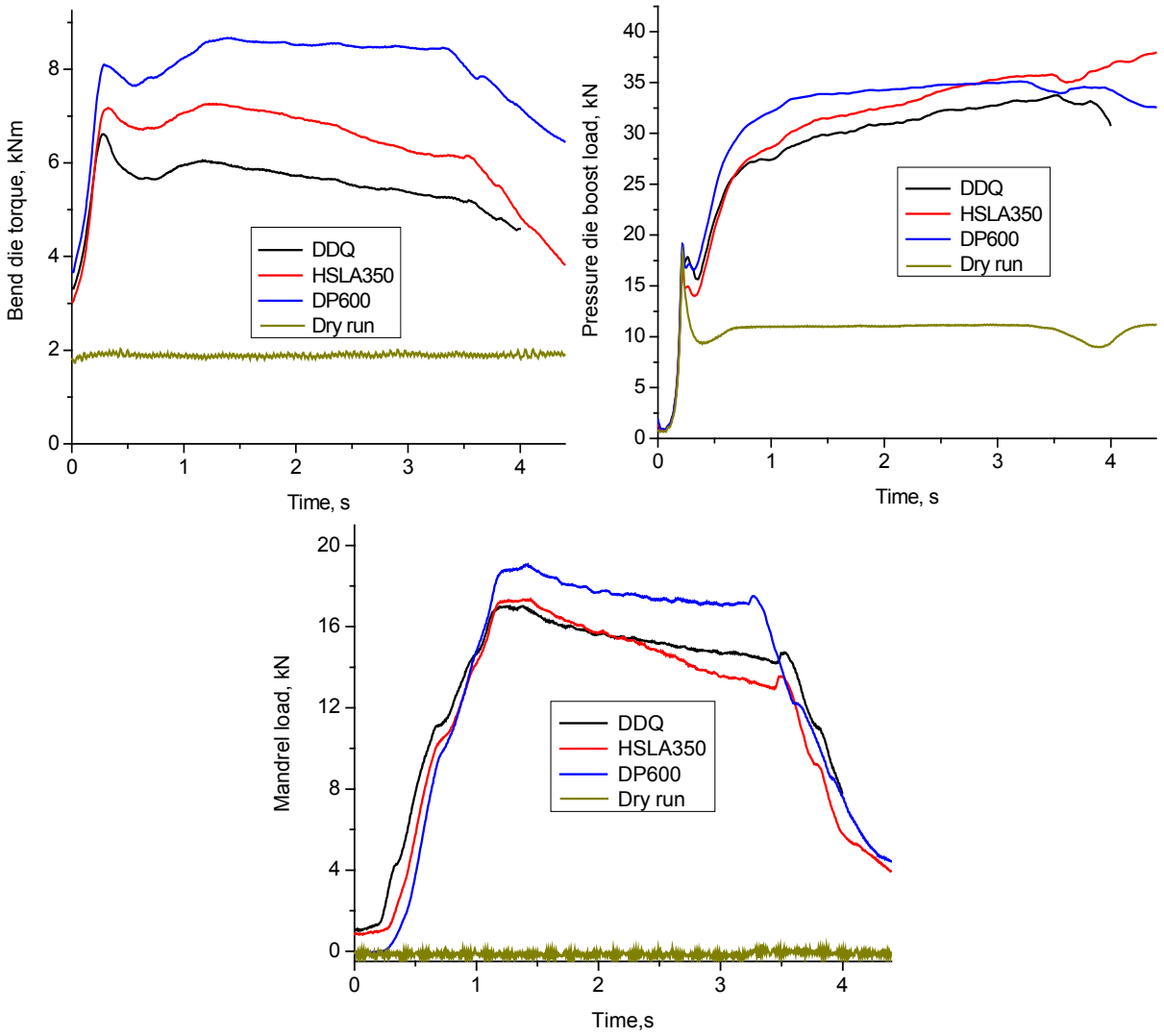

Figure 58: Average tube bending process parameters for DDQ, HSLA350 and DP600

5.1.2 Strain and thickness distribution

Strain and thickness distributions measured from three pre-bent DDQ tubes along the outside, inside and around the circumference of the bend are presented in Figure 59. The accuracy of the strain

measurements depended on the quality of the grids. On the inside of the bend, the grids usually had poor quality due to the severe frictional interaction between the wiper and tube. According to Dyment [41], the error associated with the strain measurements was about $\pm 3\%$ strain. Thickness measurements did not depend on the clarity of circle grids and had less variation. The repeatability of the strain and thickness measurements presented for the DDQ bends was representative of the results for the other alloys. Therefore, average strain and thickness distributions, based on measurements of three tubes per alloy, were calculated for the comparison purpose.

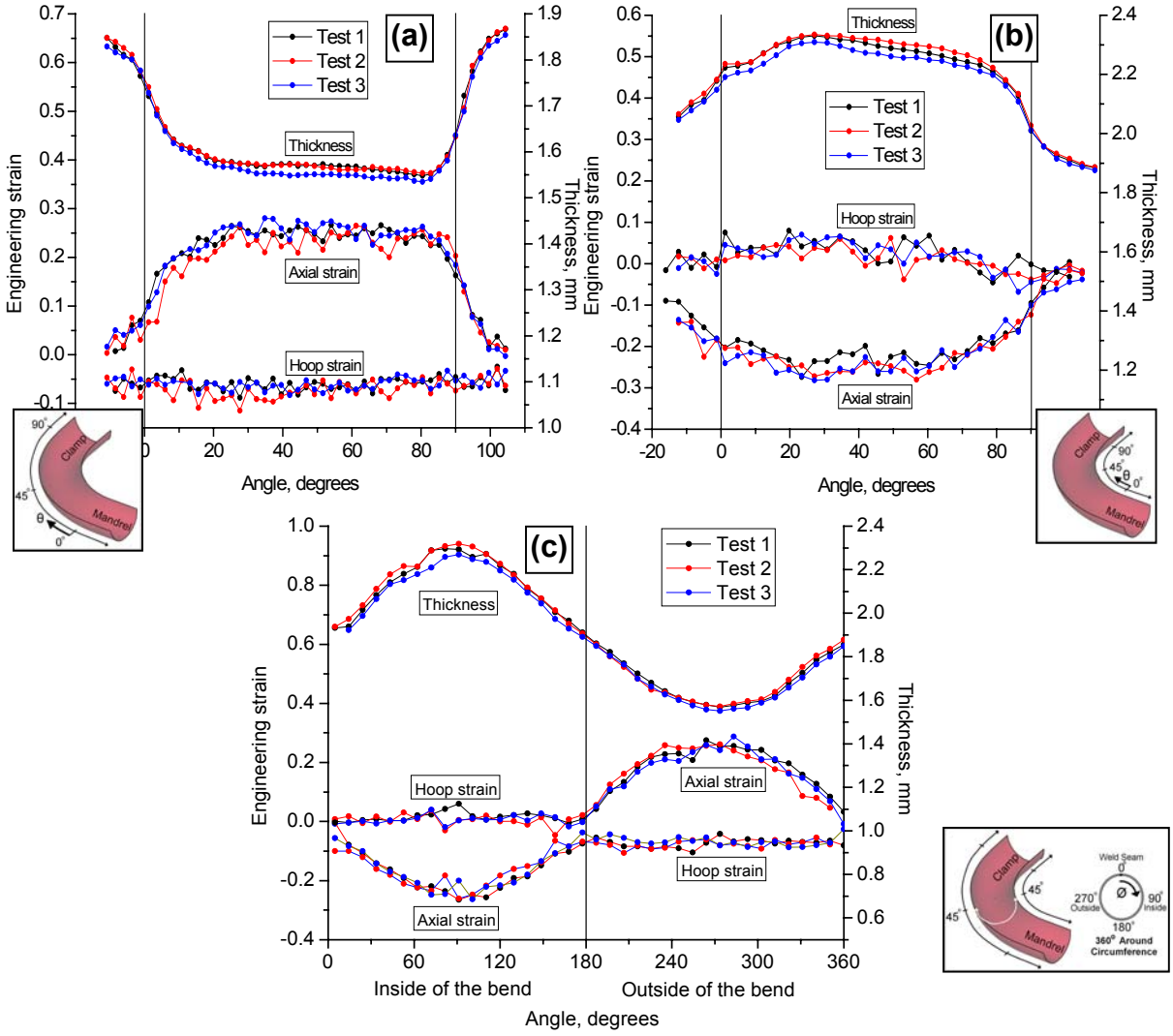

Figure 59: Strain and thickness distributions for pre-bent DDQ tubes (a) along the outside of the bend, (b) along the inside of the bend; (c) around the circumference of the bend

The average thickness and strain distributions for the tree alloys after bending are presented in Figure 60 and Figure 61. The trends in the strain distributions were the same for the three alloys and the

variation between alloys fell within a range of measurement error. The thickness distributions around the circumference of the tube were essentially the same.

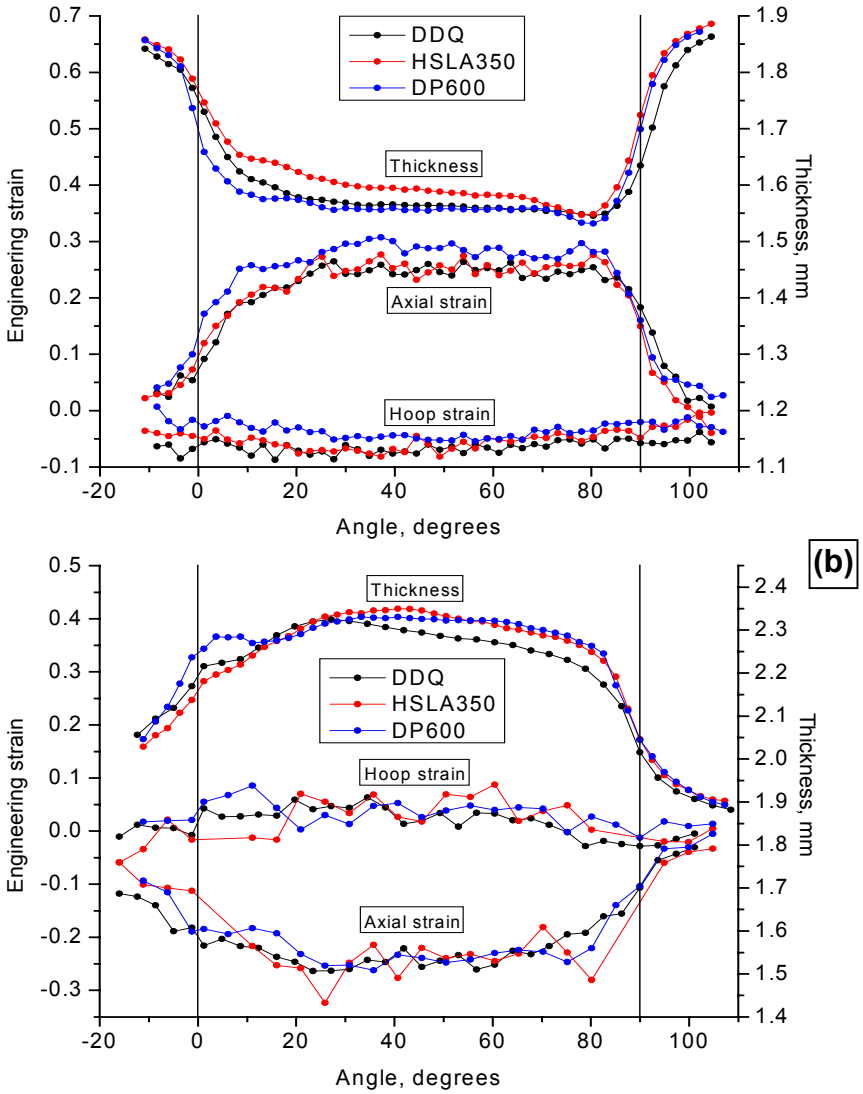

Figure 60: Strain and thickness distributions for pre-bent DDQ, HSLA350 and DP600 tubes (a) along the outside of the bend, (b) along the inside of the bend

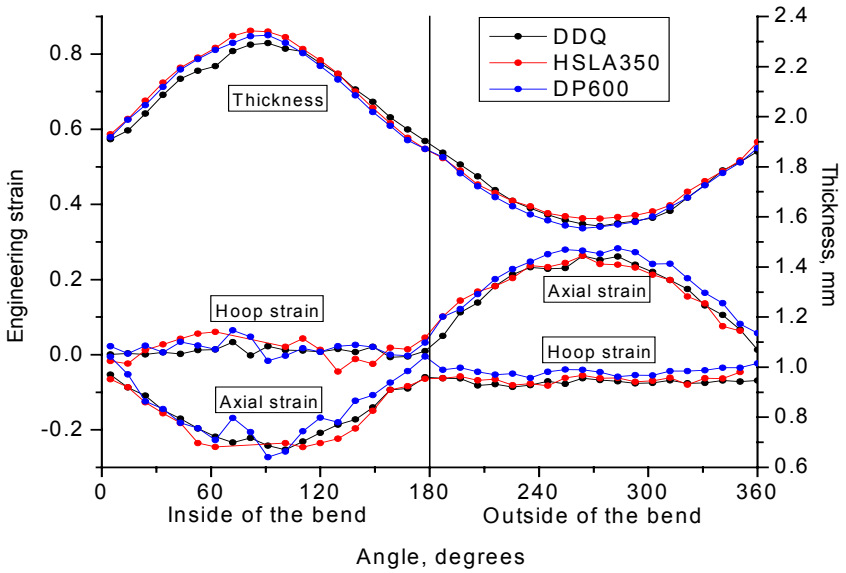

Figure 61: Strain and thickness distributions around the circumference of the bend for pre-bent DDQ, HSLA350 and DP600 tubes

5.2 Straight tube hydroforming experimental results

Several straight tube hydroforming setup tests were conducted for each alloy to evaluate the maximum level of end-feed load a tube could sustain before wrinkling. After that, tube hydroforming tests were carried out with end-feed levels of zero, 0.25YS, 050YS, 1.00YS, 1.50YS and 2.00YS, up to the maximum level of end-feed load before wrinkling. The following results were obtained:

- The DDQ tubes did not burst at any end-feed load level including zero end-feed. All tubes were pressurized up to 151.7 MPa (22 000 psi) without failure. After the tests, all tubes, regardless of the end-feed level, were almost fully formed to the hydroforming die with 6 mm corner radius. At an end-feed level of 2.00YS the tubes started to wrinkle. Although the DDQ straight tube hydroforming results didn't provide any burst data, they showed an effect of increased end-feed on tube expansion versus pressure, as well as the thickness and strain distributions at maximum internal pressure.

- The HSLA350 tubes burst at zero, 0.25YS and 0.50YS levels of end-feed. At 1.00YS end-feed level, the tubes were pressurized up to the maximum pressure of 151.7 MPa without wrinkling or bursting. At 1.50YS end-feed level, mild wrinkles were produced, while 2.0YS resulted in severe wrinkling of the tube.

- The DP600 tubes burst at levels of end-feed below 1.0YS. At 1.0YS the tubes didn't burst or wrinkle, while at 1.50YS end-feed level, the tubes started to wrinkle.

A summary of the straight tube hydroforming burst test results is tabulated in Table 11.

Table 11: Summary of straight tube hydroforming burst tests

	axial stress/ YS	EF load, kN	num of tests	failure mode	burst(max) pressure, MPa			end-feed displacement, mm			corner radius, mm			corner-fill expansion, %		
					averge	min	max	averge	min	max	averge	min	max	averge	min	max
DDQ	0.00	0	1	-	151.7	-	-	-	-	-	6.7	-	-	82.9	-	-
	0.25	30.2	-	-	-	-	-	-	-	-	-	-	-	-	-	-
	0.50	60.4	1	-	151.7	-	-	26.3	-	-	6.7	-	-	82.8	-	-
	1.00	120.8	1	-	151.7	-	-	39.9	-	-	6.8	-	-	82.5	-	-
	1.50	181.2	1	-	151.7	-	-	59.1	-	-	7.0	-	-	82.2	-	-
	2.00	241.6	1	wrinkled	-	-	-	-	-	-	-	-	-	-	-	-
HSLA350	0.00	0	3	burst	57.0	54.6	59.2	-	-	-	13.9	11.8	15.5	64.4	60.2	69.9
	0.25	45.7	3	burst	65.1	64.5	65.9	17.5	17.1	17.7	9.5	8.5	10.4	75.5	73.1	78.1
	0.50	91.3	3	burst	86.3	75.5	96.7	25.8	25.0	26.6	8.2	7.4	8.8	79.0	77.4	81.1
	1.00	182.6	1	-	151.7	-	-	42.3	-	-	7.9	-	-	79.7	-	-
	1.50	273.9	1	wrinkled	-	-	-	-	-	-	-	-	-	-	-	-
	2.00	365.2	1	wrinkled	-	-	-	-	-	-	-	-	-	-	-	-
DP600	0.00	0	3	burst	62.9	60.9	63.9	-	-	-	14.8	14.7	14.9	62.0	61.9	62.2
	0.25	54.3	3	burst	73.8	72.7	75.3	14.5	14.3	14.6	12.3	11.3	13.4	68.4	65.7	71.1
	0.50	108.6	3	burst	124.3	103.7	137.9	26.0	25.0	27.2	8.6	7.6	9.6	78.0	75.4	80.6
	1.00	217.2	1	-	151.7	-	-	38.0	-	-	10.0	-	-	73.8	-	-
	1.50	325.8	1	wrinkled	-	-	-	-	-	-	-	-	-	-	-	-
	2.00	-	-	-	-	-	-	-	-	-	-	-	-	-	-	-

The straight hydroformed DDQ, HSLA350 and DP600 tubes are presented in Figure 62, showing the increase of the amount of the material fed into the die cavity at higher levels of end-feed. Wrinkles can be observed in the HSLA350 tubes at 1.50YS and 2.0YS end-feed levels and in the DP600 tube corresponding to 1.50YS end-feed level.

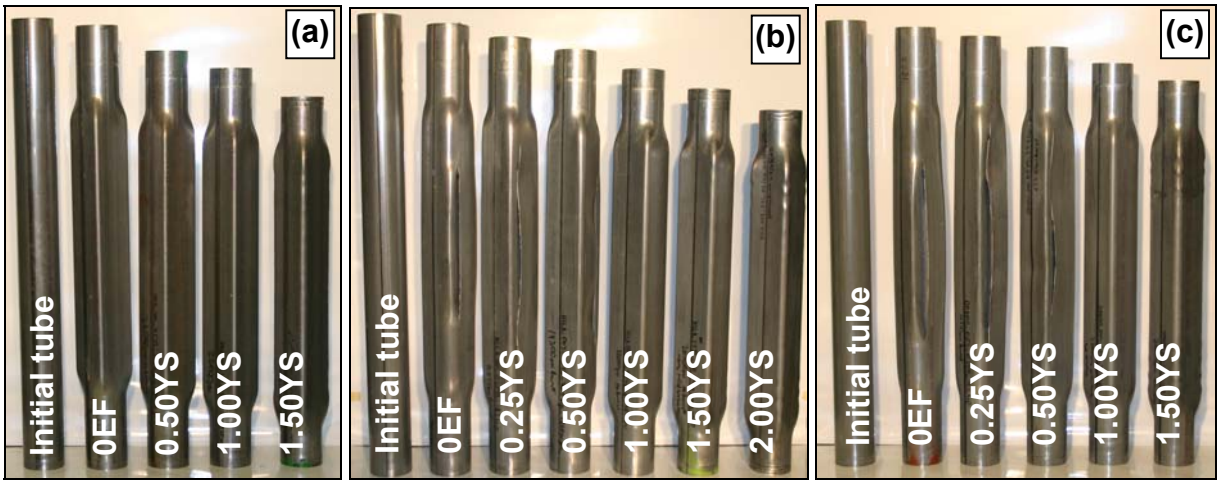

Figure 62: Straight hydroformed (a) DDQ, (b) HSLA350 and (c) DP600 tubes

5.2.1 Tube burst pressure

The measured average, maximum and minimum tube burst pressures are summarized for HSLA350 and DP600 in Figure 63, based on three tests for each case. In other cases, the tubes didn't burst prior to reaching the maximum pressure of 151.7 MPa. The DP600 tube hydroformed with 0.50YS level of end-feed could withstand double the internal pressure compared to the zero end-feed case. At the higher end-feed level of 1.0YS, both materials did not burst or wrinkle up to the maximum internal pressure of 151.7 MPa. The scatter in the burst pressure for both materials increased with an increase of end-feed level and burst pressure.

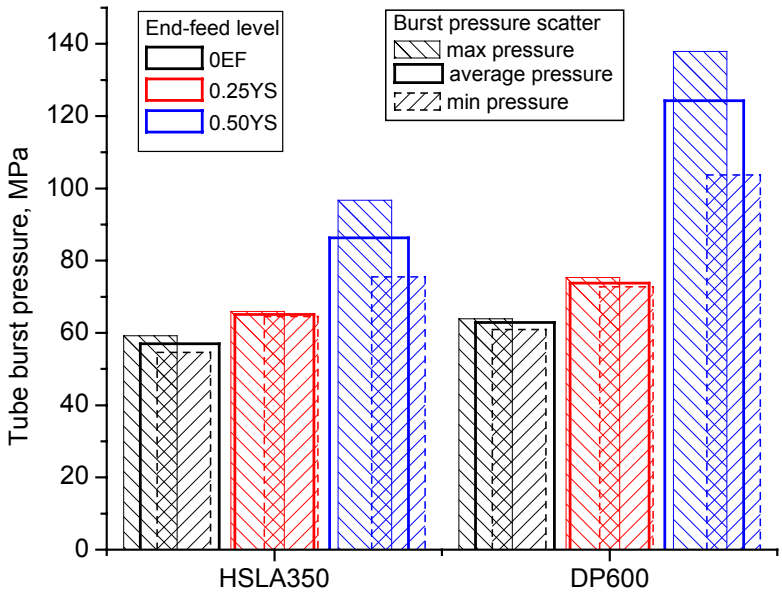

Figure 63: Tube burst pressure for hydroforming of straight HSLA350 and DP600 tubes

5.2.2 End-feed displacement

The displacement of the tube ends in the straight tube hydroforming experiments is summarized in Figure 64. The bar chart utilizes the convention employed for all subsequent bar charts: for the cases in which the tube did not burst, each quantity is presented by one value attained at maximum pressure; for the cases when the tube did burst, three values are presented: the average, maximum and minimum values obtained at burst pressure in the three experiments. Such bar graphs show the scatter associated with the results at burst and distinguish the cases when tubes burst from those when they did not.

For a given end-feed load level the amount of tube end displacement attained in the DDQ, HSLA350 and DP600 straight tube hydroforming was similar, although the tube burst pressure varied and the magnitude of end-feed load was different for each alloy. For example, at 0.50YS level of end-feed, the

maximum displacement of the DDQ tube end was 26.3 mm, compared to 25.8 mm for HSLA350 and 26.0 mm for DP600. At an end-feed level of 1.00YS none of the DDQ, HSLA350 or DP600 tubes burst at the maximum pressure of 151.7 MPa, which resulted in about 40 mm of tube end displacement at each end.

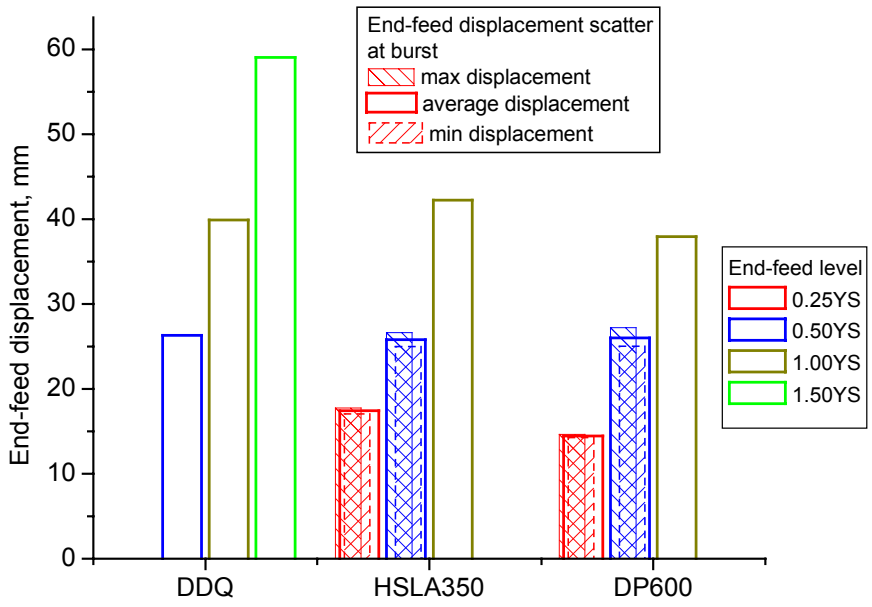

Figure 64: Tube end displacement at burst for hydroforming of straight DDQ, HSLA350 and DP600 tubes

Average curves of tube end displacement versus internal pressure are presented in Figure 65. Within each end-feed level the curves for different alloys converged to the same value at high internal pressure. The scatter in the maximum values for each curve can be estimated based on the scatter at burst, presented in previous graph.

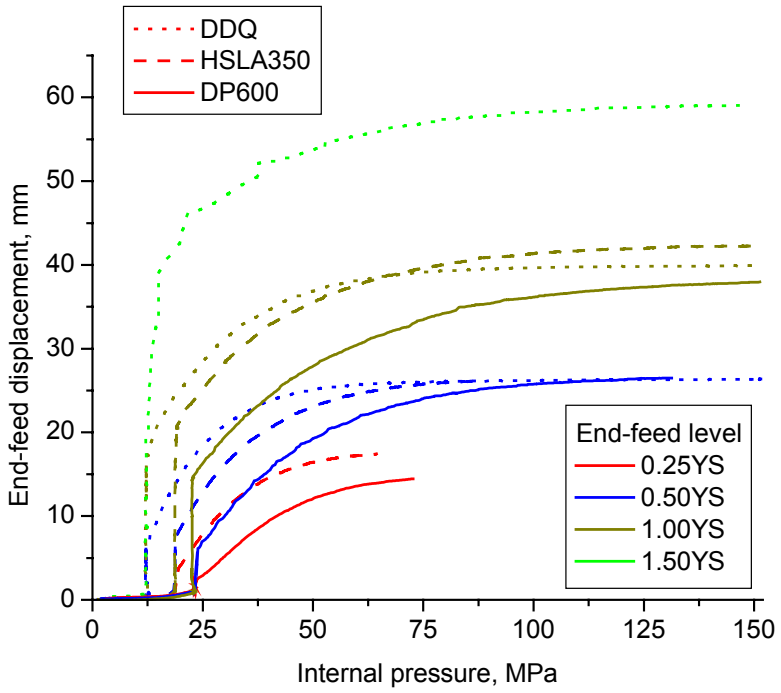

Figure 65: Tube end displacement versus internal pressure for hydroforming of straight DDQ, HSLA350 and DP600 tubes

5.2.3 Corner-fill expansion

Tube corner radii, measured manually after the straight tube hydroforming burst tests, are summarized in Figure 66 for all three alloys. The straight hydroforming die had a corner radius of 6 mm, which limited the minimum corner radius that a tube could attain.

The DDQ tubes demonstrated a slight increase in the tube corner radius from 6.7 mm at zero end-feed to 7.0 mm at 1.5YS end-feed level. The measured corner radii correspond to the maximum internal pressure of 151.7 MPa because none of the tubes burst during the experiments. The mild increase in corner radius with the increase of end-feed level might be caused by the higher tube wall thickness at those end-feed levels. Thicker tube walls had higher springback and required higher internal pressure to form small corner radii.

The decrease in corner radius at burst for the HSLA350 and DP600 tubes with an increase of end-feed force was significant. At the same time, the corner radius of the HSLA350 tubes hydroformed at 1.00YS level of end-feed decreased by only 0.3 mm compared to 0.50YS end-feed, however, the maximum internal pressure almost doubled from 84 MPa at 0.50YS to 151.7 MPa at 1.00YS. For DP600 straight tube hydroforming at 1.00YS end-feed, the change in corner radius was even larger. In both cases a negative aspect of excessive end-feed was evident. If too much material was fed into the die cavity, a much higher internal pressure was required to form a small corner radius.

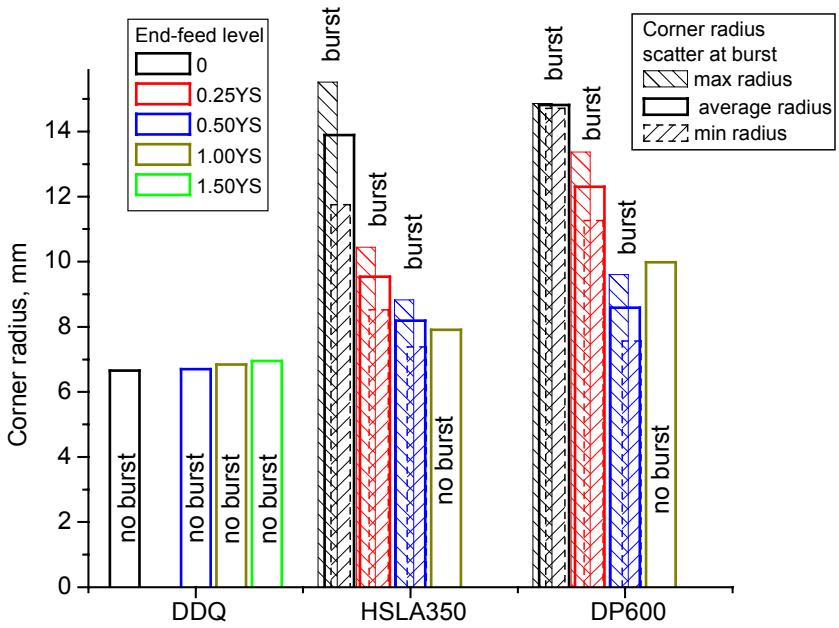

Figure 66: Tube corner radii at burst for hydroforming of straight DDQ, HSLA350 and DP600 tubes

Corner-fill expansion (%CFE) data, based on the tube corner radii presented above is summarized in Figure 67. A corner-fill expansion of 0% corresponds to the initial circular tube. A corner-fill expansion of 100% would correspond to a tube fully formed to a perfectly square cross-section with zero corner radius. The straight tube hydroforming die had a corner radius of 6 mm; therefore the maximum %CFE that could be attained with the current die was 84.6%.

The amount of corner-fill expansion obtained in the straight tube hydroforming experiments was already high at zero end-feed. The HSLA350 and DP600 tubes pressurized with zero end-feed had %CFE of 62% and 64% at burst, respectively. Higher end-feed increased the %CFE to 80% and 78% for HSLA350 and DP600, respectively, which was significant, but required much higher internal pressures and a more elaborate control system.

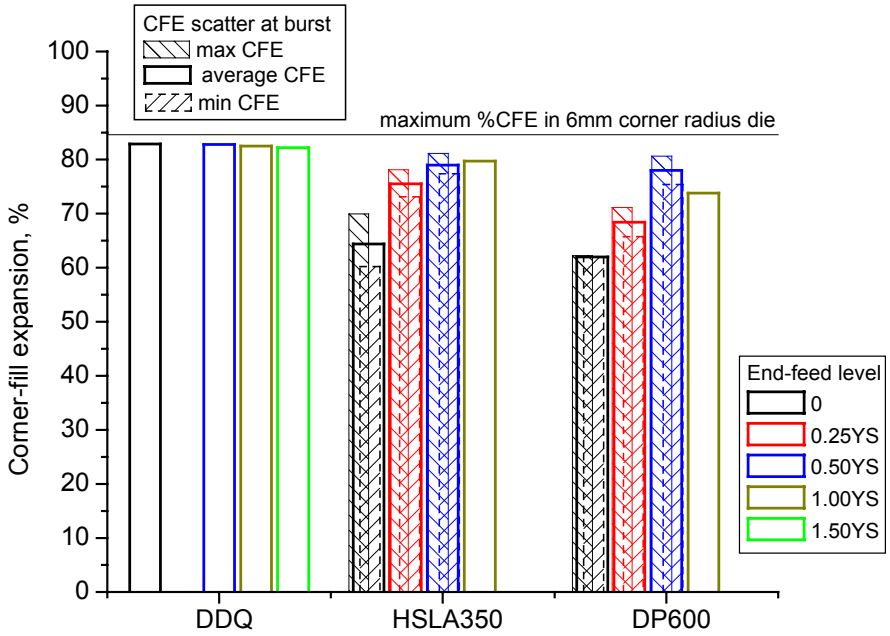

Figure 67: Tube corner-fill expansion at burst for hydroforming of straight DDQ, HSLA350 and DP600 tubes

The corner expansion versus internal pressure for each alloy is shown in Figure 68. The maximum expansion in the die with square cross-section and zero corner radius would be 16.1 mm, while the actual maximum expansion for the 6 mm corner radius die was 13.7 mm. For each alloy the curves tended to converge at high internal pressure regardless of the end-feed level. The negative effect of excessive end-feed was demonstrated by corner expansion of the DDQ tubes; when at high internal pressure, the same amount of tube expansion was attained earlier by the tubes hydroformed with lower end-feed than by those with higher end-feed.

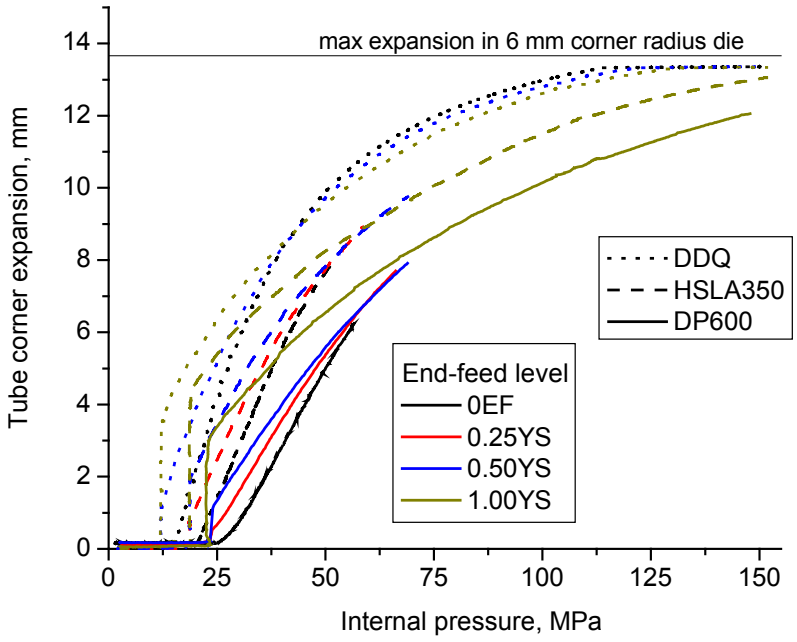

Figure 68: Tube corner expansion versus internal pressure for hydroforming of straight DDQ, HSLA350 and DP600 tubes

5.2.4 Strain and thickness distributions

A series of interrupted tests was conducted on the gridded DDQ, HSLA350 and DP600 tubes hydroformed with end-feed load levels of zero, 0.25YS, 0.50YS and 1.0YS. During the interrupted tests, each tube was pressurized to 90% of average tube burst pressure. A number of tubes did not burst and were removed intact from the press after the maximum pressure of 151.7 MPa was applied. The HSLA350 and DP600 tubes hydroformed with 0.50YS level of end-feed exhibited a larger scatter in the internal pressure at burst and were pressurized to a lower pressure.

Strain and thickness distributions were measured around the circumference in the middle cross-section of the tube. Every grid around the circumference of the tube was measured. The total number of grids measured per tube was 77. A position of the grid was defined by an angle with respect to the weld seam according to the diagram, shown in Figure 69. Two tubes per end-feed case were tested and measured for each alloy.

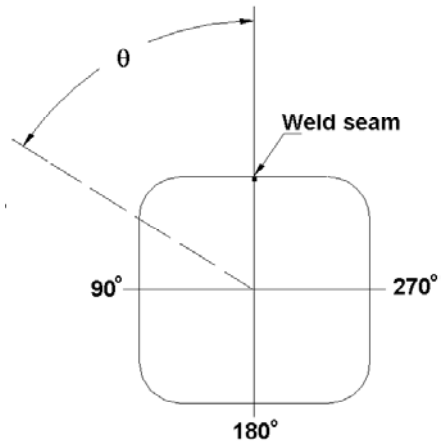

Figure 69: Straight tube hydroforming grid position diagram

Strain and thickness distributions measured on two HSLA350 tubes pressurized up to 80% of the average tube burst pressure with 0.50YS level of end-feed are presented in Figure 70. The error associated with the strain measurements was about $\pm 3\%$ strain according to Dyment [41] due to the dependence of strain measurements on the quality of the grids. Thickness measurements didn't depend on the clarity of circle grids and had less variation. The repeatability of the strain and thickness measurements seen in Figure 70 was typical for the other straight tube hydroforming cases. Therefore, average curves based on the measurements of two tubes per case are shown for subsequent data, assuming similar scatter.

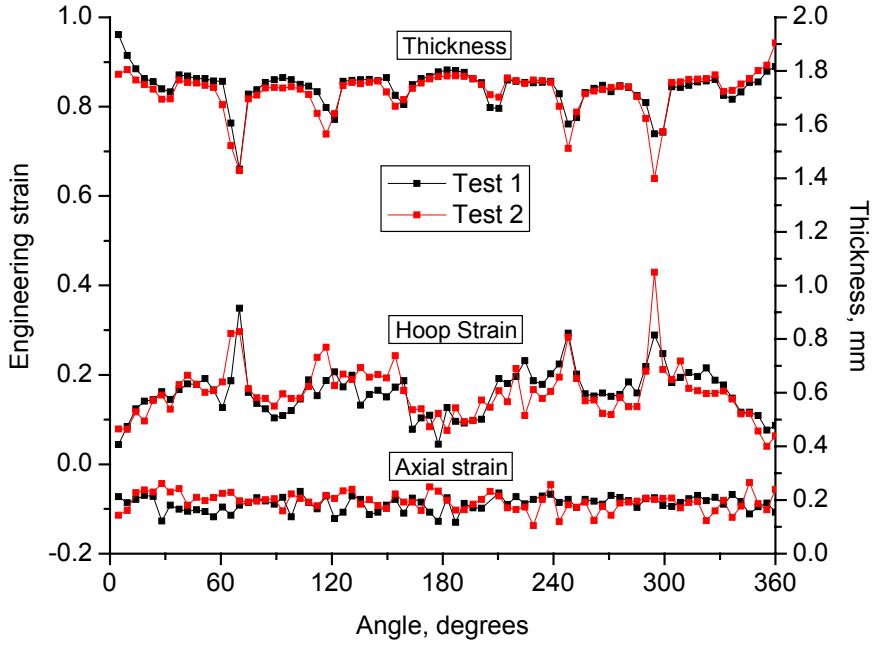

Figure 70: Thickness and strain distributions for hydroforming of straight HSLA350 tube at 0.50YS level of end-feed, internal pressure 80% to burst

Strain and thickness distributions for hydroforming of straight DDQ tubes at zero, 0.50YS and 1.00YS levels of end-feed are shown in Figure 71. The tubes were pressurized to the maximum pressure of 151.7 MPa without burst. All tubes were almost fully formed to conform to the 6 mm corner radius hydroforming die, producing similar hoop strain distributions regardless of the end-feed level. Higher compressive axial strains due to the higher end-feed loads resulted in a corresponding increase in tube wall thickness.

At zero end-feed, the DDQ tubes displayed symmetric incipient necking at two locations at 61^0 and 294^0 with respect to the weld seam. At higher levels of end-feed, the overall tube thickness increased and the incipient necking location at 294^0 disappeared, while the 61^0 location remained even at the end-feed level of 1.00YS. Incipient necking never led to the tube burst, because the tube was almost fully formed and further expansion was constrained.

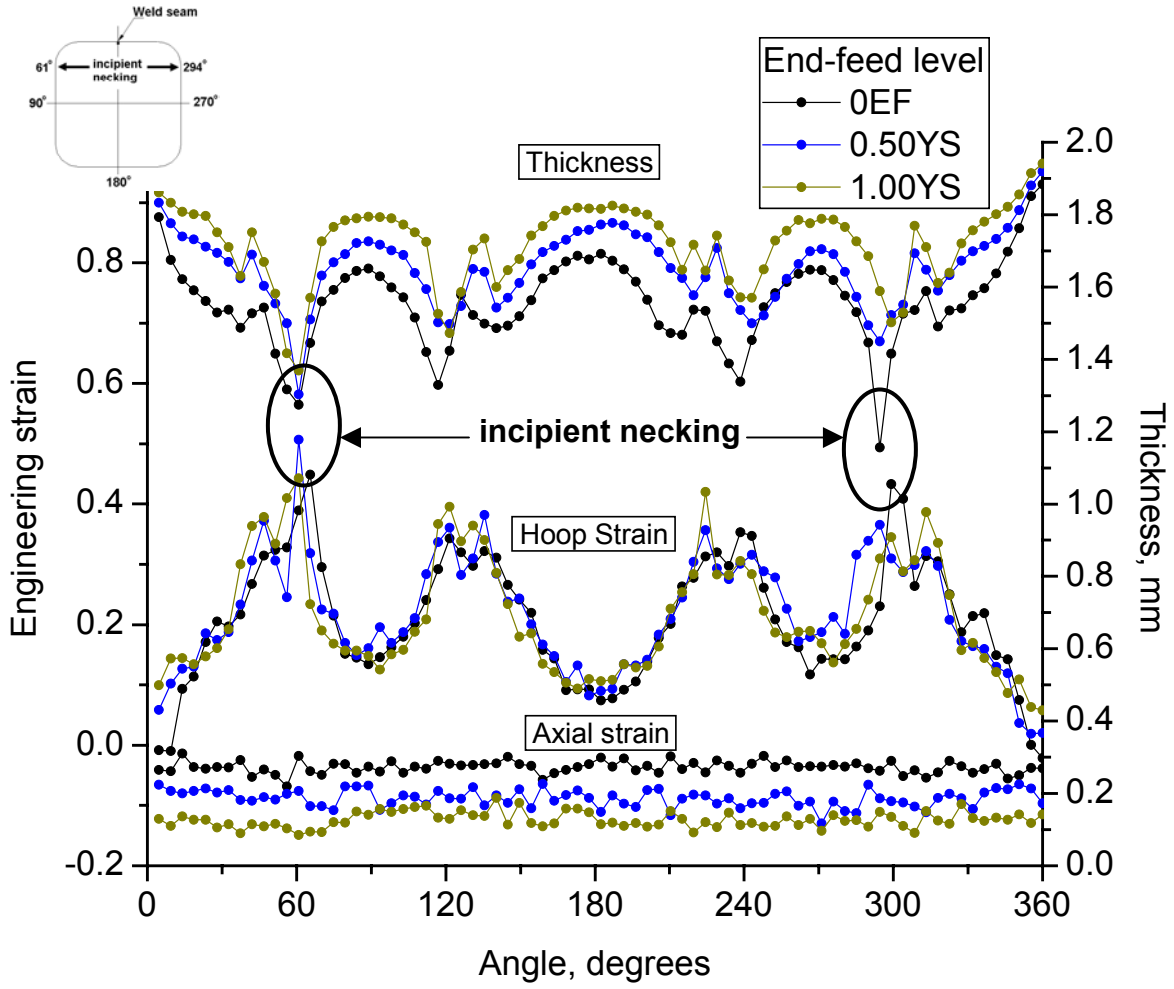

Figure 71: Strain and thickness distributions for hydroformed straight DDQ tubes. (Tubes did not fail)

Strain and thickness distributions for hydroforming of straight HSLA350 tube at zero, 0.25YS, 0.50YS and 1.00YS levels of end-feed are presented in Figure 72. The measurements corresponding to zero and 0.25YS end-feed levels were conducted on the tubes pressurized to 90% of the burst pressure. Those at an end-feed level of 0.50YS were pressurized to 80% of the burst pressure, while at an end-feed level of 1.00YS the tubes did not burst and were pressurized to maximum pressure of 151.7 MPa and then unloaded and removed from the press.

The level of hoop strain increased with an increase in tube expansion at higher levels of end-feed; the maximum hoop strain was attained at 1.00YS end-feed level. Symmetric incipient necking locations were observed at the end-feed level of 1.00YS at 61^0, 116^0, 243^0 and 299^0 around the circumference of the tube with respect to the weld seam. At the end-feed levels below 0.50YS, the strain and thickness distributions didn't indicate any incipient necking locations in the interrupted tubes.

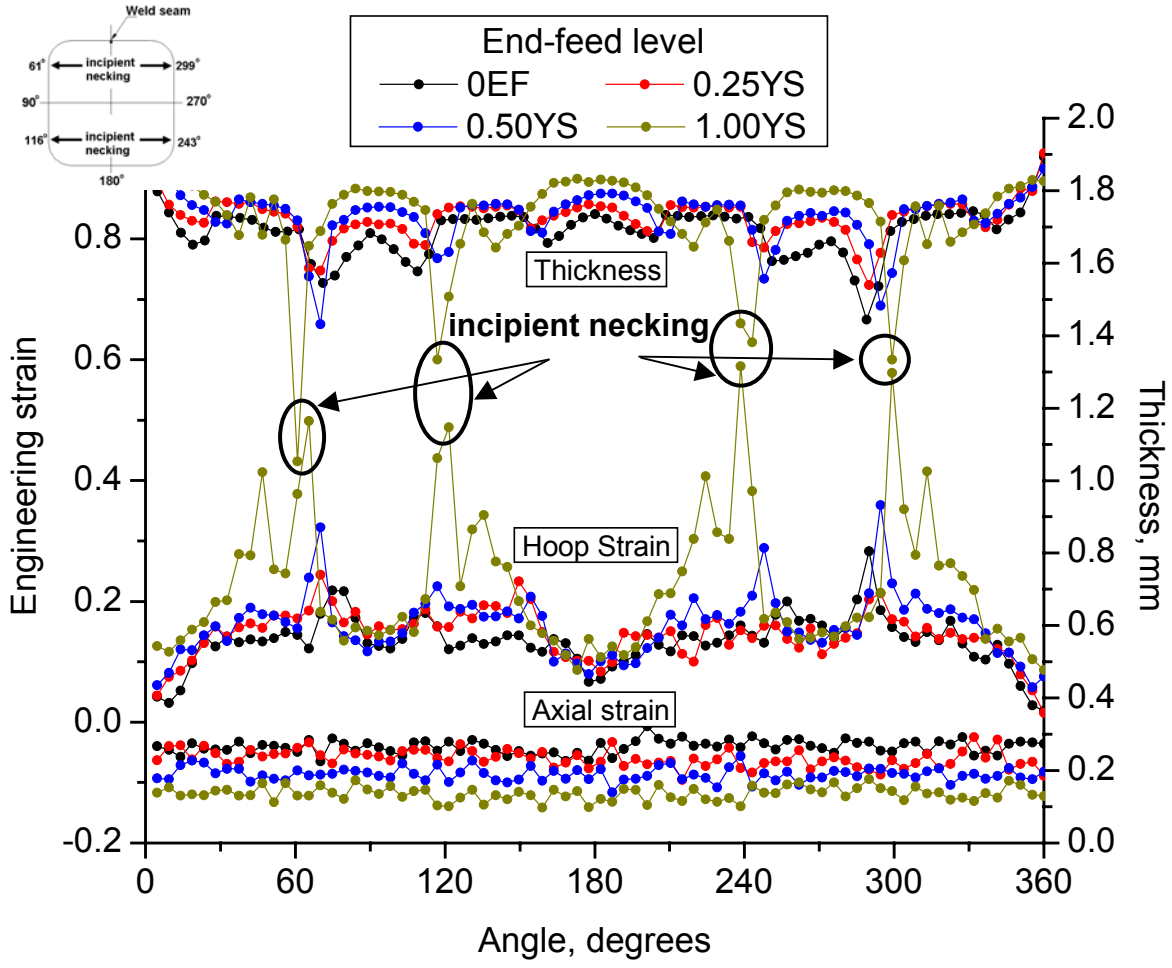

Figure 72: Strain and thickness distributions for hydroformed straight HSLA350 tubes

Strain and thickness distributions for hydroforming of straight DP600 tubes at zero, 0.25YS, 0.50YS and 1.00YS levels of end-feed are shown in Figure 73. The measurements corresponding to zero and 0.25YS end-feed levels were conducted on the tubes pressurized to 90% of the burst pressure, while the 0.50YS end-feed tubes were pressurized to 60% of the burst pressure. Burst did not occur for the tubes tested at 1.00YS end-feed level.

The tube expansion and level of hoop strain increased with end-feed. Higher end-feed produced an increase in axial compressive strain and thickness of the tube. Incipient necking at 1.00YS end-feed was observed at the 116^0, 238^0 and 294^0 locations around the circumference of the tube.

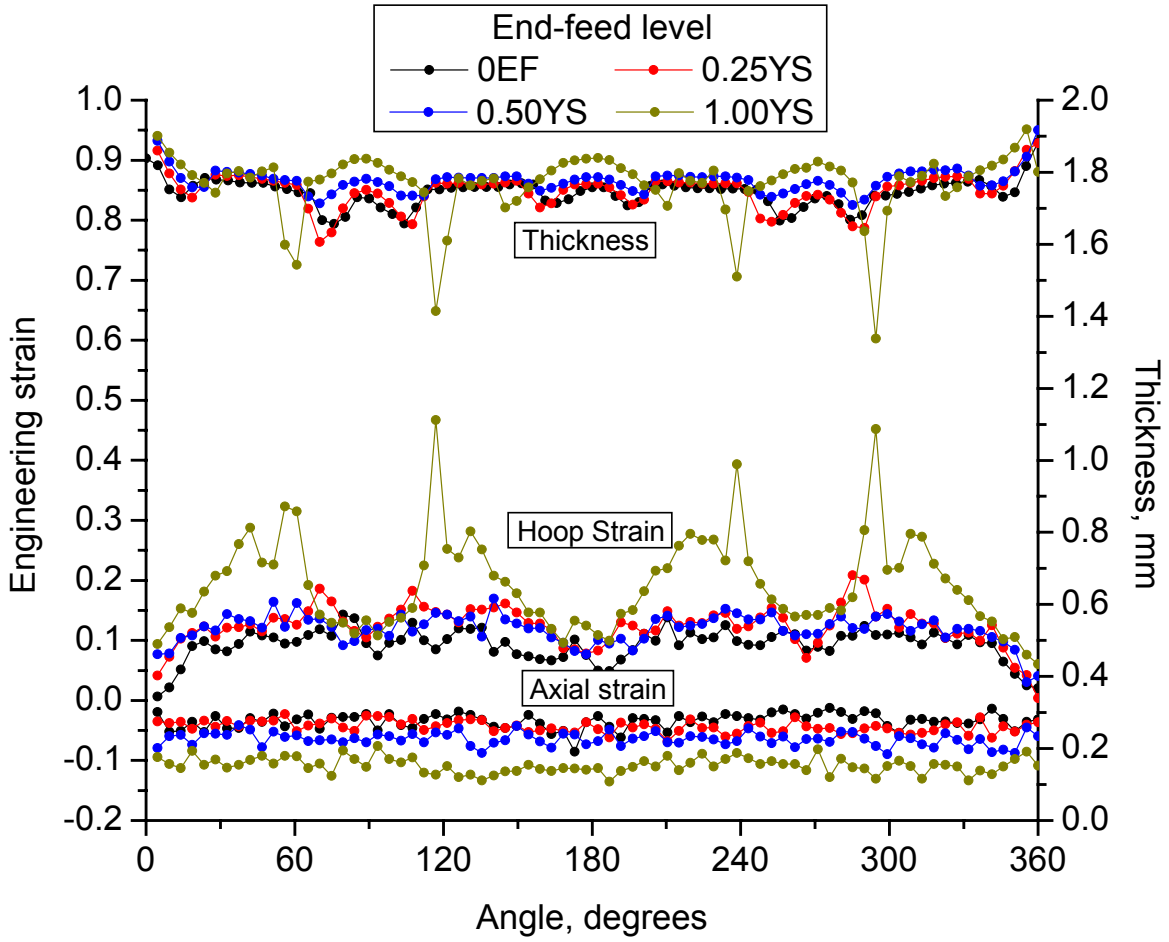

Figure 73: Strain and thickness distributions for hydroformed straight DP600 tubes

The strain and thickness distributions of the straight DDQ, HSLA350 and DP600 tubes hydroformed at 1.0YS level of end-feed and pressurized up to the maximum pressure of 151.7 MPa are shown in Figure 74. The distributions for the three alloys appear to be almost identical regardless of the strength of the material. Some minor differences occur in the regions around the incipient necking locations.

The results show that a high level of end-feed produces the same strain distribution in the less formable DP600 tube as in much more formable DDQ tube without failure.

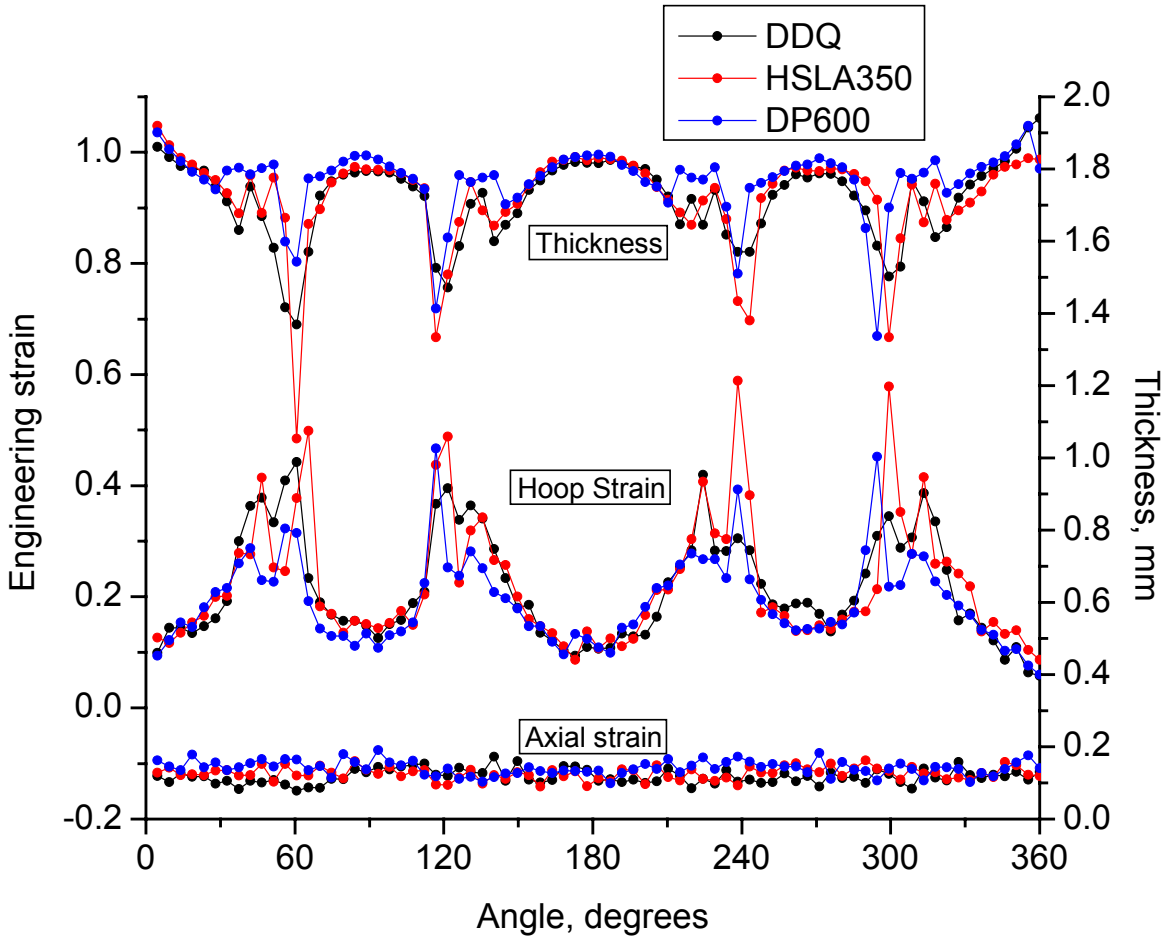

Figure 74: Summary of strain and thickness distributions for hydroforming of straight DDQ, HSLA350 and DP600 tubes at 1.00YS level of end-feed, internal pressure 151.7 MPa

Average values of strain and thickness around the circumference of DDQ, HSLA350 and DP600 tubes hydroformed at different levels of end-feed are summarized in Figure 75 and Table 12. The DDQ tubes, which all fully formed in the hydroforming die, had the same average hoop strain at different levels of end-feed. Therefore, for DDQ an increase in compressive axial strain at higher levels of end-feed was compensated by an increase in tube wall thickness.

The HSLA350 and DP600 tubes had higher expansion at higher levels of end-feed and, therefore, greater average hoop strain. Increased end-feed for HSLA350 and DP600 also produced higher compressive axial strain, which compensated for the increased hoop strain. The average thickness of the HSLA350 and DP600 tubes remained unchanged with the increase of end-feed level.

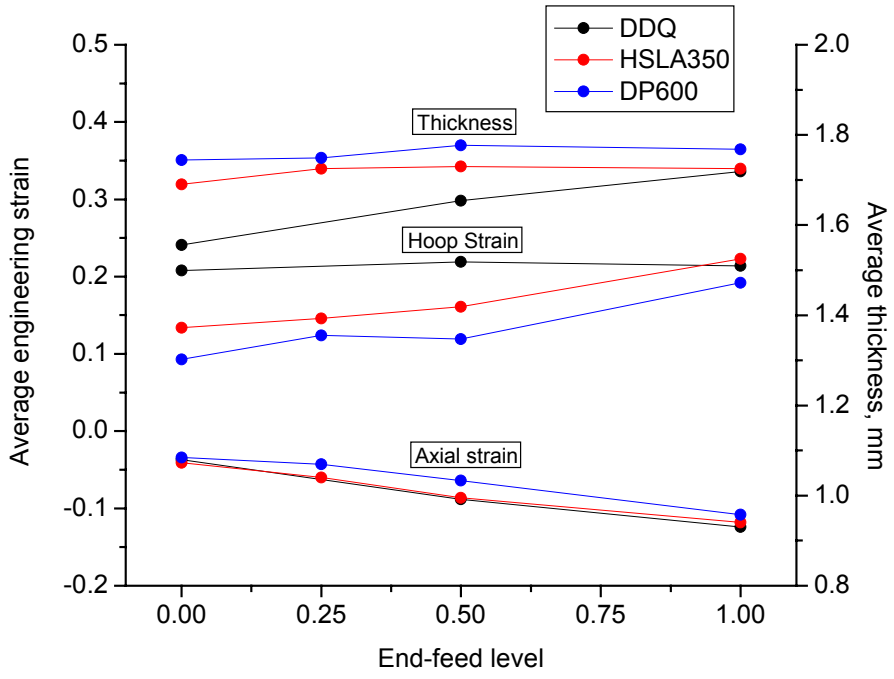

Figure 75: Summary of average strains and thickness for hydroforming of straight DDQ, HSLA350 and DP600 tubes

Table 12: Summary of average strains and thickness for hydroforming of straight DDQ, HSLA350 and DP600 tubes

	EF level	Internal pressure,MPa	fraction of internal pressure to burst pressure	Average		
				major eng strain	minor eng strain	thickness,mm
DDQ	0.00	151.7	1.0	0.208	-0.037	1.556
	0.50	151.7	1.0	0.219	-0.088	1.654
	1.00	151.7	1.0	0.214	-0.124	1.719
HSLA350	0.00	51.7	0.9	0.134	-0.041	1.690
	0.25	58.6	0.9	0.146	-0.060	1.725
	0.50	69.0*	0.8*	0.161	-0.086	1.730
	1.00	151.7	1.0	0.223	-0.118	1.725
DP600	0.00	56.5	0.9	0.093	-0.034	1.744
	0.25	66.2	0.9	0.124	-0.043	1.749
	0.50	69.0*	0.6*	0.119	-0.064	1.777
	1.00	151.7	1.0	0.192	-0.108	1.768

5.2.5 Onset of necking in straight tube hydroforming experiments

The XSFLC method utilized for failure prediction in the FE simulations of the straight and pre-bent tube hydroforming essentially provides predictions of the onset of necking. Therefore the measured internal pressure at the onset of necking was estimated for each case.

The strain and thickness distributions measured from the straight HSLA350 and DP600 tubes hydroformed at zero and 0.25YS levels of end-feed did not indicate any incipient necking locations at 90% of tube burst pressure. This meant that the neck initiated at an internal pressure higher than 90% of burst pressure. Therefore, for the purpose of current research, the internal pressure at the onset of necking was assumed to coincide with the average tube burst pressure for these cases. For the straight HSLA350 and DP600 tubes hydroformed at an end-feed level of 0.50YS, the onset of necking was also assumed to coincide with the moment of burst.

The strain and thickness distributions for the tubes pressurized to maximum pressure of 151.7 MPa without burst indicated incipient necking. Therefore, in order to estimate internal pressure at the onset of necking, additional interrupted tests were conducted on tubes pressurized to 70% of the maximum pressure and lower. These tubes were cut in half, and examined using a tactile method to obtain estimates for the upper and lower limits of internal pressure at the onset of necking. Due to the large number of cases, three internal pressure levels per end-feed case were tested for each alloy. As a result, lower and upper estimates of internal pressure at the onset of necking were determined. A summary of the estimated internal pressure at the onset of necking is presented in Table 13.

Table 13: Estimated internal pressure at the onset of necking in straight tube hydroforming

EF level	Estimated internal pressure at necking initiation, MPa								
	DDQ			HSLA350			DP600		
	Estimated from burst test	Limits		Estimated from burst test	Limits		Estimated from burst test	Limits	
		Lower	Upper		Lower	Upper		Lower	Upper
0.00	-	79.3	115.8	57.0	n/a	n/a	62.9	n/a	n/a
0.25	-	-	-	65.1	n/a	n/a	73.8	n/a	n/a
0.50	-	-	151.7	86.3	n/a	n/a	124.3	n/a	n/a
1.00	-	127.6	151.7	-	82.7	106.2	-	106.2	151.7

5.3 Pre-bent tube hydroforming experimental results

Representative DDQ, HSLA350 and DP600 pre-bent and hydroformed tubes are shown in Figure 76, demonstrating the effect of increased end-feed on the tube expansion and amount of tube material fed into the die cavity. Major wrinkles can be observed on the inside of the bend of the tubes hydroformed at 1.00YS level of end-feed. Therefore subsequent pre-bent tube hydroforming tests were carried out with the end-feed levels of zero, 0.25YS and 0.50YS for the three alloys.

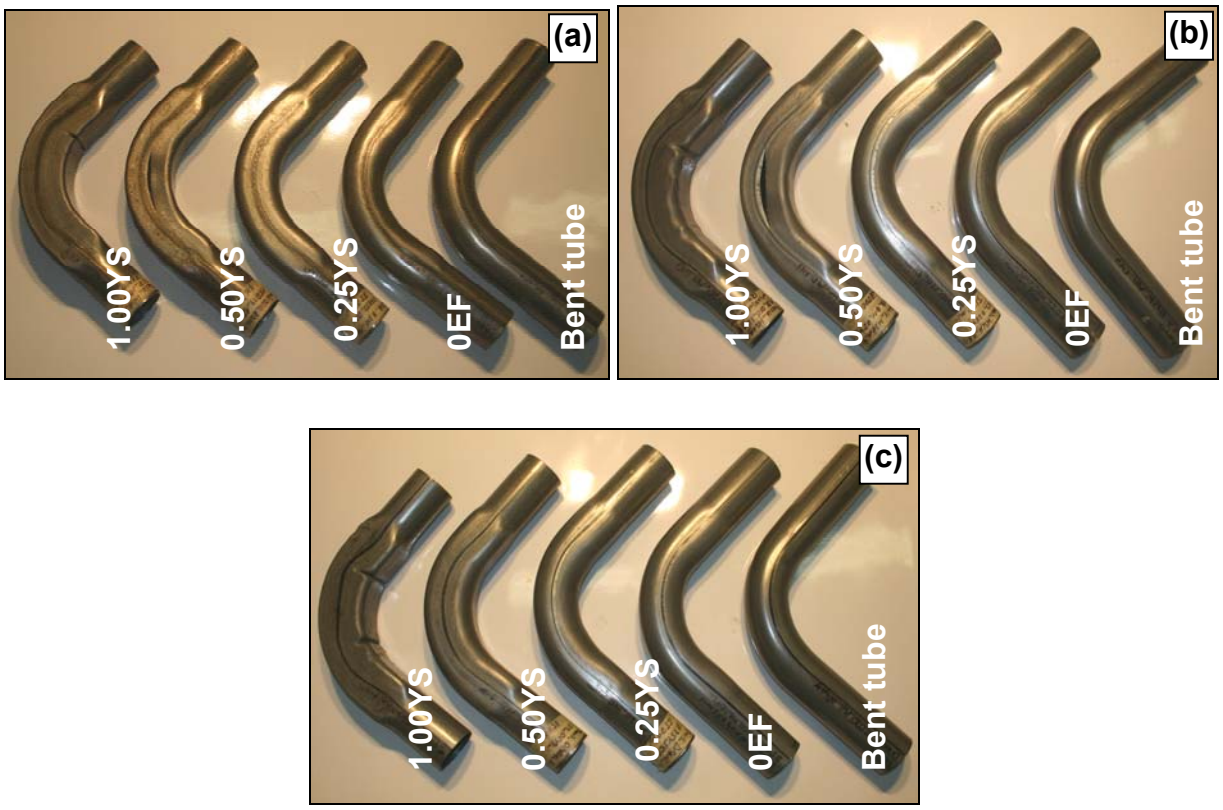

Figure 76: (a) DDQ, (b) HSLA350 and (c) DP600 pre-bent and hydroformed tubes

A summary of pre-bent tube hydroforming burst test results is tabulated in Table 14.

Table 14: Summary of pre-bent tube hydroforming burst tests

	axial stress/YS	EF load, kN	num of tests	failure mode	burst(max) pressure, MPa			end-feed displacement, mm			corner-fill expansion, %					
											outside of the bend			inside of the bend		
					averge	min	max	averge	min	max	averge	min	max	averge	min	max
DDQ	0.00	0	3	burst	26.9	26.7	27.0	5.4	5.4	5.4	26.8	26.5	27.3	-7.8	-9.3	-5.7
	0.25	30.2	3	burst	32.0	31.3	32.5	10.9	10.9	11.3	46.0	44.4	47.6	23.8	22.3	26.0
	0.50	60.4	3	burst	63.1	63.1	63.1	20.4	20.3	20.4	73.3	72.6	74.0	62.7	62.0	63.4
	1.00	120.8	1	wrinkled	-	-	-	-	-	-	-	-	-	-	-	-
HSLA350	0.00	0	3	burst	32.1	32.1	32.1	3.3	3.1	3.5	26.1	24.5	28.6	-20.7	-23.2	-18.0
	0.25	45.7	3	burst	35.6	35.5	35.7	9.4	9.1	10.3	40.3	38.0	43.0	-18.7	-20.6	-15.9
	0.50	91.3	3	burst	55.5	56.3	55.1	17.5	17.3	17.7	60.2	58.1	63.6	42.6	39.7	45.5
	1.00	182.6	1	wrinkled	-	-	-	-	-	-	-	-	-	-	-	-
DP600	0.00	0	3	burst	44.9	44.6	45.0	4.0	3.5	4.8	26.7	26.4	27.0	-9.1	-9.2	-9.0
	0.25	54.3	3	burst	45.4	44.9	46.0	8.5	8.2	9.4	40.0	38.0	41.6	-9.2	-14.2	-1.5
	0.50	108.6	3	burst	66.0	63.6	68.7	16.5	16.4	16.8	61.1	60.3	62.2	34.6	32.0	37.3
	1.00	217.2	1	wrinkled	-	-	-	-	-	-	-	-	-	-	-	-

5.3.1 Burst pressure and burst locations

Average, maximum and minimum burst pressure values for hydroforming of pre-bent DDQ, HSLA350 and DP600 tubes, based on three repeatable tests for each end-feed level, are summarized in Figure 77.

The increase in tube burst pressure from an end-feed level of zero to 0.25YS was small for the DDQ and HSLA350 tubes and insignificant for the DP600 tubes. The increase in tube burst pressure from an end-feed level of 0.25YS to 0.50YS was much more pronounced for all three alloys. The scatter of tube burst pressure in pre-bent tube hydroforming was much smaller than in straight tube hydroforming.

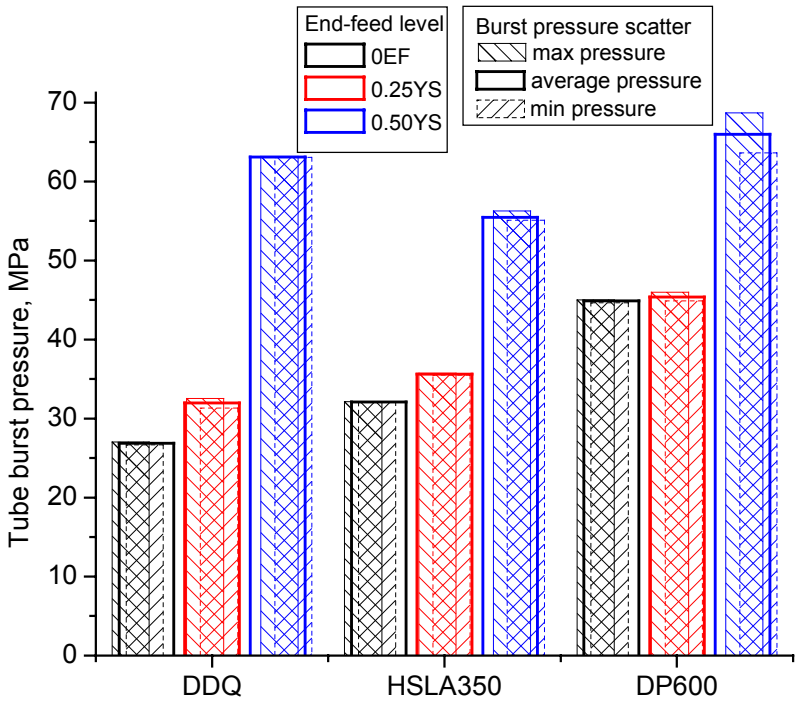

Figure 77: Tube burst pressure for hydroforming of pre-bent DDQ, HSLA350 and DP600 tubes

Typical burst locations in the hydroformed pre-bent DDQ, HSLA350 and DP600 tubes at different levels of end-feed are shown in Figure 78.

DDQ pre-bent tubes hydroformed at zero and 0.25YS levels of end-feed burst at the neutral axis of the bend on the side opposite to the weld seam. At 0.50YS end-feed, the tubes burst at the neutral axis next to the weld seam.

HSLA350 pre-bent tubes hydroformed with zero end-feed burst on the outside of the bend. At 0.25YS end-feed, the tubes burst at the neutral axis on the side opposite to the weld seam. At 0.50YS, the tubes burst along the neutral axis next to the weld seam.

All of the DP600 pre-bent tubes burst at the neutral axis on the side opposite to the weld seam.

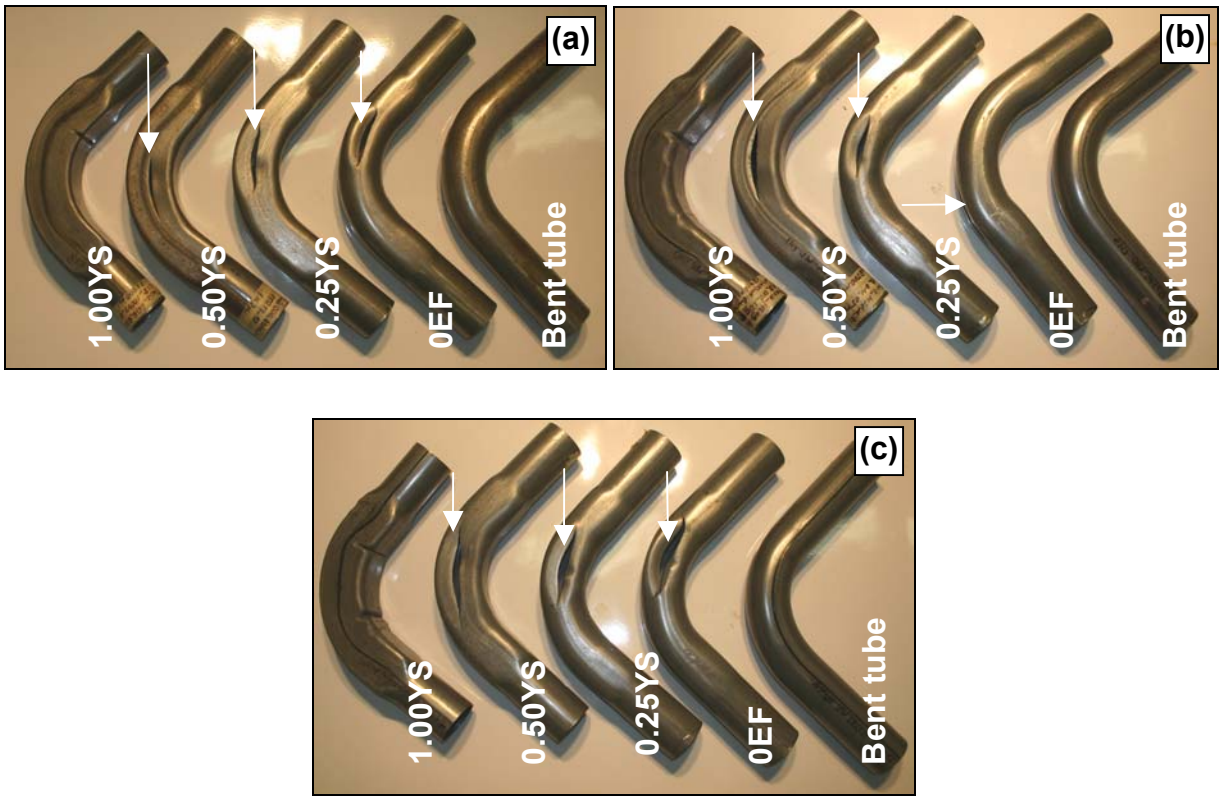

Figure 78: Burst locations in hydroformed pre-bent (a) DDQ, (b) HSLA350 and (c) DP600 tubes

5.3.2 End-feed displacement

The displacement of the tube end at burst during pre-bent tube hydroforming is summarized in Figure 79 for all three alloys. The tube end displacement at zero end-feed was due to contraction of the tube during pressurization. At higher levels of end-feed the amount of the material fed into the die cavity significantly increased. For a given end-feed level, tube end displacement at burst decreased with the increase of strength of the material. For all alloys, the amount of tube end displacement at 0.50YS level of end-feed was about four times higher than the tube end displacement due to self-contraction.

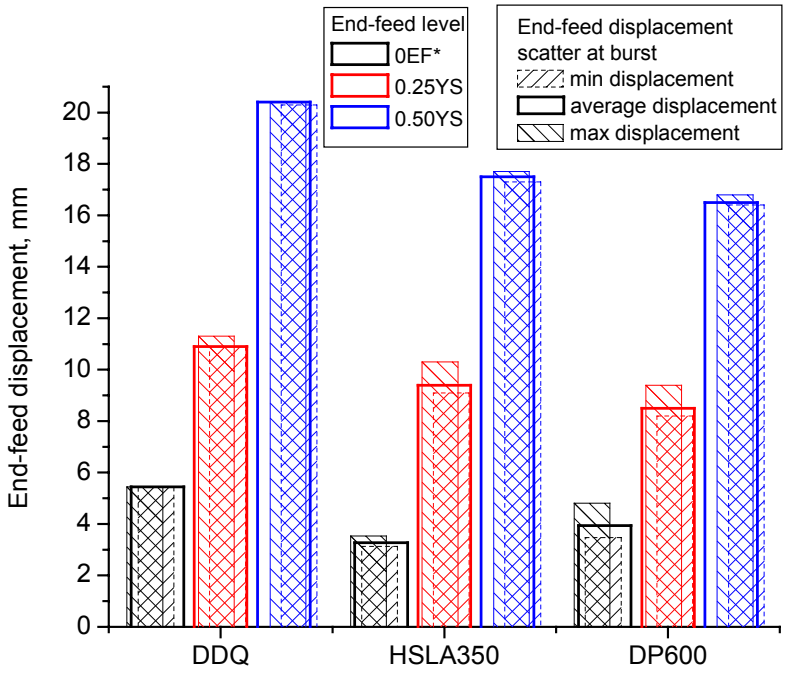

Figure 79: Tube end displacement at burst for hydroformed pre-bent DDQ, HSLA350 and DP600 tubes

The average tube end displacement versus internal pressure curves for the three alloys are presented in Figure 80.

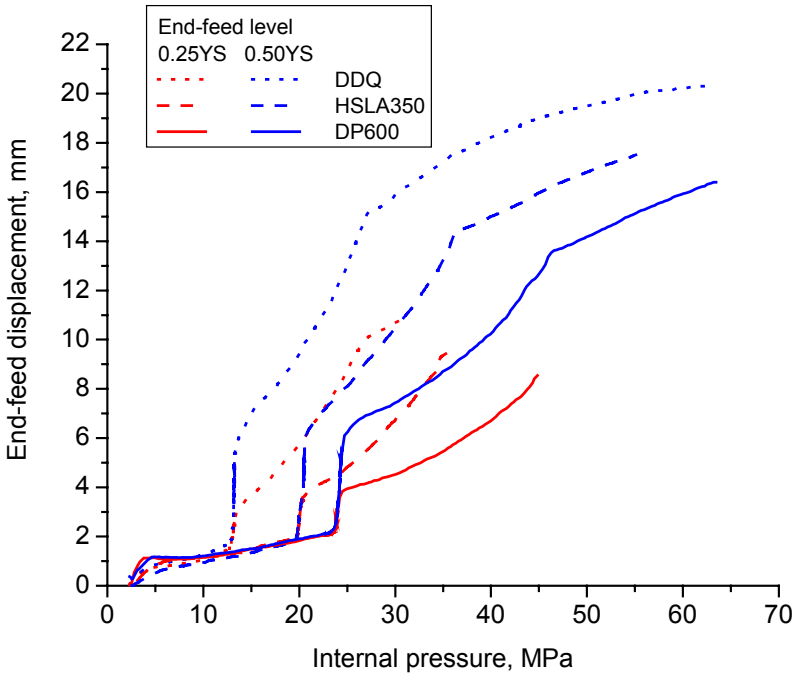

Figure 80: Tube end displacement versus internal pressure for hydroforming of pre-bent DDQ, HSLA350 and DP600 tubes

5.3.3 Corner-fill expansion

Corner-fill expansion (%CFE), measured on the inside and on the outside of the bend away from the failure location after each burst test, is summarized in Figure 81. A corner-fill expansion of 0% corresponded to a tube with circular cross-section of 76.2 mm outer diameter. A corner-fill expansion of 100% would correspond to a tube fully formed to a perfect square cross-section with zero corner radius. The pre-bent tube hydroforming die had a corner radius of 3.175 mm, therefore the maximum %CFE a tube could attain was 91.9%.

The %CFE of the outside of the bend increased significantly with end-feed, from about 26% for all three alloys at zero end-feed, to 73% for DDQ and 60% for HSLA350 and DP600 at 0.50YS level of end-feed. "Negative expansion" of the inside of the bend was observed at low levels of end-feed. Having thinner wall and larger surface area, the outside of the bend started to form earlier than the inside of the bend. The thicker inside of the bend actually moved away from the inside radius of hydroforming die producing an apparent "negative expansion" at the initial stage of pre-bent tube hydroforming. If the tube burst before the inside of the bend started to form, the final expansion of the inside of the bend was negative. This was the case for the DDQ tubes hydroformed with zero end-feed and the HSLA350 and DP600 tubes hydroformed at zero and 0.25YS levels of end-feed.

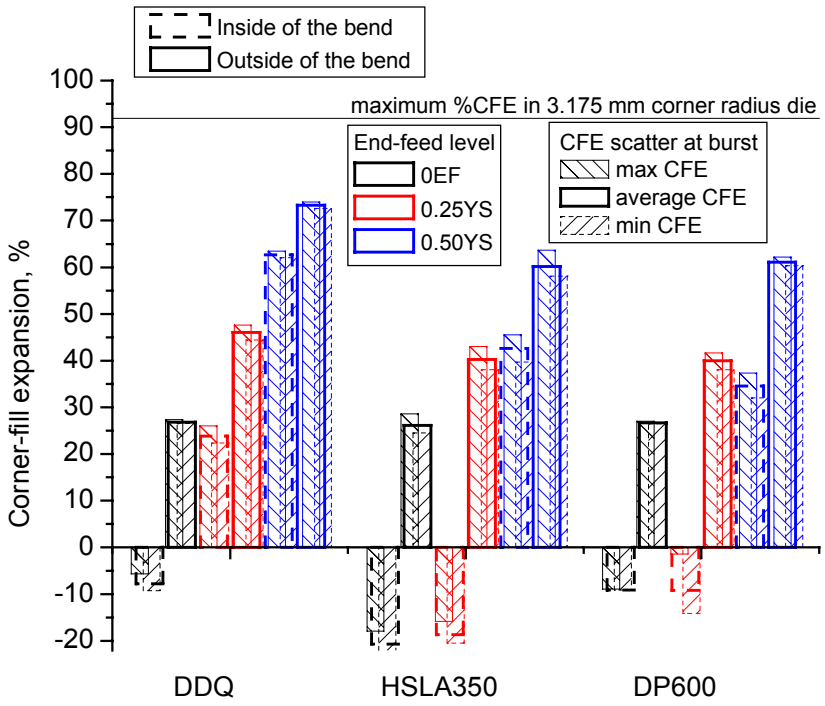

Figure 81: Tube corner-fill expansion of the inside and outside of the bend at burst for hydroformed pre-bent DDQ, HSLA350 and DP600 tubes

To illustrate the effect of negative corner expansion of the inside of the bend, hydroformed tubes, cut in half after the burst tests, are presented in Figure 82. It is evident that the inside of the bend didn't start to form and had a circular cross-section at the moment of burst, for the DDQ tube, hydroformed with zero end-feed, and the HSLA350 and DP600 tubes, hydroformed at zero and 0.25YS levels of end-feed. At the same time, the outside of the bend was already formed. At an end-feed level of 0.50YS, tube burst occurred after the inside of the bend started to form. Figure 81 demonstrated the corresponding increase of %CFE of the inside of the bend at burst from -8%, -21% and -9% at zero end-feed level to 63%, 43% and 35% at 0.50YS level of end-feed for the DDQ, HSLA350 and DP600 tubes, accordingly.

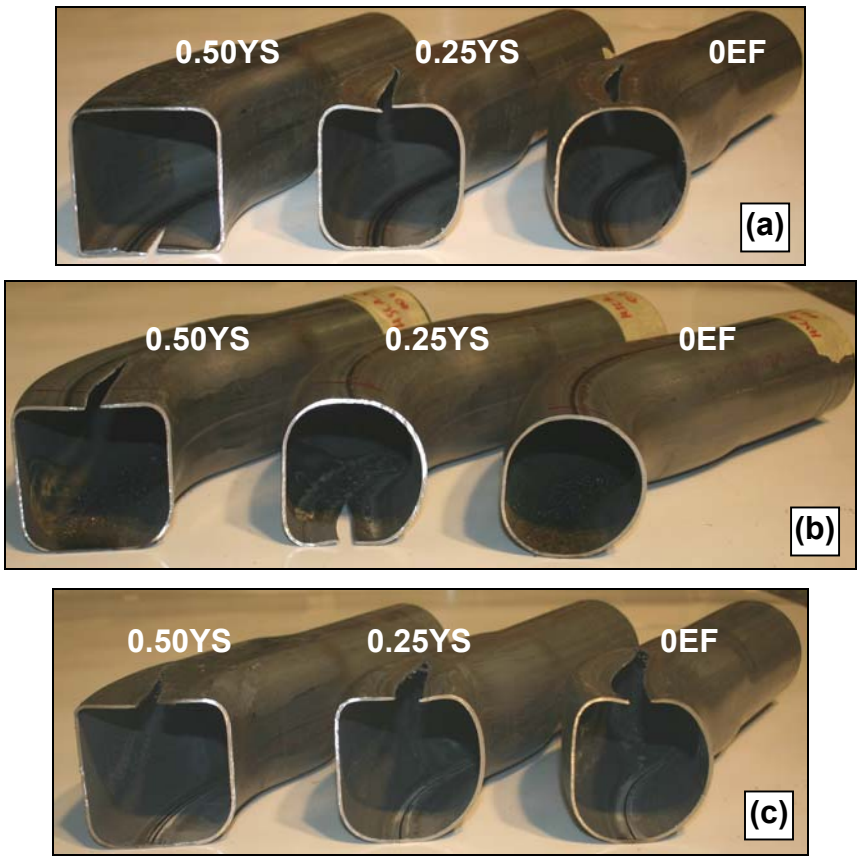

Figure 82: Cross-sections of pre-bent and hydroformed (a) DDQ, (b) HSLA350 and (c) DP600 tubes

5.3.4 Strain and thickness distributions

A series of interrupted pre-bent tube hydroforming tests with zero, 0.25YS and 0.50YS levels of end-feed was conducted on gridded DDQ, HSLA350 and DP600 tubes. Most of the tubes were pressurized to 90% of average tube burst pressure. At 0.50YS level of end-feed additional tubes were pressurized to

70% of average tube burst pressure. Also, some of the DDQ tubes were interrupted at lower pressure as outlined in the following.

Strain and thickness distributions were measured around the circumference in the 45-degree bend angle cross-section of two tubes per case. Every grid around the circumference of the tube was measured. The position of each grid was determined by the angle with respect to the weld seam in the same way as in the straight tube hydroforming experiments.

Measured strain and thickness distributions from DDQ pre-bent tubes hydroformed at zero, 0.25YS and 0.50YS levels of end-feed are presented in Figure 83. Average strain and thickness distributions of non-hydroformed tubes, measured after the tube bending operation, are also included in the figure. Being hot-rolled without any galvanizing treatment, the DDQ tubes developed surface rust after gridding, which led to higher friction and lower burst pressure during hydroforming of gridded tubes, compared to their un-gridded counterparts. For this reason the gridded DDQ tubes hydroformed at 0.25YS and 0.50YS levels of end-feed, were pressurized to only 70% of internal pressure at burst.

The strain and thickness distributions measured from the tubes hydroformed at zero and 0.25YS levels of end-feed were almost identical to the distributions of the non-hydroformed tube. This means that tubes did not undergo significant circumferential expansion before burst. The increase of the outside corner-fill expansion was due to the change of the shape of the cross-section of the tube without any expansion. The "negative corner-fill expansion" of the inside of the bend compensated for the positive corner-fill expansion of the outside of the bend.

At 0.50YS level of end-feed the DDQ tubes burst after the initiation of the circumferential expansion. All changes of strain and thickness distributions occurred on the inside of the bend, while the strains and thickness on the outside of the bend remained the same as in non-hydroformed tube. The strain and thickness distributions indicated the locations of incipient necking, which corresponded to 9^0 and 162^0. Both locations were next to the neutral axis of the bend, one next to the weld seam and the other one on the side opposite to the weld seam. The incipient necking locations in the interrupted tests corresponded to the observed failure locations in the DDQ tubes hydroformed to burst.

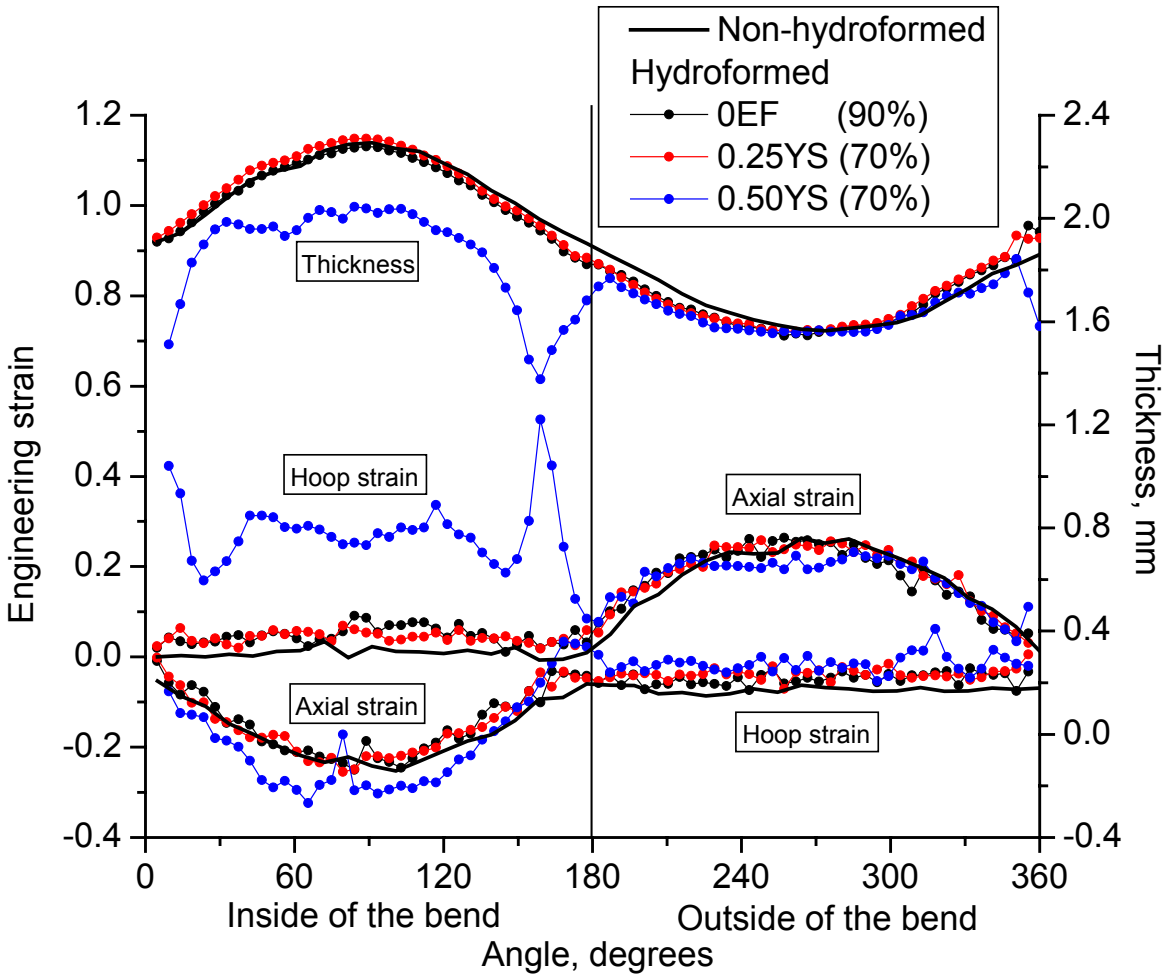

Figure 83: Strain and thickness distributions for hydroformed pre-bent DDQ tubes

The measured strain and thickness distributions from the hydroformed pre-bent HSLA350 tubes at zero, 0.25YS and 0.50YS levels of end-feed are presented in Figure 84. Average strain and thickness distributions from HSLA350 non-hydroformed tubes, measured after tube bending operation, were also included. The strain and thickness distributions of the tubes hydroformed at zero and 0.25YS levels of end-feed were almost identical to the distributions for the non-hydroformed tube with a slight increase of hoop strain at the inside of the bend. At 0.50YS level of end-feed, the strain and thickness distributions on the inside of the bend changed significantly, while on the outside of the bend they remained almost unchanged. The strain and thickness distributions demonstrated three incipient necking locations: on the neutral axis at the weld seam (9^0), on the neutral axis opposite to the weld (164^0) and on the inside of the bend (90^0).

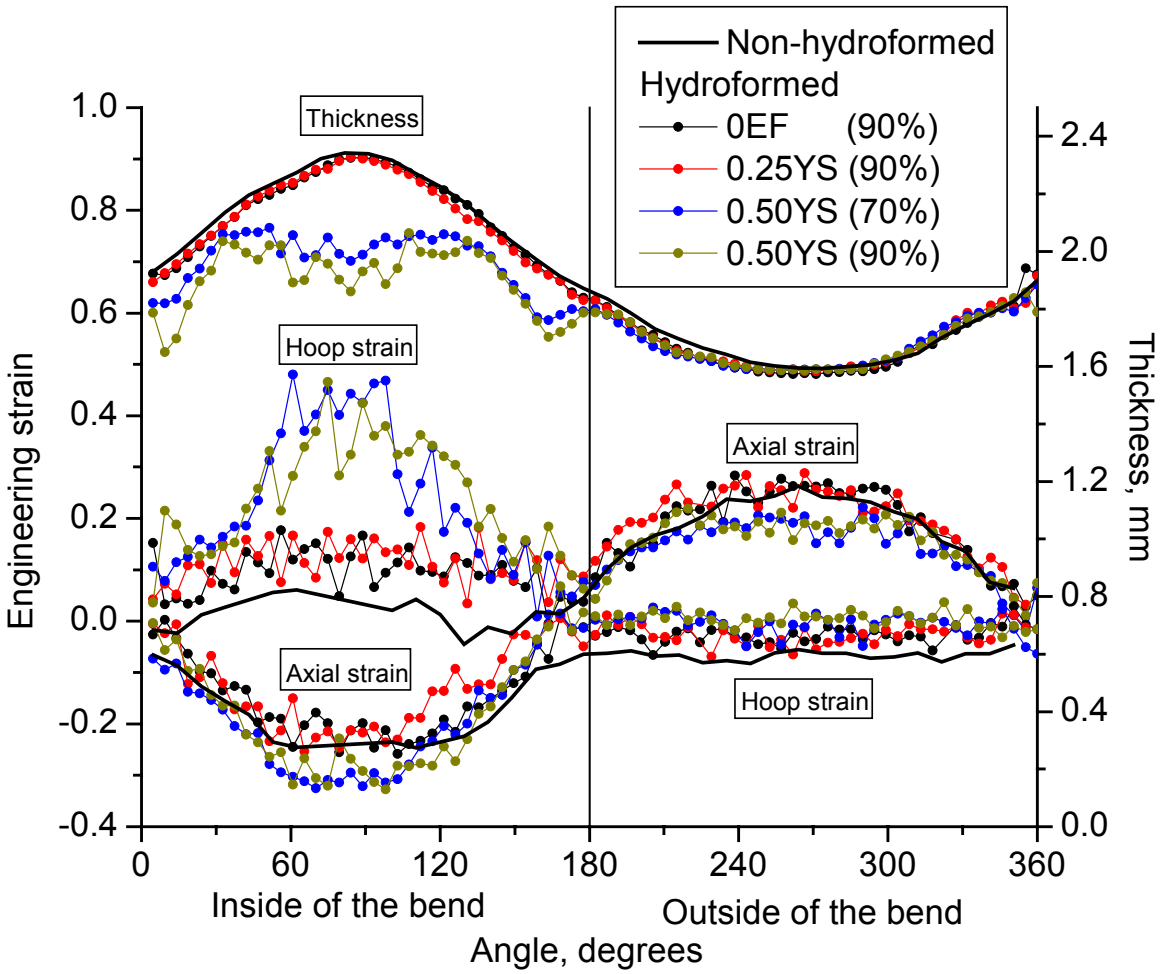

Figure 84: Strain and thickness distributions for hydroformed pre-bent HSLA350 tubes

The strain and thickness distributions from the DP600 pre-bent tubes hydroformed at zero, 0.25YS and 0.50YS levels of end-feed demonstrated the same trends as HSLA350 tubes and are presented in Figure 85.

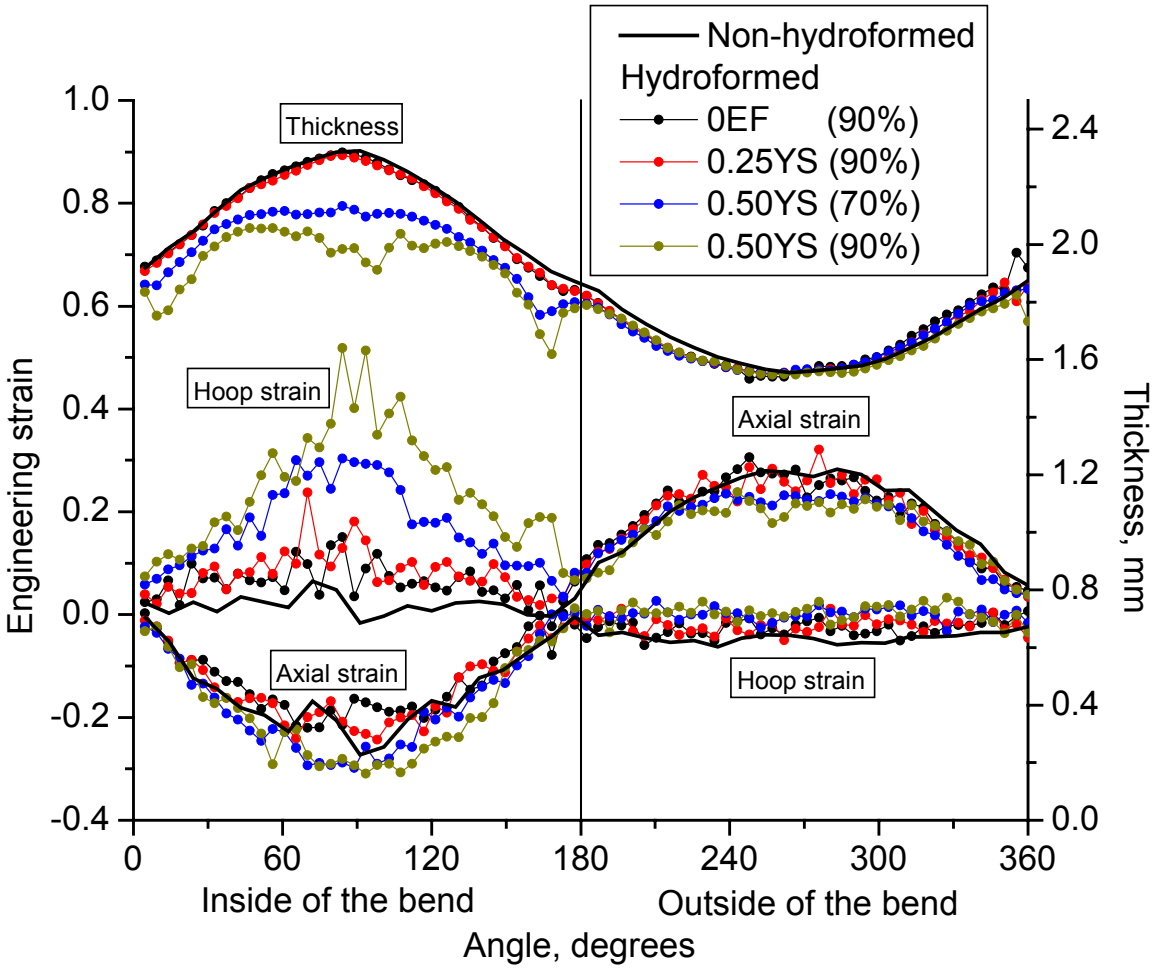

Figure 85: Strain and thickness distributions for hydroformed pre-bent DP600 tube

5.3.5 Onset of necking in pre-bent tube hydroforming experiments

Strain and thickness distributions from the hydroformed pre-bent DDQ, HSLA350 and DP600 tubes at zero and 0.25YS levels of end-feed didn't indicate incipient necking at the internal pressure of 90% of tube burst pressure. Therefore for those cases the onset of necking was assumed to coincide with the moment of burst.

At 0.50YS level of end-feed, the tubes indicated incipient necking, therefore the tubes, pressurized to 90% of the tube burst pressure were cut in half and tactile method was utilized to identify necking. As a result, although the strain and thickness distributions had spikes, necking was not observed. Therefore for DDQ, HSLA350 and DP600 tubes hydroformed at 0.50YS level of end-feed, the onset of necking was also assumed to coincide with the moment of burst.

Chapter 6

Numerical simulation comparison

In the current chapter the results from the simulations of the tube bending and straight and pre-bent tube hydroforming operations are compared with the measured results. In the straight tube hydroforming FE simulations, the effect of friction coefficient on predicted results was also examined in detail. The straight tube hydroforming study confirmed the appropriateness of the input values of COF for the subsequent pre-bent tube hydroforming simulations. Failure predictions made using the XSFLC method for the straight and pre-bent tube hydroforming operations were compared with the experimental results.

6.1 Tube bending

The main purpose of the tube bending FE simulations was to provide accurate input for the subsequent pre-bent tube hydroforming simulations. Detailed FE investigation of the tube bending process itself was already performed by Dyment [41] and Bardelcik [71] and was not in the scope of current work.

A contour plot of effective plastic strain, shown in Figure 86 for an HSLA350 bend, provides good insight into the distribution of strain in the pre-bent tubes. The highest effective plastic stain in the pre-bent tube was attained on the outside and on the inside of the bend, where the highest tension/thinning and compression/thickening occurred, respectively.

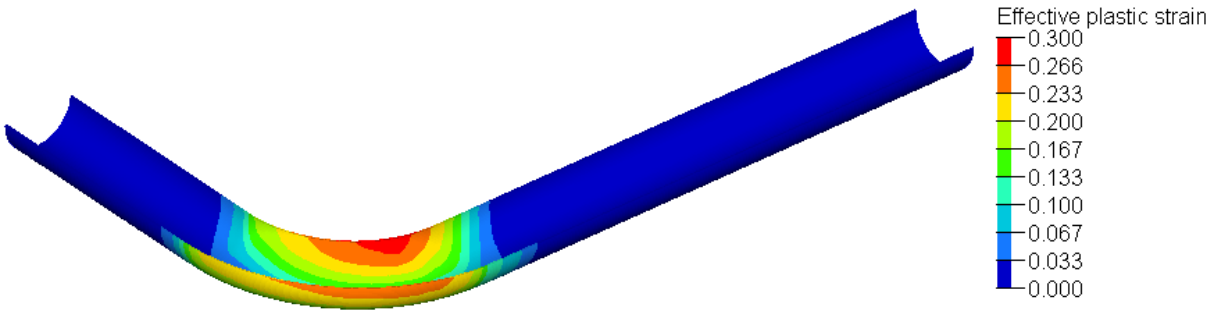

Figure 86: Effective plastic strain in pre-bent HSLA350 tube

Two levels of friction coefficient, as discussed in Chapter 3, were simulated in order to evaluate the effect of increased friction on the predicted strain and thickness variation and loads in tube bending. The set of higher friction coefficients was obtained in twist compression tests (TCT) on HSLA350 specimens. The set of lower COF corresponded to the values measured by Bardelcik [68] on DP600 specimens. Friction coefficients for the bending lubricants were not measured for the hot rolled DDQ tubes. The values of friction coefficients are tabulated in Table 8, Chapter 3.

6.1.1 Process variables – bending frictional drag

Detailed investigation of the tube bending process parameters was already performed by Dyment [41] and Bardelcik [71]. Therefore, only the predicted and measured mandrel load in tube bending was compared and presented in Figure 87 for all three alloys to provide insight into the accuracy of the prediction of process parameters in the tube bending simulations. The predicted mandrel load was underestimated using both sets of COF. At the same time, the set of higher COF produced better agreement between the predicted and measured results. The reasons for the discrepancy might come form a higher actual COF between the inside of the tube and the mandrel, variation of the actual wiper die rake angle or misalignment in the experiment [41].

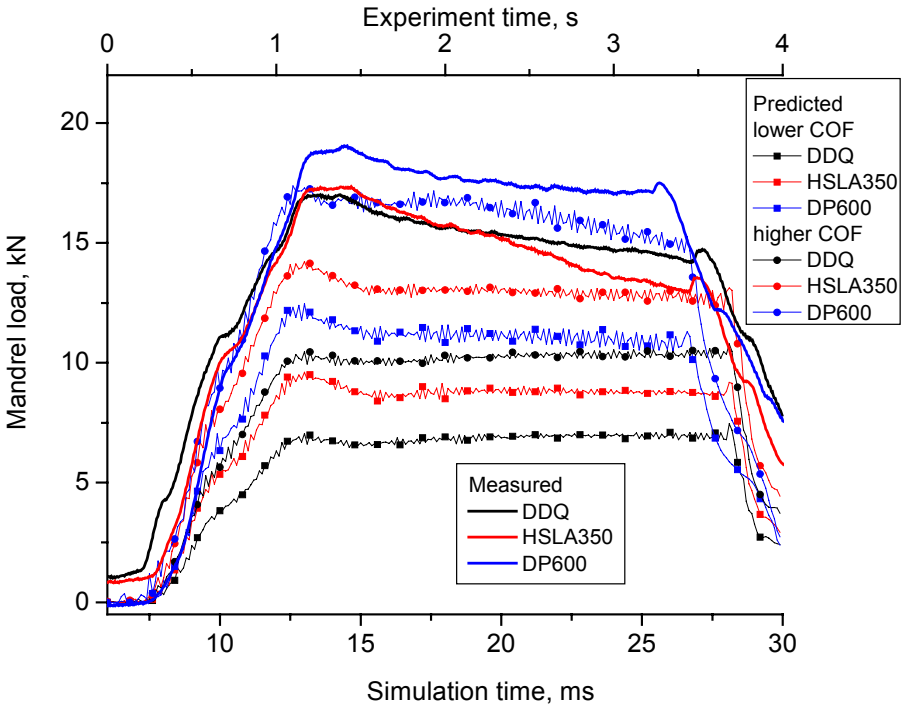

Figure 87: Predicted and measured mandrel load for tube bending of DDQ, HSLA350 and DP600 tubes

6.1.2 Strain and thickness distribution

The change in friction coefficient from low to high COF did not have an effect on predicted strain and thickness distributions for all three bent tubes, as shown in Figure 88, Figure 89 and Figure 90 for the DDQ bend. The predicted distributions using both sets of COF were virtually identical and agreed well with the experimental data. The major discrepancy between the measured and predicted strain distributions occurred on the inside of the bend, where experimental measurements were least accurate due to the poor quality of the grids. Comparison of strain and thickness predictions obtained for HSLA350 and DP600 pre-bent tubes using both COF levels also revealed negligible difference between both predictions (not shown for brevity).

The predicted strain and thickness distributions extracted from the FE simulations using the lower COF values were in close agreement with the measured distributions for all three alloys, as shown in Figure 91, Figure 92 and Figure 93. Similar to the experimental results, the predicted strain and thickness variations were almost identical for three alloys regardless of the strength of the material.

Accurate prediction of strain and thickness distribution in the bend after tube bending operation was of primary interest for further pre-bent tube hydroforming simulation in current research. Once agreement of tube bending predictions was confirmed with the experimental results, tube forming history was

transferred further through the sequence of springback and die closure to the pre-bent tube hydroforming simulation.

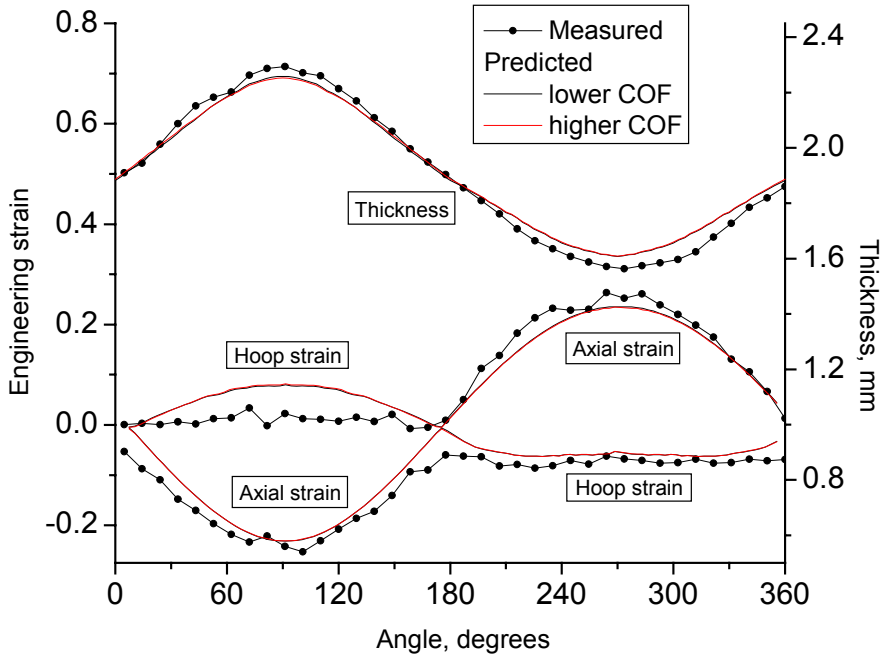

Figure 88: Predicted and measured strain and thickness distribution around the circumference of DDQ bend

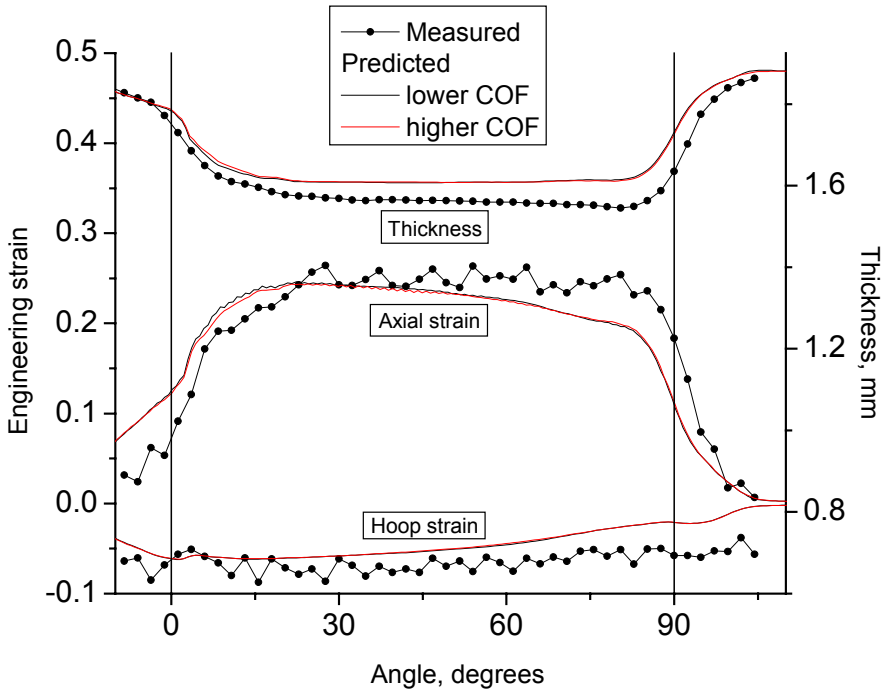

Figure 89: Predicted and measured strain and thickness distribution along the outside of DDQ bend

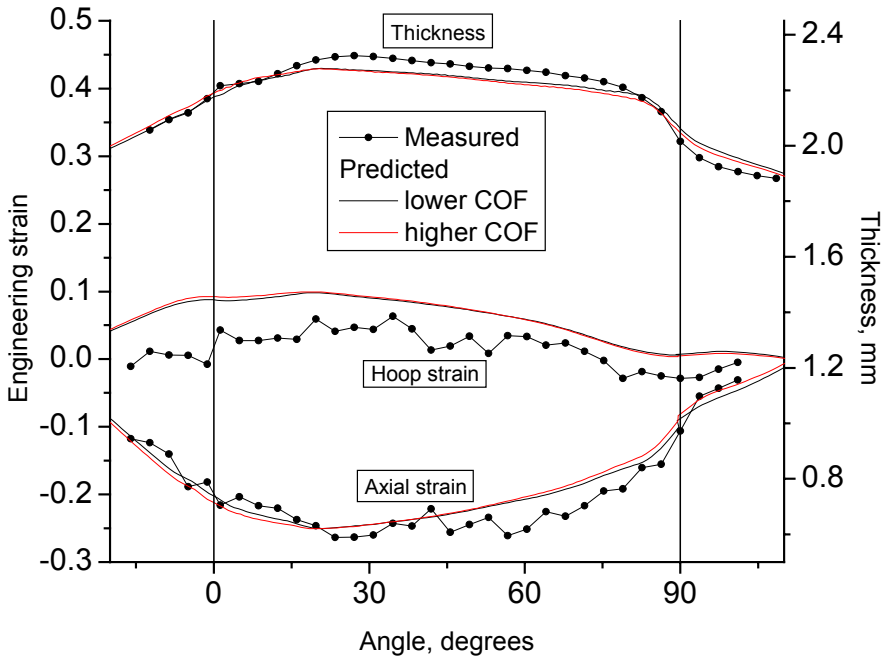

Figure 90: Predicted and measured strain and thickness distribution along the inside of DDQ bend

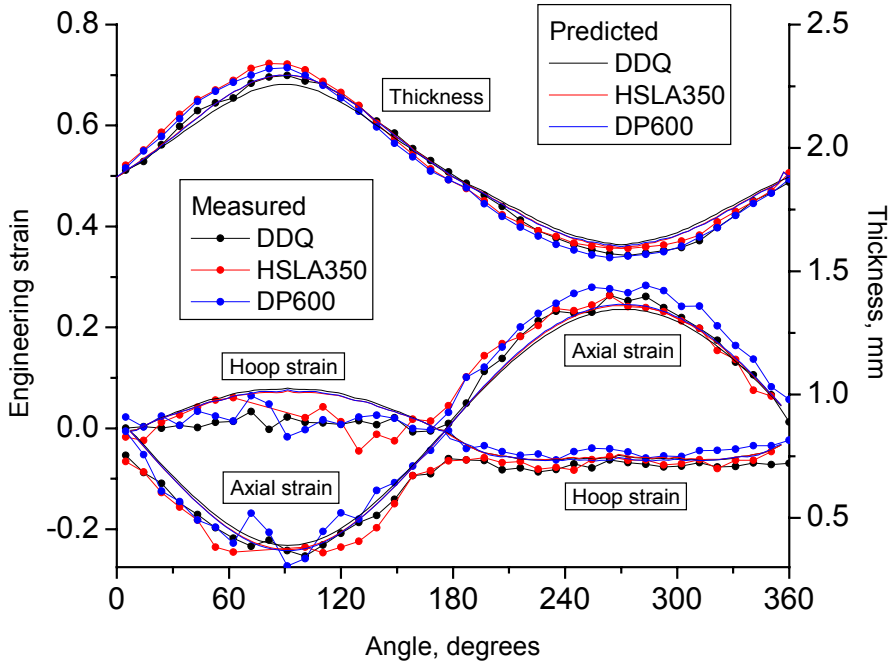

Figure 91: Predicted and measured strain and thickness distributions around the circumference of DDQ, HSLA350 and DP600 bends

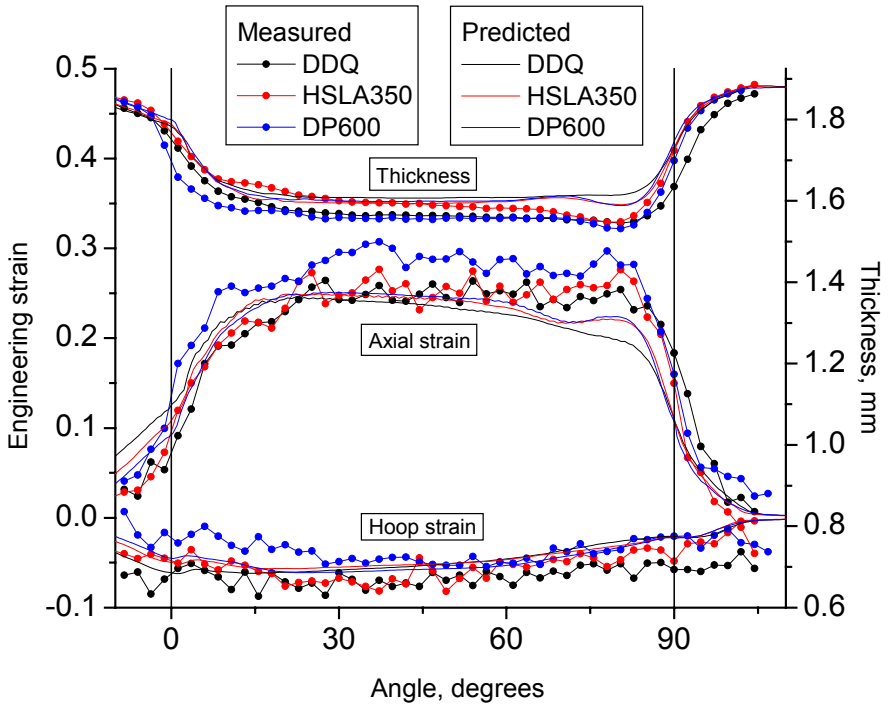

Figure 92: Predicted and measured strain and thickness distributions along the outside of DDQ, HSLA350 and DP600 bends

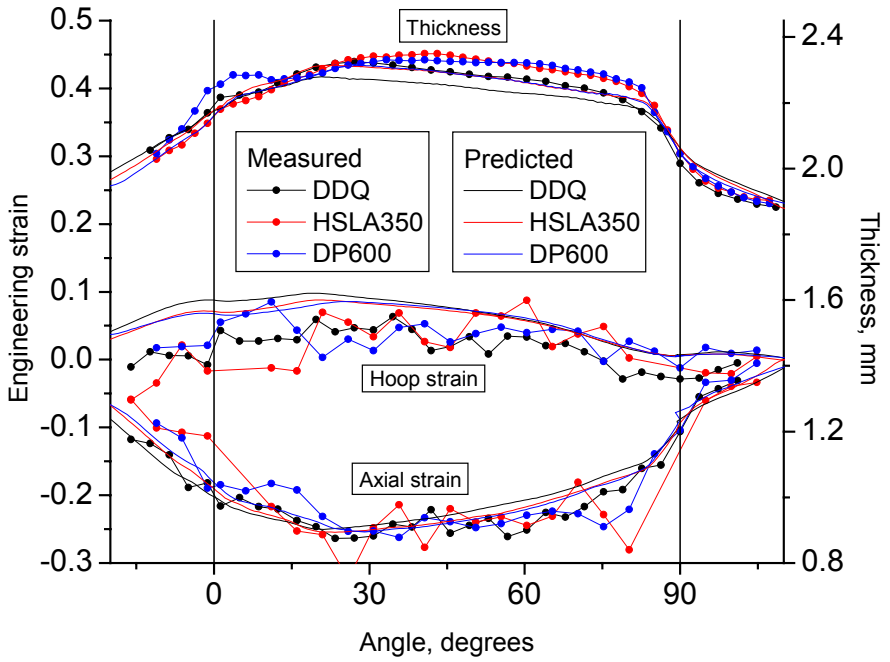

Figure 93; Predicted and measured strain and thickness distributions along the inside of DDQ, HSLA350 and DP600 bends

6.2 Straight tube hydroforming

A contour plot of effective plastic strain, shown in Figure 94 for HSLA350 straight tube hydroforming with zero end-feed, corresponding to the tube internal pressure of 90% of the measured tube burst pressure, provides good insight into the distribution of strain in straight tube hydroforming. The highest effective plastic stain in straight tube hydroforming occurred along the tangency lines, which divided the parts of the tube in contact with the die and expanding corners of the tube.

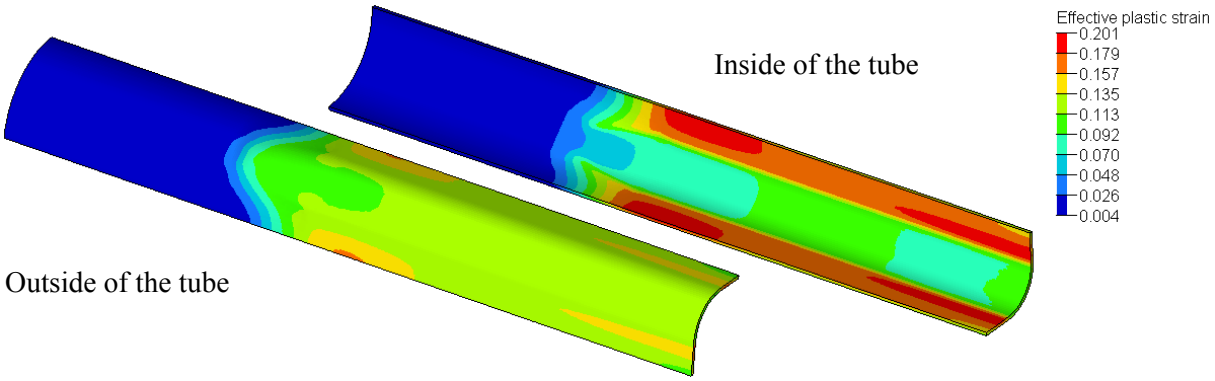

Figure 94: Effective plastic strain in HSLA350 straight tube hydroforming with zero end-feed, internal pressure 51.7 MPa (90% to burst), COF=0.03

A parametric study investigating the effect of small variation of input COF between the tube and the hydroforming die was conducted using the straight tube hydroforming simulations. The tube material properties and COF between the tube and the die were the main input characteristics for the material. The tube material properties were already confirmed in tube free expansion simulations, for which the stress-strain curve was the only material input parameter. Thus straight tube hydroforming simulations served to investigate the effect of input COF and to determine the relation between the value of COF measured in TCT and the "best" value used in the simulations in the absence of other uncertainties.

The COF measured in TCT conducted on DDQ, HSLA350 and DP600 sheet specimens, lubricated with a solid film Hydrodraw 625 lubricant was low, between 0.03 and 0.05. Therefore to investigate the effect of small variations, values of COF between 0.01 and 0.05 were simulated for DDQ and between 0.01 and 0.04 for HSLA350 and DP600 in the straight tube hydroforming simulations.

6.2.1 Effect of friction coefficient on tube end displacement

The tube end displacement was significantly affected by variation in the COF between the tube and the hydroforming die. The predicted and measured tube end displacement versus internal pressure curves for DDQ straight tube hydroforming at 0.50YS, 1.00YS and 1.50YS levels of end-feed are shown in

Figure 95. An increase in COF for each end-feed level resulted in a corresponding decrease of tube end displacement. For each end-feed level, there was a single COF value that better predicted the tube end displacement. For DDQ this value was 0.02 for 0.50YS, 0.03 for 1.00YS and 0.05 for 1.50YS level of end-feed. It should be noted that at 1.50YS end-feed, the tube end displacement was about 60 mm, which introduced significant lubricant wear, increasing COF. For more reasonable end-feed levels of 0.50YS and 1.00YS, COF was between 0.02 and 0.03, which was lower than 0.05, the value extracted from the TCT conducted on the DDQ specimens.

The measured and predicted tube end displacement versus internal pressure for hydroforming of straight HSLA350 tubes is presented in Figure 96. The same trends of decreasing tube end displacement with an increase in COF, observed for DDQ, were predicted for HSLA350. Interestingly, for all three levels of end-feed, the closest agreement of measured and predicted data was attained using a COF of 0.03, which was also the value measured in TCT on HSLA350 specimens.

The measured and predicted tube end displacement versus internal pressure for hydroforming of straight DP600 tubes is presented in Figure 97. The DP600 tube end displacement demonstrated the most inconsistent behavior with respect to the value of COF for which the predictions best matched the experiments. At 0.25YS and 1.00YS levels of end-feed, a COF of 0.04 provided the closest agreement, while at 0.50YS it was 0.02. The COF measured in TCT on DP600 specimens was 0.035, which agreed well with the results for 0.25YS and 1.00YS levels of end-feed, but not with the 0.50YS results

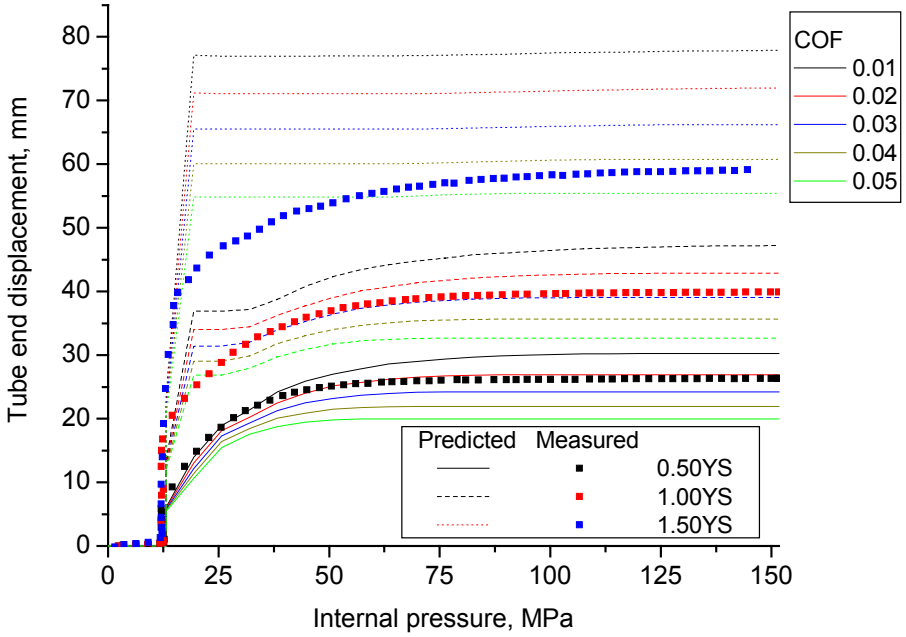

Figure 95: Predicted and measured tube end displacement for hydroformed straight DDQ tubes

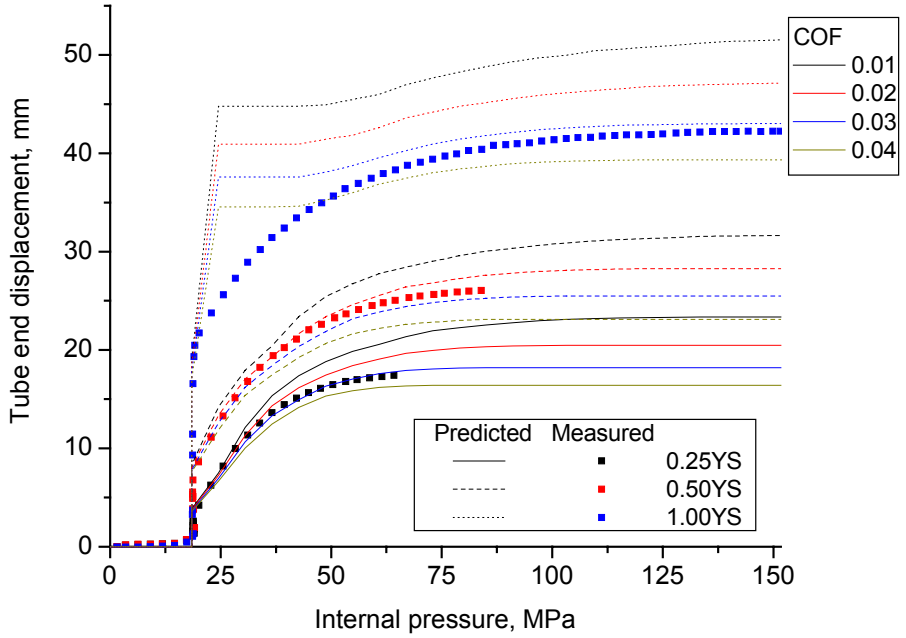

Figure 96: Predicted and measured tube end displacement for hydroformed straight HSLA350 tubes

.

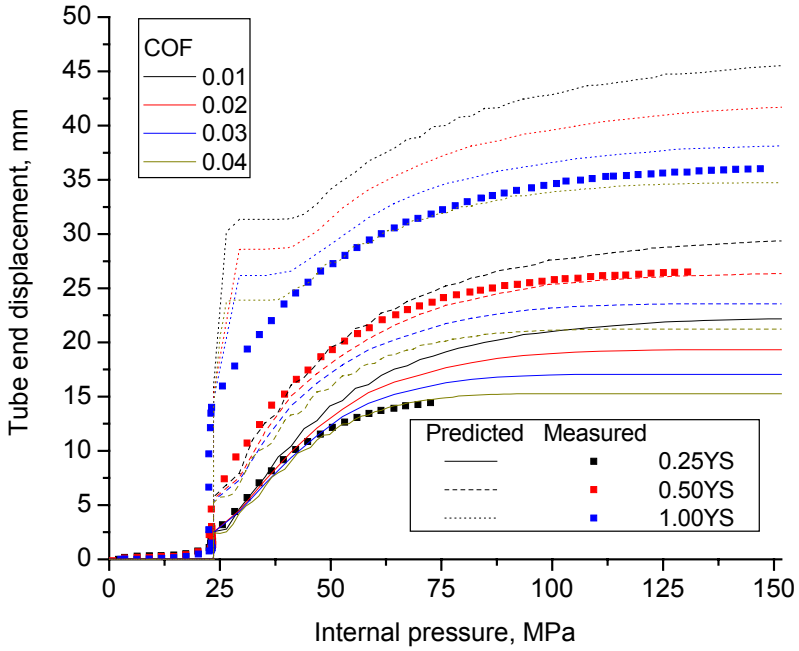

Figure 97: Predicted and measured tube end displacement for hydroformed straight DP600 tubes

A summary of the values of COF for which the models agreed well with the measured tube end displacement for straight tube hydroforming is presented in Table 15 for the three alloys.

Table 15: COF providing good agreement between predicted and measured tube end displacement

	COF				COF measured in TCT
	0.25YS	0.50YS	1.00YS	1.50YS	
DDQ	-	0.02	0.03	0.05	0.05
HSLA350	0.03	0.03	0.03	-	0.03
DP600	0.04	0.02	0.04	-	0.035

6.2.2 Effect of friction coefficient on tube corner-fill expansion

Small variations of input COF between the tube and the hydroforming die had an insignificant effect on the predicted corner-fill expansion versus internal pressure curves, as shown in Figure 98 for hydroforming of the straight HSLA350 tubes. Similar behavior was observed for the other alloys (not shown). Unlike tube end displacement, corner-fill expansion was less sensitive to small variation of input COF. Excellent agreement between numerical and experimental data presented below for HSLA350 was typical for DDQ and DP600 straight tube hydroforming as well.

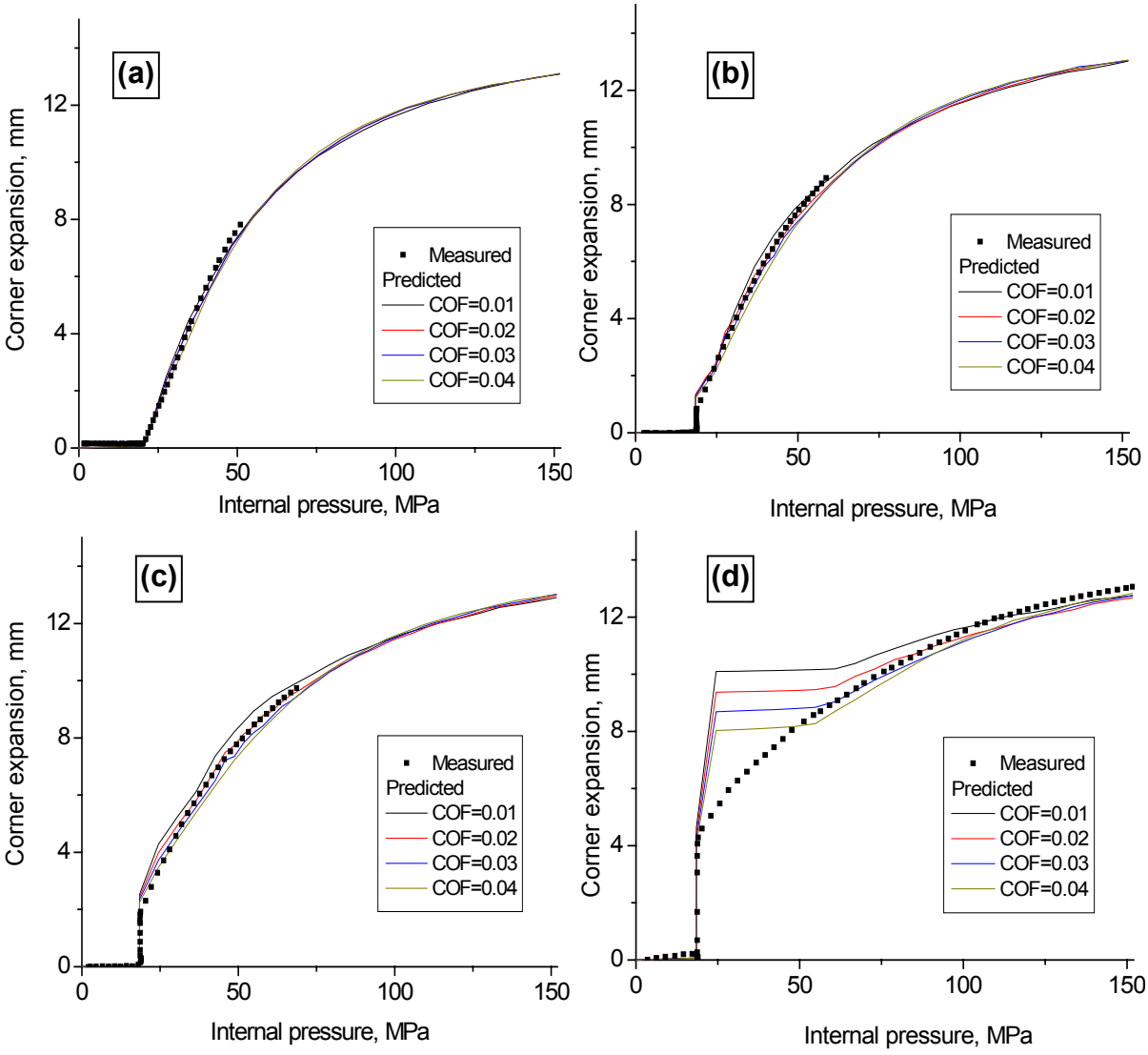

Figure 98: Measured and predicted tube corner-fill expansion versus internal pressure for hydroforming of straight HSLA350 tubes at (a) 0EF; (b) 0.25YS; (c) 0.50YS; (d) 1.00YS levels of end-feed

6.2.3 Effect of friction coefficient on strain and thickness distribution

The high sensitivity of the tube end displacement and the low sensitivity of corner-fill expansion to COF variation during the straight tube hydroforming simulations produced corresponding effects in the strain and thickness distributions around the circumference of the tube. The lower COF predicted higher tube end displacement and therefore higher compressive axial strain. The corner-fill expansion was not significantly affected by variation of COF. Therefore the average hoop strain around the circumference of the tube was also close for different values of COF. At the same time, the hoop strain and thickness distributions were more uniform for lower COF because of higher material flow into the deformation region. For a higher COF more thinning and higher hoop strains were observed, especially

at the locations of subsequent incipient necking. It confirmed that a higher COF retarded material flow and triggered localization of deformation.

The predicted and measured strain and thickness distributions for hydroforming of straight HSLA350 tubes at zero, 0.25YS, 0.50YS and 1.00YS levels of end-feed are shown in Figure 99, Figure 100, Figure 101 and Figure 102, respectively. The predicted results were extracted from the FE simulations at the internal pressure corresponding to the experimental internal pressure, when the tests were interrupted to conduct strain and thickness measurements. In the HSLA350 experiments, strain and thickness measurements were carried out at an internal pressure of 90% of tube burst pressure for zero and 0.25YS levels of end-feed, 80% for 0.50YS and maximum pressure of 151.7 MPa for 1.00YS end-feed level. The results for HSLA350 straight tube hydroforming simulations conducted with COF of 0.03 and 0.04 provided the best agreement with the experimental results. The major difference between the predicted and measured results occurred in the regions next to incipient necking locations, where the measured hoop strain and thinning were higher than predicted by the FE simulation.

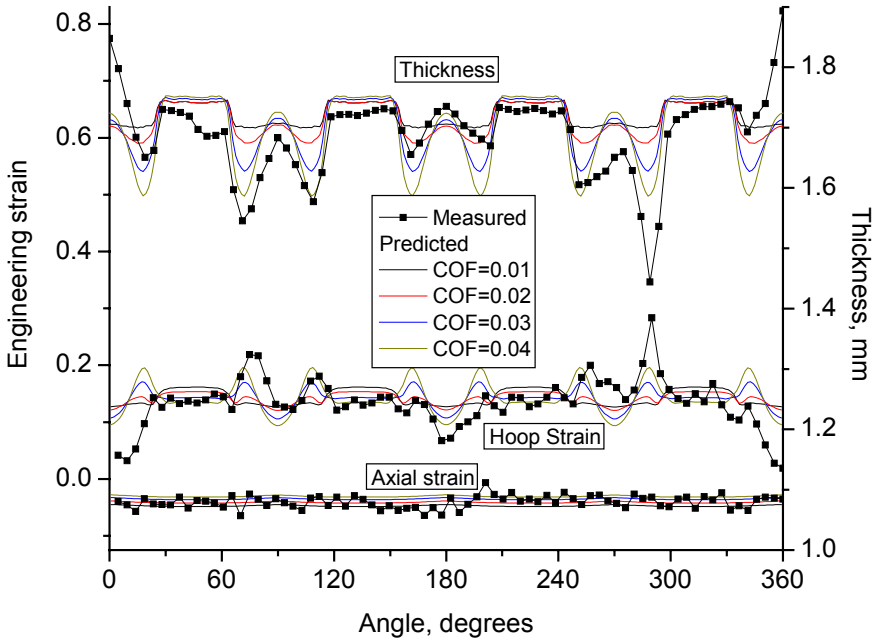

Figure 99: Predicted and measured strain and thickness distributions around the circumference of straight HSLA350 tube hydroformed with zero end-feed

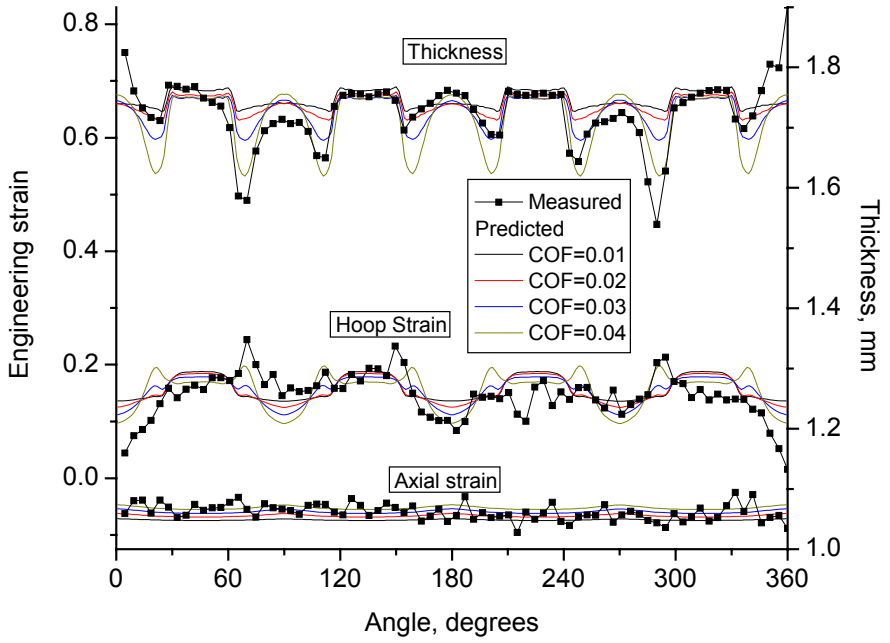

Figure 100: Predicted and measured strain and thickness distributions around the circumference of straight HSLA350 tube hydroformed at 0.25YS level of end-feed

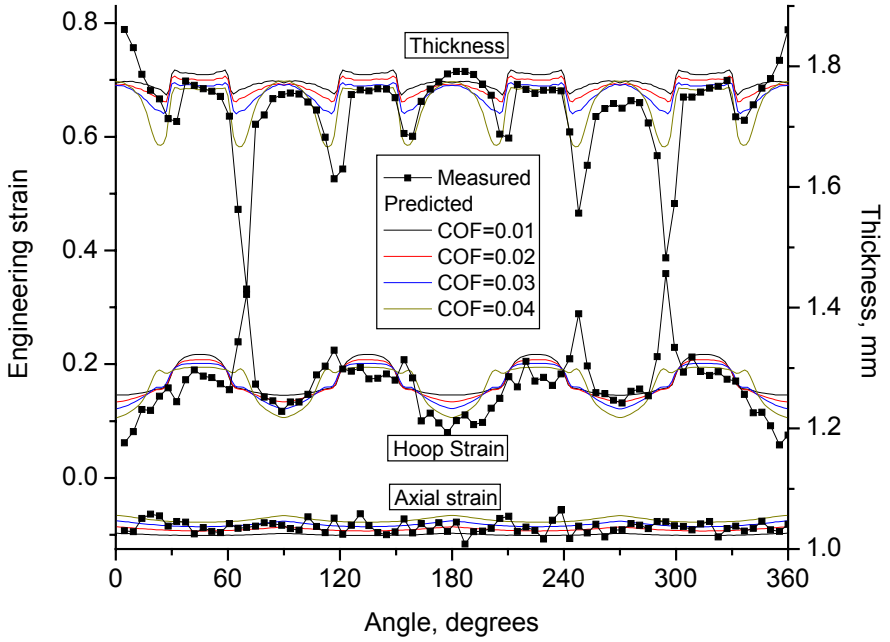

Figure 101: Predicted and measured strain and thickness distributions around the circumference of straight HSLA350 tube hydroformed at 0.50YS level of end-feed

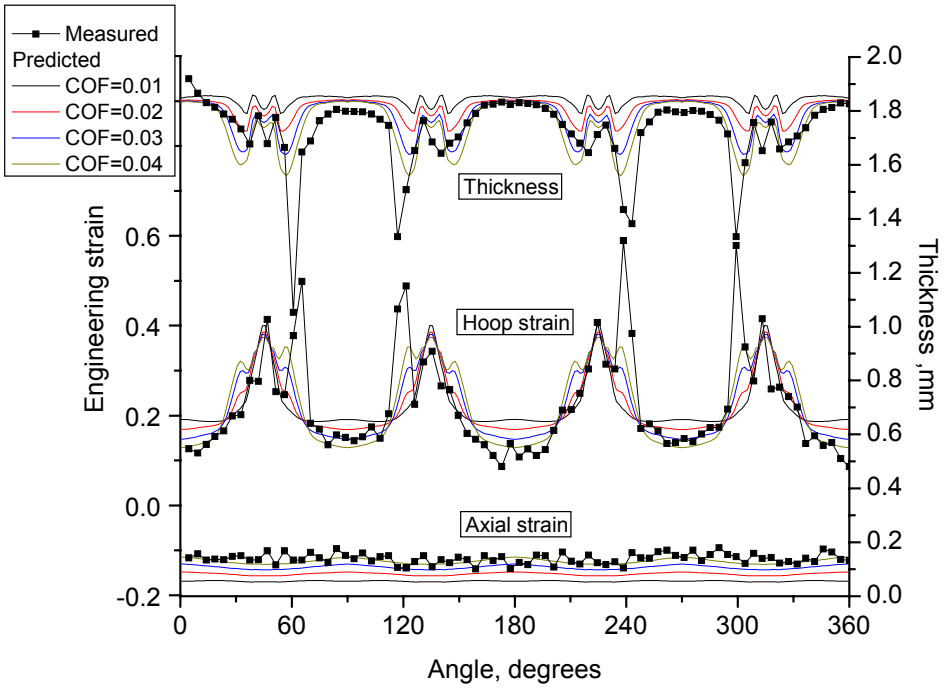

Figure 102: Predicted and measured strain and thickness distributions around the circumference of straight HSLA350 tube hydroformed at 1.00YS level of end-feed

Numerical and experimental strain and thickness distributions for hydroforming of straight DDQ and DP600 tube at 1.00YS level of end-feed are compared in Figure 103 and Figure 104, respectively. The predicted and measured results for the DDQ tubes agreed well for values of COF between 0.03 and 0.05. The DP600 predictions were in a good agreement with experiment for the COF values of 0.03 and 0.04 that also provided the best tube end displacement predictions.

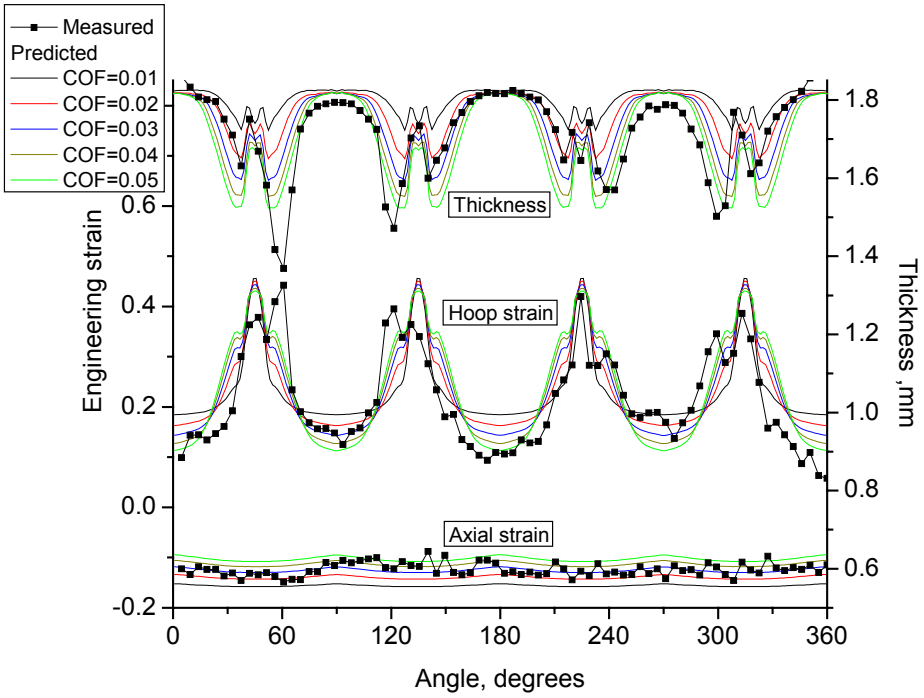

Figure 103: Predicted and measured strain and thickness distributions around the circumference of straight DDQ tube hydroformed with 1.00YS level of end-feed

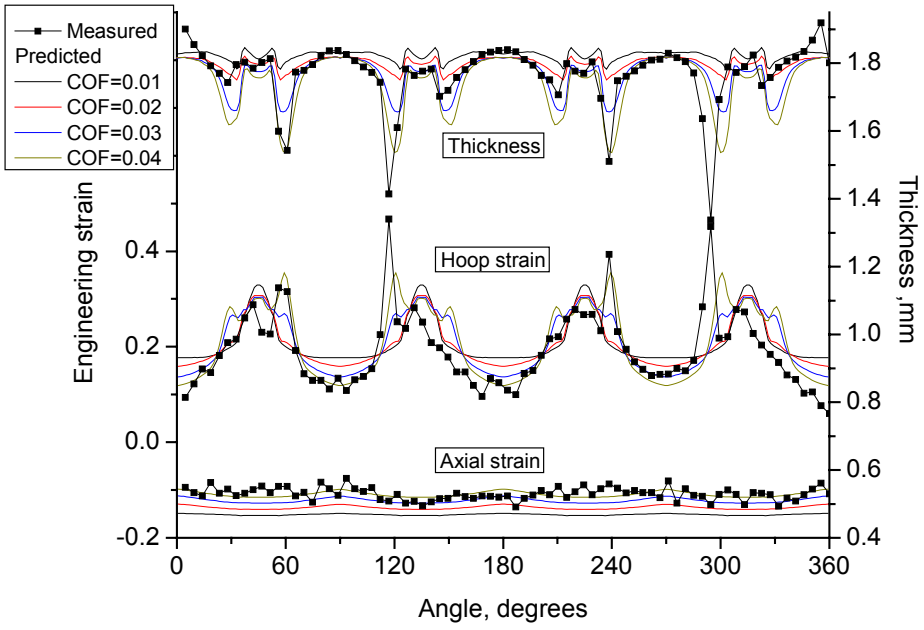

Figure 104: Predicted and measured strain and thickness distributions around the circumference of straight DP600 tube hydroformed with 1.00YS level of end-feed

6.2.4 Failure prediction using the XSFLC method - effect of friction coefficient

The Extended Stress-Based Forming Limit Curve (XSFLC) method [58] was utilized to predict failure of the tubes. To visualize necking in the tube in the FE simulations, a history variable was recorded for every element at every time step. This variable was set equal to 1, when the stress path of the element in the invariant stress space crossed the XSFLC. This meant that the material at the location of the element was predicted to neck. Once the element crossed the XSFLC, it stayed "necked" even if stress path changed its direction and went below the XSFLC.

In all straight tube hydroforming simulations the first elements to cross the XSFLC were located on the inside of the tube. With further increase of internal pressure, corresponding history variable gradually indicated necking in the adjacent elements through the thickness of the tube. The time step when all elements through the thickness of the tube at a particular location crossed the XSFLC was taken as the moment of predicted onset of necking [58]. The progression of "necked" elements through the thickness of the tube is illustrated in Figure 105, presenting a contour plot of the XSFLC variable, indicating necking using upper XSFLC limit, for HSLA350 straight tube hydroforming with zero end-feed (COF=0.03).

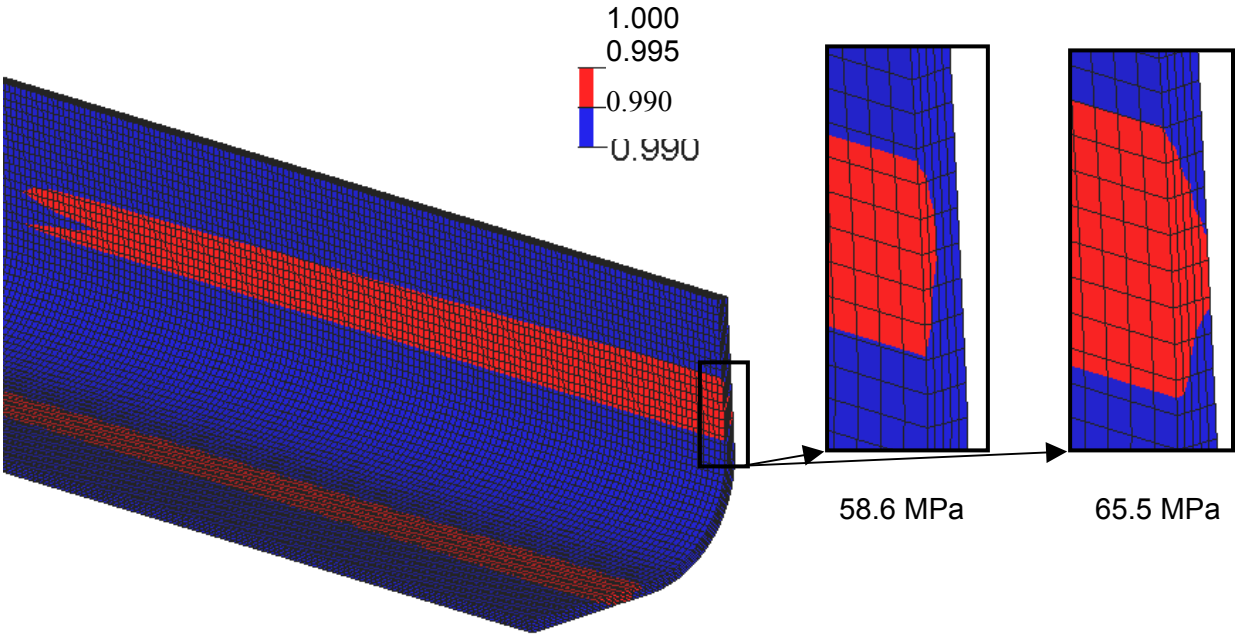

Figure 105: Prediction of the onset of necking for hydroforming of straight HSLA350 tube with zero end-feed using upper XSFLC limit for HSLA350, COF=0.03

In all straight tube hydroforming experiments the tubes necked and burst along the tangency line, as shown in Figure 106a. This line divided the parts of the tube that were in contact with the die from the free expanding corners of the tube. This location was well predicted in FE simulations for all three

alloys as shown in Figure 106b for an HSLA350 tube hydroformed with zero end-feed using upper XSFLC estimate (COF=0.03).

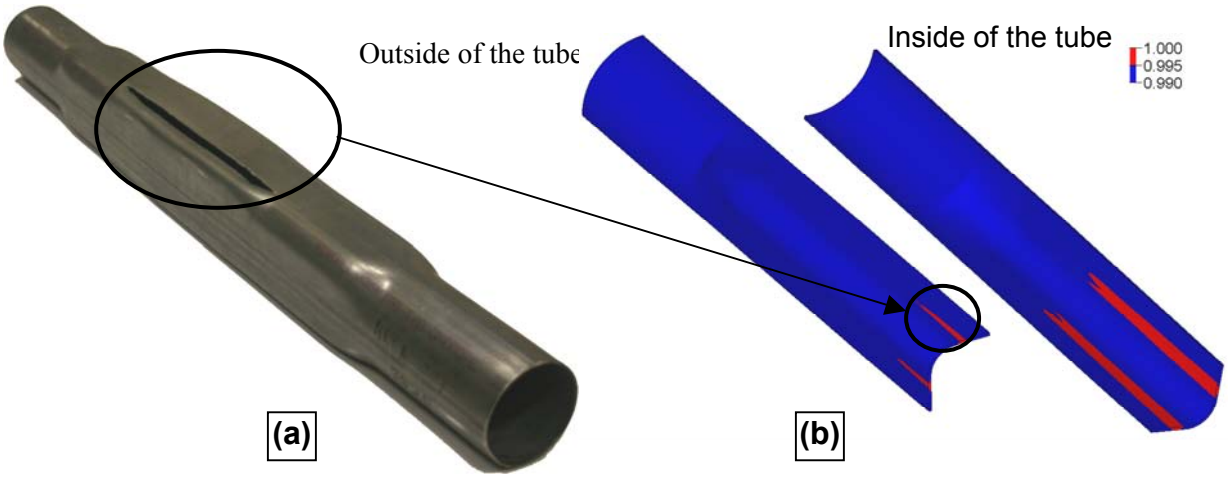

Figure 106: (a) typical experimental failure location; (b) predicted necking location in hydroforming of straight HSLA350 tube with zero end-feed using upper XSFLC limit, internal pressure of 65.5 MPa, COF=0.03,

To obtain failure predictions using the upper and lower XSFLC limits, discussed in Chapter 4, all simulations were run twice. The time step in the simulations corresponded to an increase of the tube internal pressure of about 3 MPa. Therefore, prediction of the onset of necking was checked every 3 MPa.

Comparison of the predicted and measured internal pressure at the onset of necking for hydroforming of the straight HSLA350 tubes is presented in Figure 107. In all of the HSLA350 straight tube hydroforming simulations, the onset of necking was predicted at the location observed in the experiments, except for the zero end-feed simulations with low COF of 0.01 and 0.02. In those two cases, necking was predicted along the symmetry plane, where symmetry boundary conditions were applied in the model. At higher levels of end-feed and low COF (0.01 for 0.25YS, 0.01 and 0.02 for 0.50YS and 1.00YS) upper XSFLC limit did not predict the onset of necking up to the maximum pressure of 151.7 MPa.

A higher COF decreased the predicted internal pressure at the onset of necking for both XSFLC limits. A COF of 0.03, which was measured in TCT on the HSLA350 specimens as well as was confirmed by tube end displacement results for all end-feed levels, provided the best agreement between measured and predicted internal pressure at the onset of necking. Upper and lower predictions in the simulations with a COF of 0.03 sandwiched the experimental necking pressure for all end-feed levels.

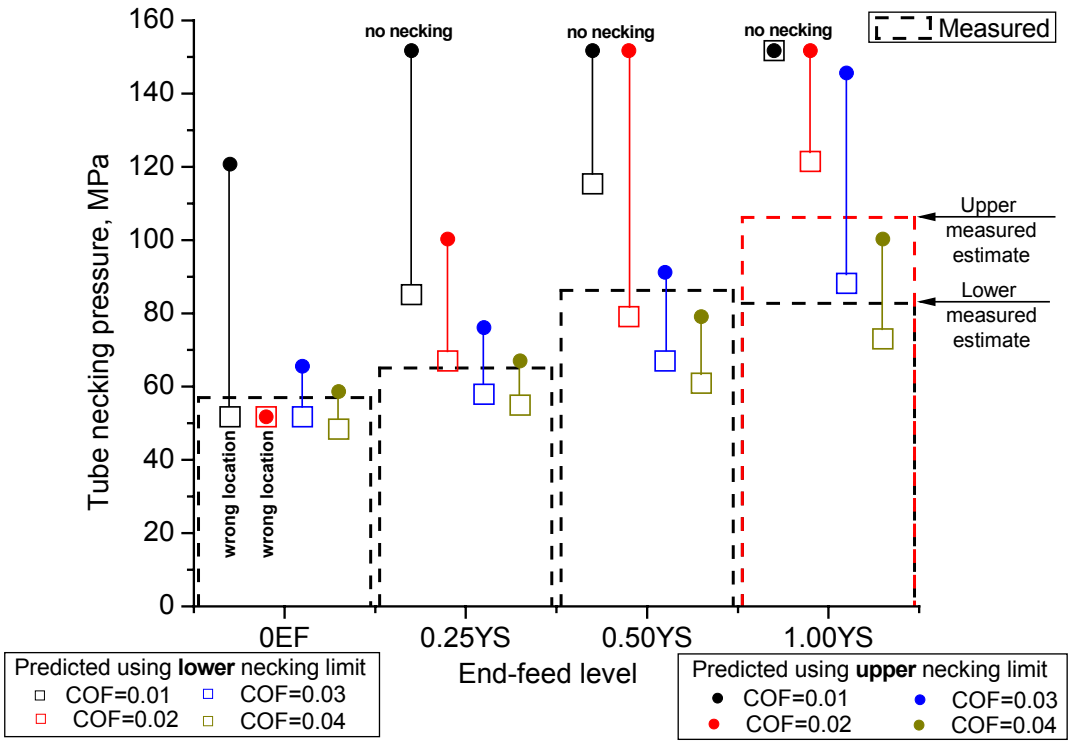

Figure 107: Measured and predicted internal pressure at the onset of necking for hydroforming of straight HSLA350 tubes

Comparison of the predicted and measured internal pressure at the onset of necking for hydroforming of the straight DP600 tubes is presented in Figure 108. Interestingly, COF that provided the best agreement between measured and predicted tube end displacement produced the best predictions of tube internal pressure at the onset of necking. For 0.25YS and 1.00YS levels of end-feed this value of COF was 0.04, while for 0.50YS it was 0.02. Evidently, the predicted pressure at the onset of necking using those values of COF sandwiched corresponding experimental results. This confirmed that the FE simulations predicted necking well using the XSFLC method when the COF accurately predicted the parameters of hydroforming process. For the zero end-feed case, the numerical results mildly over-predicted the internal pressure at the onset of necking using all COF. At the same time, a COF of 0.04, which was confirmed to provide the best agreement between experimental and numerical results for the next end-feed level of 0.25YS, produced the closest estimate.

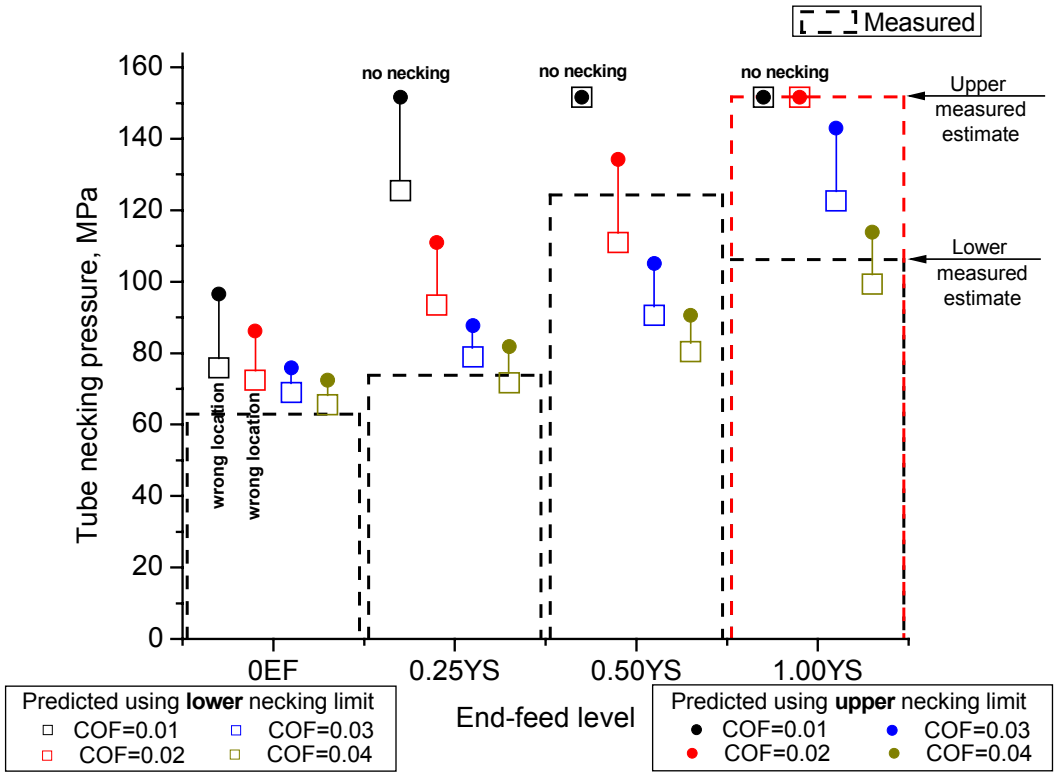

Figure 108: Measured and predicted internal pressure at the onset of necking for hydroforming of straight DP600 tubes

Comparison of the predicted and measured internal pressure at the onset of necking for hydroforming of the straight DDQ tubes is presented in Figure 109. In the experiments, none of the tubes burst, although necking was observed at all end-feed levels. Additional tests were conducted to evaluate approximate experimental limits of necking initiation. Therefore it was difficult to compare experimental and predicted results for DDQ straight tube hydroforming. None of the simulations with an upper XSFLC limit predicted necking at any end-feed level or COF up to the maximum internal pressure of 151.7 MPa. The simulations conducted with the COF of 0.03, that provided better agreement between predicted and measured DDQ tube end displacement, sandwiched the experimental estimates.

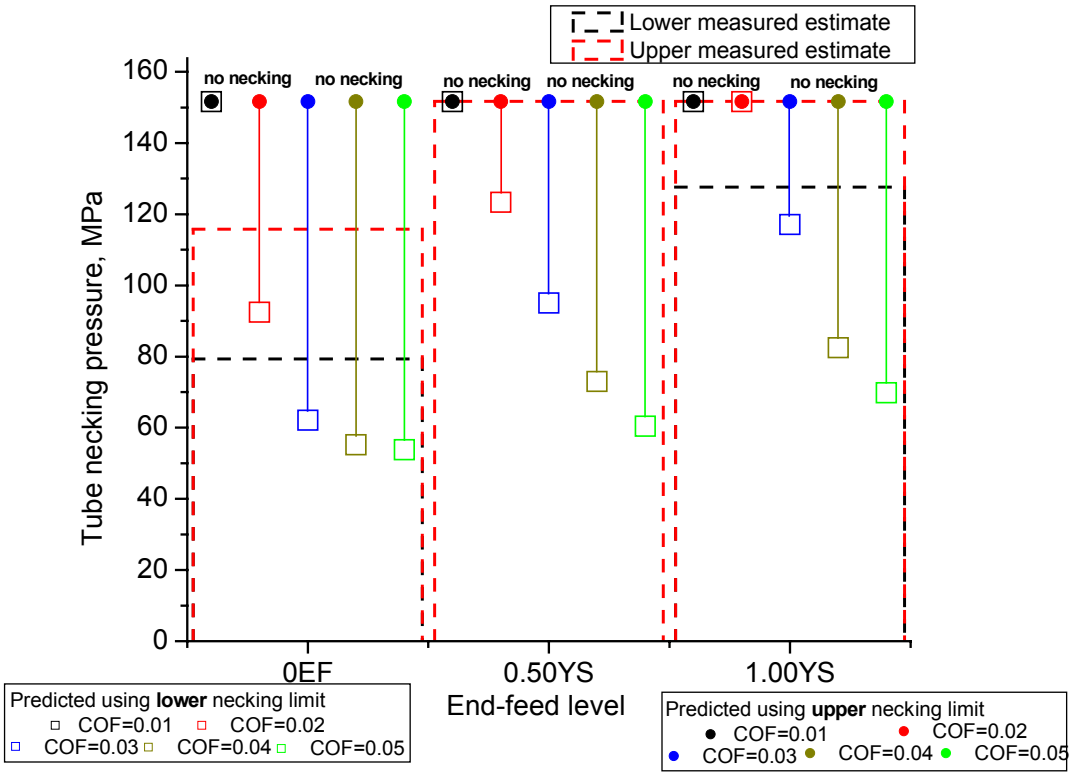

Figure 109: Measured and predicted internal pressure at the onset of necking for hydroforming of straight DDQ tubes

A summary of predicted tube internal pressure at the onset of necking for DDQ, HSLA350 and DP600 is presented in Table 16. The measured and predicted tube corner-fill expansion at the onset of necking was not separately compared, because tube expansion versus internal pressure was already shown to be predicted well by FE simulations. Therefore if the tube internal pressure at the onset of necking was predicted accurately, it resulted in accurate prediction of corresponding expansion.

Table 16: Measured and predicted internal pressure at the onset of necking for hydroforming of straight DDQ, HSLA350 and DP600 tubes

	End-feed level	Predicted necking pressure, MPa										Experimental necking pressure, MPa	
		COF=0.01		COF=0.02		COF=0.03		COF=0.04		COF=0.05			
		Lower	Upper	Lower	Upper	Lower	Upper	Lower	Upper	Lower	Upper		
DDQ	0.00	151.7	151.7	92.4	151.7	62.1	151.7	55.2	151.7	53.8	151.7	79.3	115.8
	0.50	151.7	151.7	123.3	151.7	95.0	151.7	72.9	151.7	60.3	151.7	-	151.7
	1.00	151.7	151.7	151.7	151.7	117.0	151.7	82.4	151.7	69.8	151.7	127.6	151.7
HSLA350	0.00	51.7	120.7	51.7	51.7	51.7	65.5	48.3	58.6	-	-	57.0	
	0.25	85.1	151.7	66.9	100.2	57.8	76.0	54.8	66.9	-	-	65.1	
	0.50	115.4	151.7	79.0	151.7	66.9	91.1	60.9	79.0	-	-	86.3	
	1.00	151.7	151.7	121.4	151.7	88.1	145.6	73.0	100.2	-	-	82.7	106.2
DP600	0.00	75.8	96.5	72.4	86.2	69.0	75.8	65.5	72.4	-	-	62.9	
	0.25	125.5	151.7	93.5	110.9	78.9	87.6	71.6	81.8	-	-	73.8	
	0.50	151.7	151.7	110.9	134.2	90.5	105.1	80.4	90.5	-	-	124.3	
	1.00	151.7	151.7	151.7	151.7	122.6	143.0	99.3	113.8	-	-	106.2	151.7

6.3 Pre-bent tube hydroforming

The predicted effective plastic strain in a pre-bent HSLA350 non-hydroformed tube and a tube hydroformed at 0.50YS level of end-feed is shown in Figure 110. The results for the hydroformed tube were extracted at an internal pressure of 49.6 MPa, corresponding to 90% of experimental tube burst pressure. Comparison of plastic strain distributions in non-hydroformed and hydroformed tubes demonstrated that in pre-bent tube hydroforming a significant amount of deformation occurred on the inside of the bend. Plastic strains on the outside of the hydroformed bend remained comparable to those of the non-hydroformed tube, while on the inside of the bend the strains increased dramatically.

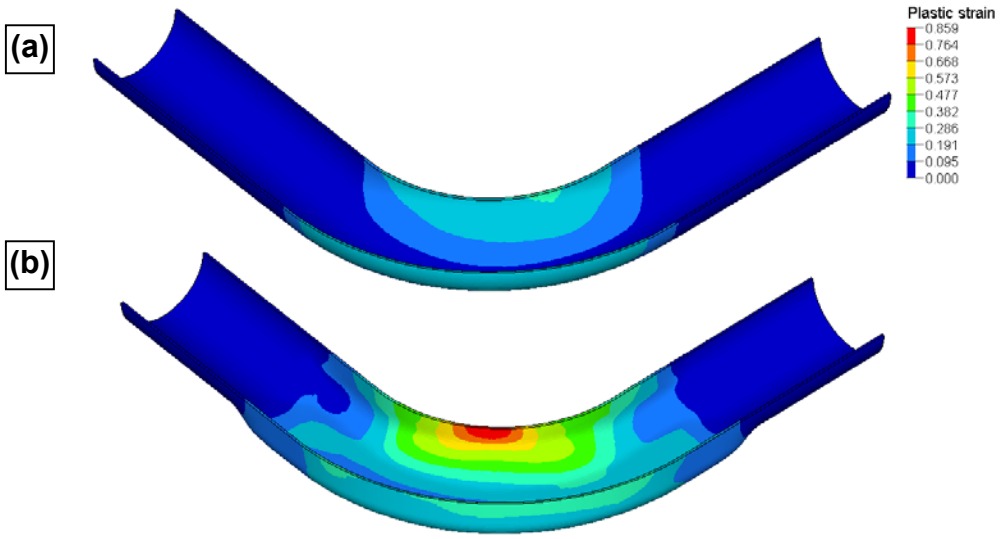

Figure 110: Effective plastic strain in (a) pre-bent non-hydroformed HSLA350 tube; (b) pre-bent HSLA350 tube hydroformed at 0.50YS level of end-feed, internal pressure 49.6 MPa

The results of the parametric study of the effect of COF between the tube and the hydroforming die in the straight tube hydroforming simulations were utilized in the pre-bent tube hydroforming simulations. The HSLA350 and DP600 straight tube hydroforming simulations confirmed that the COF obtained in TCT predicted the experimental results reasonably well for both materials. Therefore the HSLA350 and DP600 pre-bent tube hydroforming simulations were carried out with values of COF measured in the TCT, tabulated in Table 15. In the DDQ straight tube hydroforming simulations, a COF of 0.03, lower than that measured in TCT, predicted experimental data better and therefore was utilized in DDQ pre-bent tube hydroforming simulations.

6.3.1 Tube end-feed displacement

The displacement of the two ends of the tube in pre-bent tube hydroforming was different, but within 5% from each other. Therefore the predicted and measured tube end displacement versus internal pressure was averaged over the two ends of the tube and is presented in Figure 111.

Best agreement between the predicted and measured tube end displacement for both end-feed levels was observed for HSLA350. The COF of 0.03 resulted in good prediction of tube end displacement, demonstrating consistent behavior.

The predicted tube end displacement for pre-bent DP600 tube hydroforming was slightly less than the experimental results for both end-feed levels, but still agreed reasonably well. The reason for this under-prediction might be a slightly lower actual COF, compared to the value of 0.035 measured in TCT and confirmed by the straight tube hydroforming simulations.

The tube end displacement in pre-bent DDQ tube hydroforming was slightly under-predicted for 0.25YS level of end-feed and significantly under-predicted for 0.50YS level of end-feed. Although the COF of 0.03 utilized in FE simulation was confirmed by straight tube hydroforming simulations, in pre-bent tube hydroforming the actual COF was even lower.

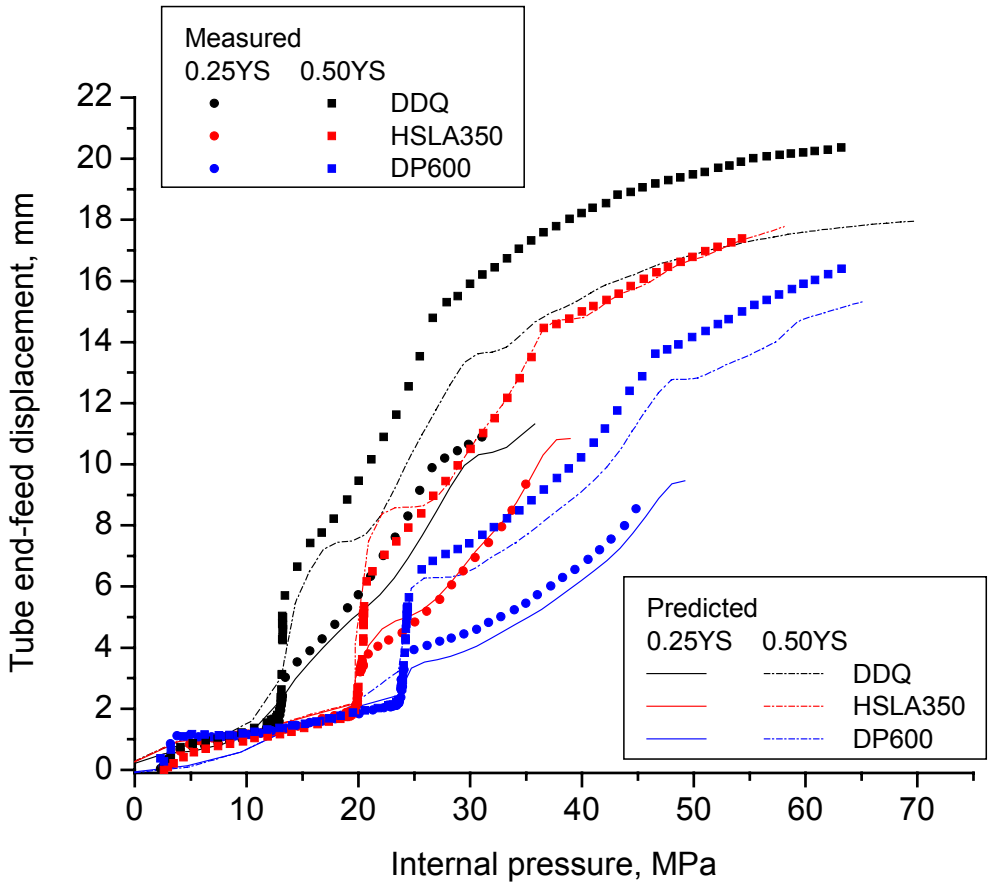

Figure 111: Average tube end displacement versus internal pressure for hydroforming of pre-bent DDQ, HSLA350 and DP600 tubes

6.3.2 Tube corner-fill expansion

The measured and predicted tube corner-fill expansion at the inside and outside of the bend in DDQ, HSLA350 and DP600 pre-bent tube hydroforming is shown in Figure 112, Figure 113 and Figure 114 respectively. There was a good agreement between model and experiment for the HSLA350 and DP600 data. The main discrepancy between predicted and measured results was observed on the inside of the bend at the beginning of the process before application of end-feed. These differences are attributed to ovalization of the tube after bending.

The level of agreement between the measured and predicted expansion for the DDQ pre-bent tube hydroforming was the poorest among the three alloys. The error was related to inferior predictions of tube end displacement for the pre-bent DDQ tubes. In pre-bent tube hydroforming, tube end displacement had a significant effect on tube expansion. The tube within the pre-bent die was more flexible than in the straight die, and application of end-feed load without internal pressure already

introduced positive expansion of the outside of the bend and "negative" expansion of the inside of the bend.

The effect of "negative" corner-fill expansion was captured well by the FE models for the three alloys. FE simulation eventually predicted positive expansion of the inside of the bend for all the alloys and end-feed levels. In the experiments with lower levels of end-feed the tube burst before the inside of the bend pulled back to the inside radius of the hydroforming die. Therefore the corner-fill expansion of the inside of the bend remained negative for low end-feed cases. The length of the LVDT probe located on the inside of the bend during the tests was limited to measure negative expansion up to –5 mm only. Therefore, if the tube continued to move away from the inside radius of the hydroforming die, the reading of the LVDT remained around –5 mm. That's why the predicted negative expansion of the inside of the bend at higher levels of end-feed was higher than that measured in the experiments.

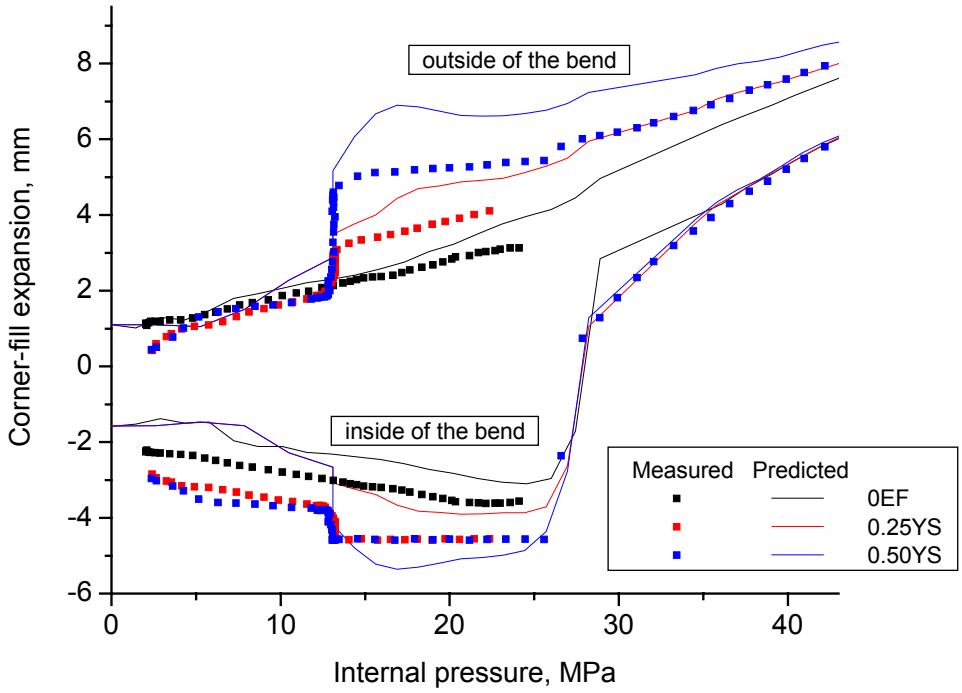

Figure 112: Corner-fill expansion of the inside and outside of the bend for hydroforming of pre-bent DDQ tubes

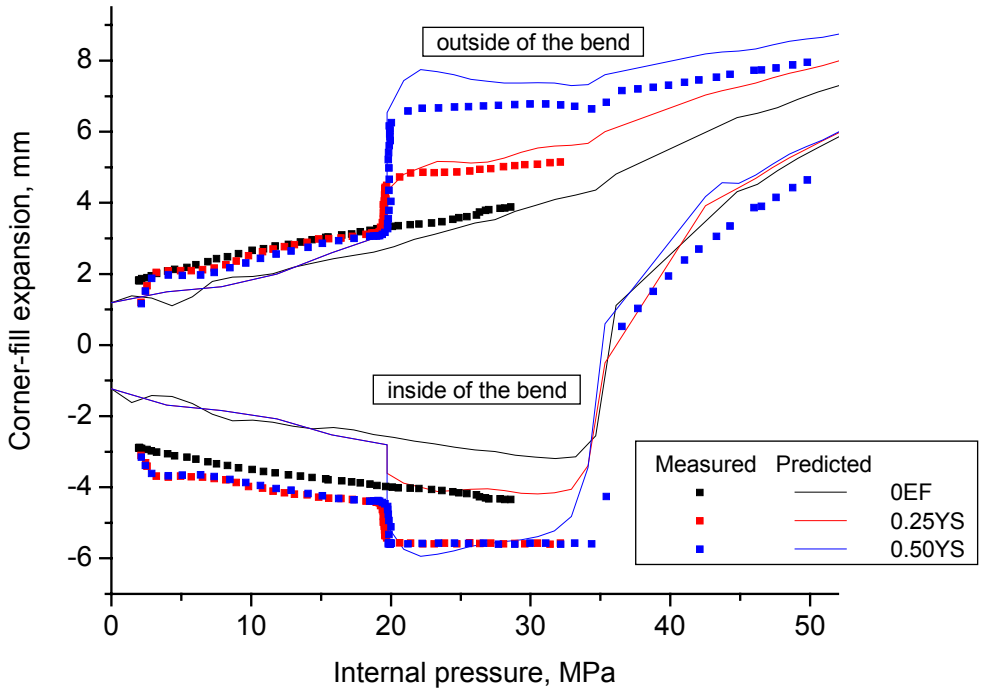

Figure 113: Corner-fill expansion of the inside and outside of the bend for hydroforming of pre-bent HSLA350 tubes

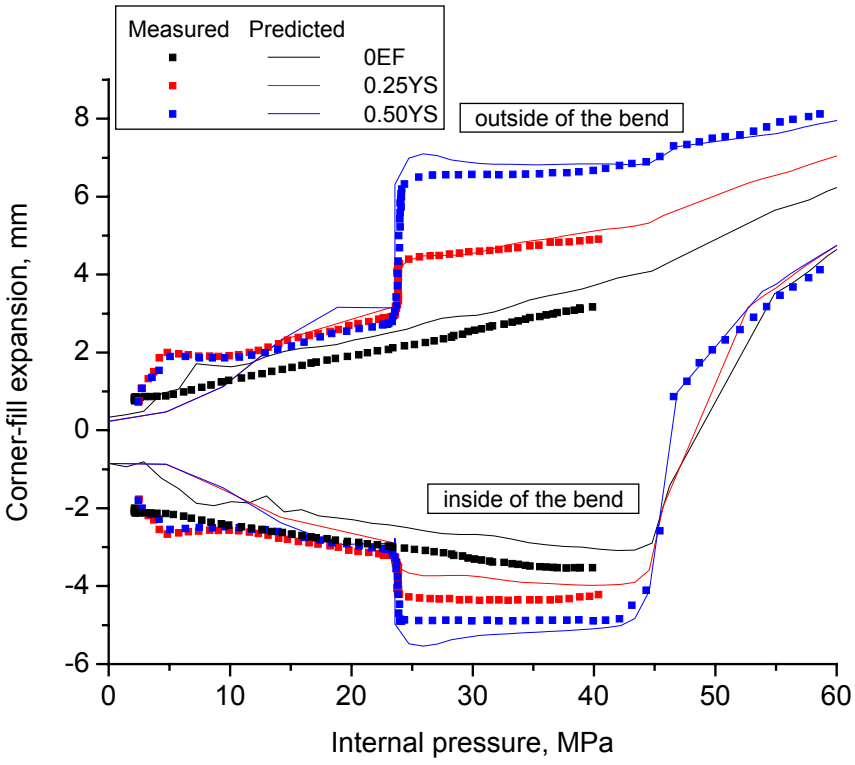

Figure 114: Corner-fill expansion of the inside and outside of the bend for hydroforming of pre-bent DP600 tubes

6.3.3 Strain and thickness distribution

The predicted strain and thickness distributions for hydroforming of the pre-bent HSLA350 tubes at zero, 0.25YS and 0.50YS levels of end-feed are shown in Figure 115. The presented results were extracted from FE simulations at the internal pressure corresponding to 90% of the experimental tube burst pressure. Pre-bent tubes hydroformed at zero and 0.25YS levels of end-feed did not undergo any significant expansion up to the internal pressure of 90% of tube burst pressure. The only change was a slight decrease of axial strain on the outside of the bend at 0.25YS level of end-feed due to compressive end-feed load and earlier forming of the outside of the bend. The strain and thickness distributions on the inside of the bend for both end-feed levels were predicted to be the same and remained unchanged compared to the non-hydroformed tube. At an end-feed level of 0.50YS, the tube experienced significant expansion, especially on the inside of the bend. This resulted in a dramatic increase of thinning, hoop strain and compressive axial strain. On the outside of the bend the strain and thickness for 0.50YS level of end-feed remained virtually unchanged. Only the axial strain on the outside of the bend slightly decreased due to the higher compressive end-feed load.

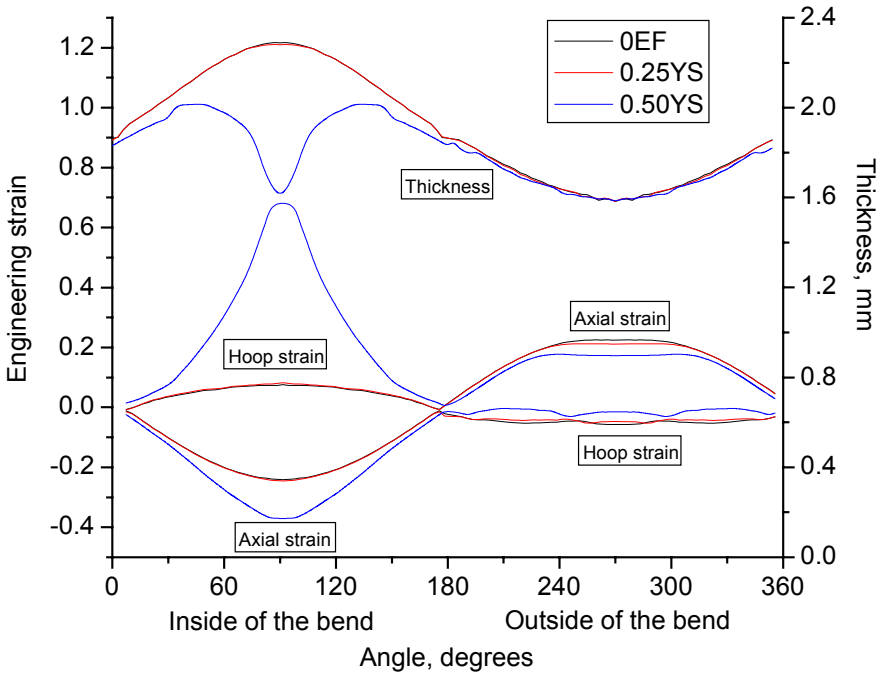

Figure 115: Predicted strain and thickness distributions for hydroforming of pre-bent HSLA350 tubes

Comparison of the predicted and measured strain and thickness distributions for the pre-bent HSLA350 tube hydroformed at zero, 0.25YS and 0.50YS levels of end-feed are presented in Figure 116, Figure 117 and Figure 118 respectively. For zero and 0.25YS levels of end-feed the predicted and measured results had an excellent agreement. A significant discrepancy occurred on the inside of the bend for the

hoop strain, where, due to poor quality of the grids, the strain measurements were least accurate. For 0.50YS level of end-feed, the agreement between the measured and predicted strains and thickness was excellent for the outside of the bend. On the inside of the bend, both experimental and numerical distributions indicated significant decrease of thickness compared to the non-hydroformed tubes. FE simulations predicted a point with minimum thickness in the middle of the inside of the bend, while in the experiments the same spike was not as apparent. The spike in the curve may be due to buckling of the tube at the early stages of pressurization and end-feed. It may be possible that the model over-predicted the severity of the buckling. A drop in the measured thickness distribution on the neutral axis of the bend due to incipient necking was not captured by the FE simulations.

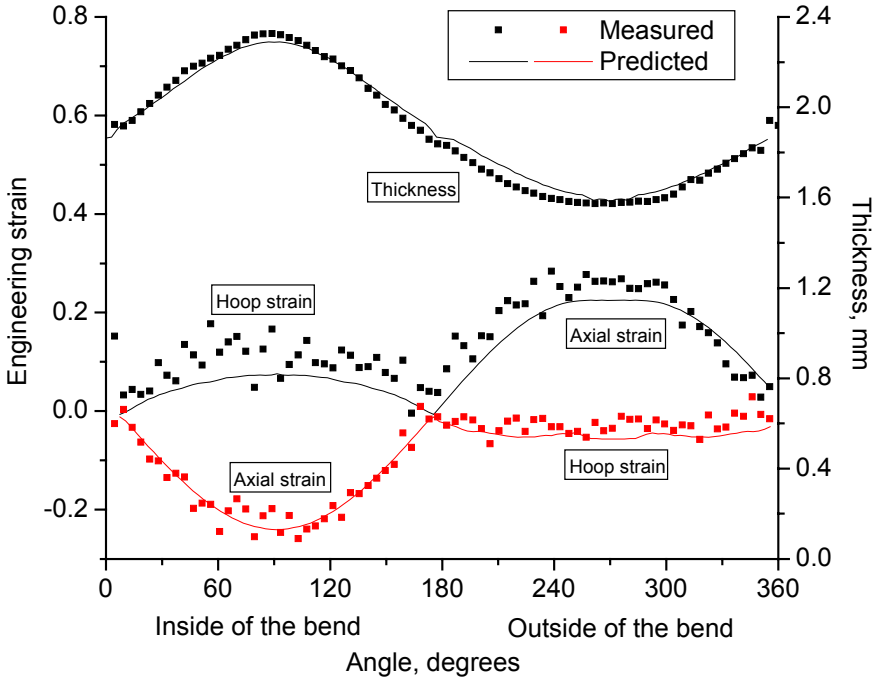

Figure 116: Predicted and measured strain and thickness distributions for hydroforming of pre-bent HSLA350 tube at zero end-feed, interrupted at 90% of tube burst pressure

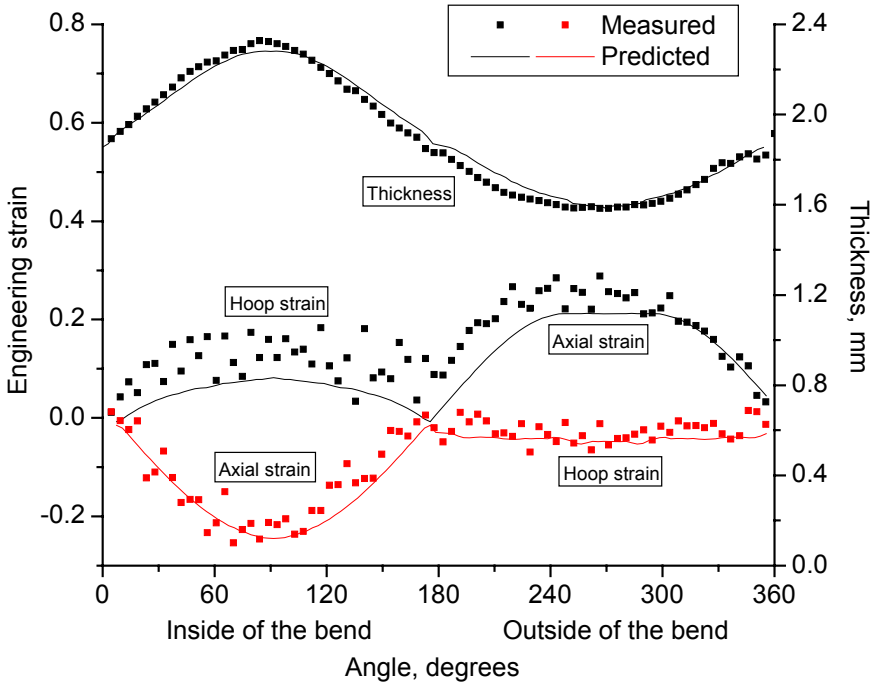

Figure 117: Predicted and measured strain and thickness distributions for hydroforming of pre-bent HSLA350 tube at 0.25YS level of end-feed, interrupted at 90% of tube burst pressure

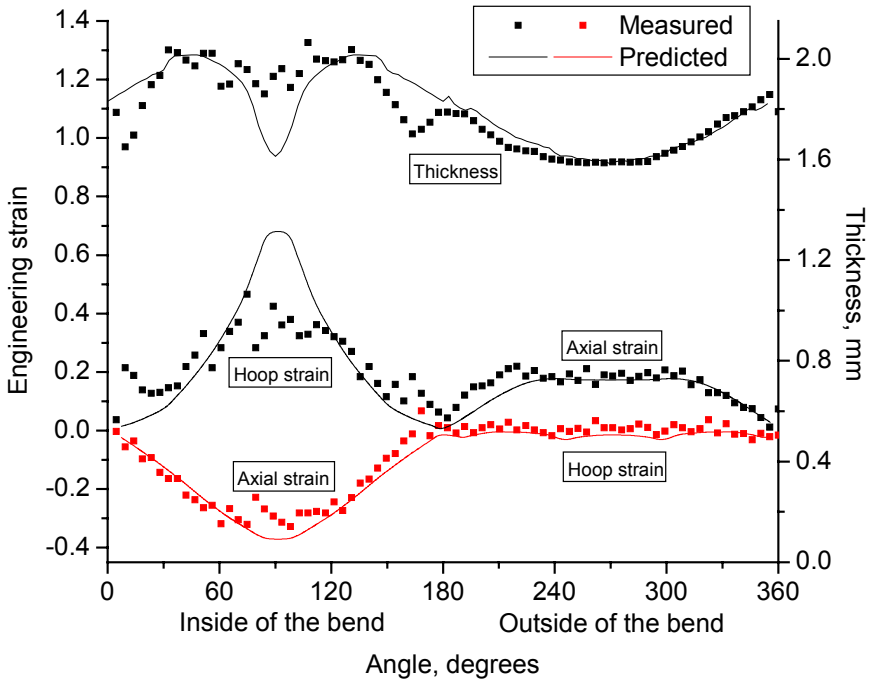

Figure 118: Predicted and measured strain and thickness distributions for hydroforming of pre-bent HSLA350 tube at 0.50YS level of end-feed, interrupted at 90% of tube burst pressure

The predicted and measured strain and thickness distributions for hydroforming of the pre-bent DP600 and DDQ tubes are presented only for the end-feed level of 0.50YS in Figure 119 and Figure 120,

respectively. For both alloys, the predicted thickness and strain variations on the outside of the bend had excellent agreement with the experimental results. The same trends for the predicted strain and thickness distributions on the inside of the bend demonstrated for the HSLA350 tubes were observed for DDQ and DP600. Spikes in the strain and thickness distributions in the DDQ tubes on the neutral axis were not captured by predicted distributions. Those spikes were probably attributed to incipient necking in the experiment that were not captured by the FE simulation.

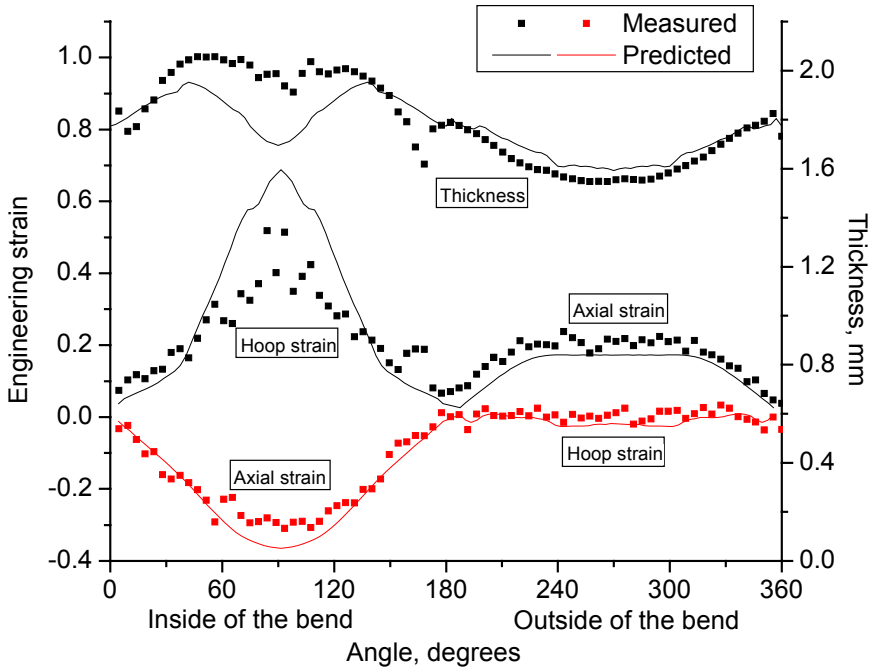

Figure 119: Predicted and measured strain and thickness distributions for hydroforming of pre-bent DP600 tube at 0.50YS level of end-feed, interrupted at 90% of tube burst pressure

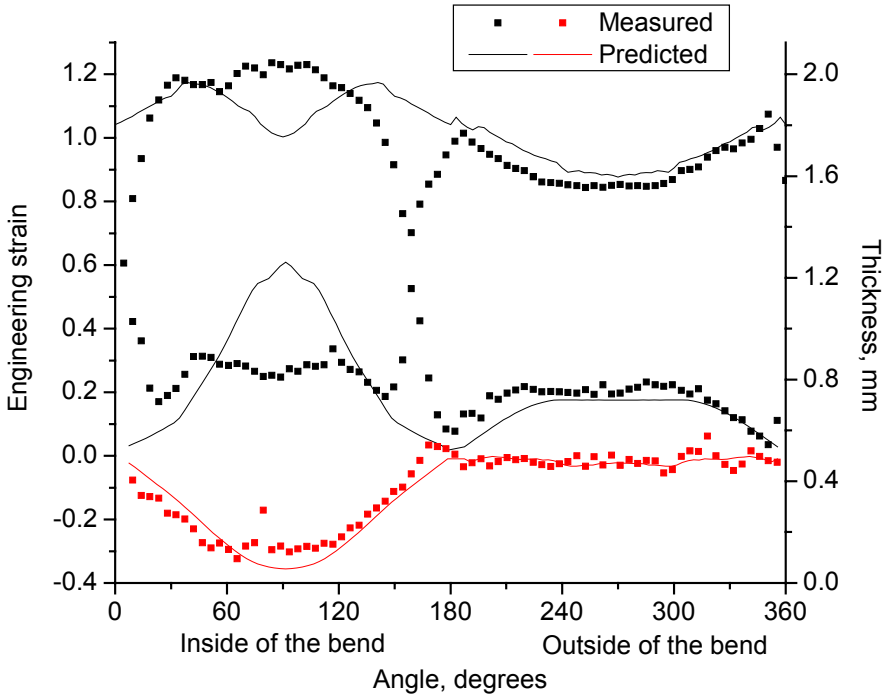

Figure 120: Predicted and measured strain and thickness distributions for hydroforming of pre-bent DDQ tube at 0.50YS level of end-feed, interrupted at 70% of tube burst pressure

6.3.4 Failure prediction in pre-bent tube hydroforming using the XSFLC method

Contour plots of the variable indicating predicted necking according to the XSFLC method for DP600 pre-bent tube hydroforming with zero end-feed are shown in Figure 121. The black arrow shows predicted failure location that corresponded to the experimental failure location. Two additional failure locations on the inside and outside of the bend are marked with white arrows. The pre-bent tube hydroforming simulations predicted several potential failure locations: on the inside of the bend; on the outside of the bend; and, along the neutral axis. The typical failure location in the DDQ, HSLA350 and DP600 pre-bent tube hydroforming experiments was along the neutral axis of the bend, as shown in Figure 121 for a DP600 tube, hydroformed with zero end-feed. Only in hydroforming of the pre-bent HSLA350 tubes with zero end-feed was failure located on the outside of the bend. The observed failure locations were discussed in detail in Chapter 5.

In all simulations, the first location to be indicated as failure location was on the inside of the bend. As soon as the inside of the bend started to return to contact the inside radius of the die, the XSFLC method predicted failure in all cases. This failure location prediction was followed by the locations along the neutral axis and outside of the bend, which usually occurred around the same time. It should

be noted that application of the XSFLC criterion in pre-bent tube hydroforming required additional assumptions for multi-stage forming cases when the material was loaded along different axes or changed loading from compression to tension [58]. Those additional assumptions have not been validated or calibrated yet. For this reason, the pre-bent tube hydroforming failure predictions should be interpreted with caution. The straight tube hydroforming failure predictions required only the main assumption of the XSFLC method, which was validated. Therefore the failure predictions for straight tube hydroforming were more reliable.

The predicted and measured internal pressures at the onset of necking in pre-bent tube hydroforming are shown in Figure 122. The predicted internal pressure was extracted from the simulations for the failure locations corresponding to the experiments. Both upper and lower XSFLC limits over-predicted the measured tube internal pressure at the onset of necking. At the same time, the major trend of the increased internal pressure at the onset of necking with the increase in end-feed level was captured well by the XSFLC method for all three alloys.

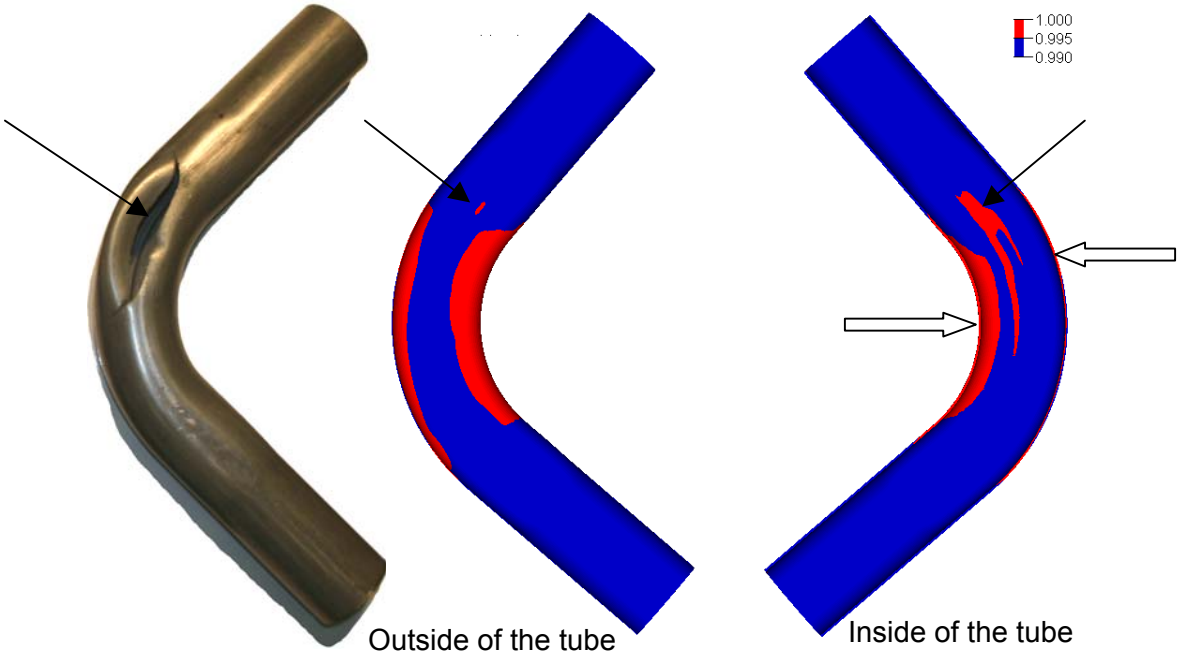

Figure 121: Experimental and numerical failure location prediction for hydroforming of pre-bent DP600 tube at zero end-feed

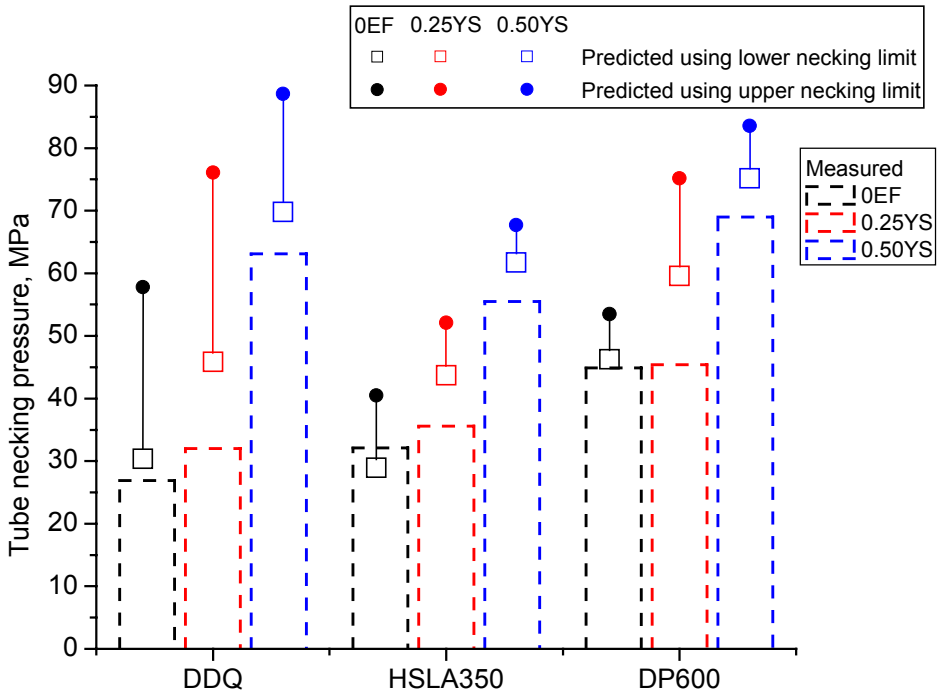

Figure 122: Measured and predicted internal pressure at the onset of necking for hydroforming of pre-bent DDQ, HSLA350 and DP600 tubes

Chapter 7
Discussion

7.1 Tube bending

The experiments and numerical simulations confirmed that the strength of the material had very little effect on the strain and thinning during tube bending for the alloys studied. This conclusion was in agreement with findings of Dyment [41] and Grantab [70], who showed that there was no effect of material strength on strain and thickness variations, while the severity of the bend, the geometry of the bend dies and bending boost significantly affected the strain and thickness in the bend. In the current research, all tubes had the same R/D ratio, thickness to diameter ratio and boost level of 100% and therefore the obtained strain and thickness distributions were virtually identical.

In the tube bending experiments, materials with higher strength required increased bend die torque and pressure die feed load to complete the bend. The mandrel load was primarily affected by the pressure die clamping load and friction between the mandrel and the inside of the tube. The predicted mandrel load in the FE simulations was also significantly affected by the coefficient of friction between the inside of the tube and the mandrel.

7.2 Tube hydroforming

The pre-bending operation significantly decreased the internal pressure at burst in the tube hydroforming experiments. The increase of end-feed load for both straight and pre-bent tube

hydroforming postponed failure, increased internal pressure and corner-fill expansion at burst, as shown in Figure 123 and Figure 124. A negative effect of excessive end-feed was detected in straight tube hydroforming: a high end-feed load significantly increased the internal pressure required to form small corner radii. Therefore sufficient levels of end-feed should be evaluated for each case of tube hydroforming, based on chosen loading schedule. In pre-bent tube hydroforming "negative corner-fill expansion" was observed due to earlier forming of the outside of the bend than the inside of the bend. Therefore in low end-feed level cases, when end-feed was unable to push enough material into the expanding zone, the tube failed before the initiation of the expansion of the inside of the bend. All of these findings were in accordance with the results obtained by Dyment [41] and Bardelcik [71].

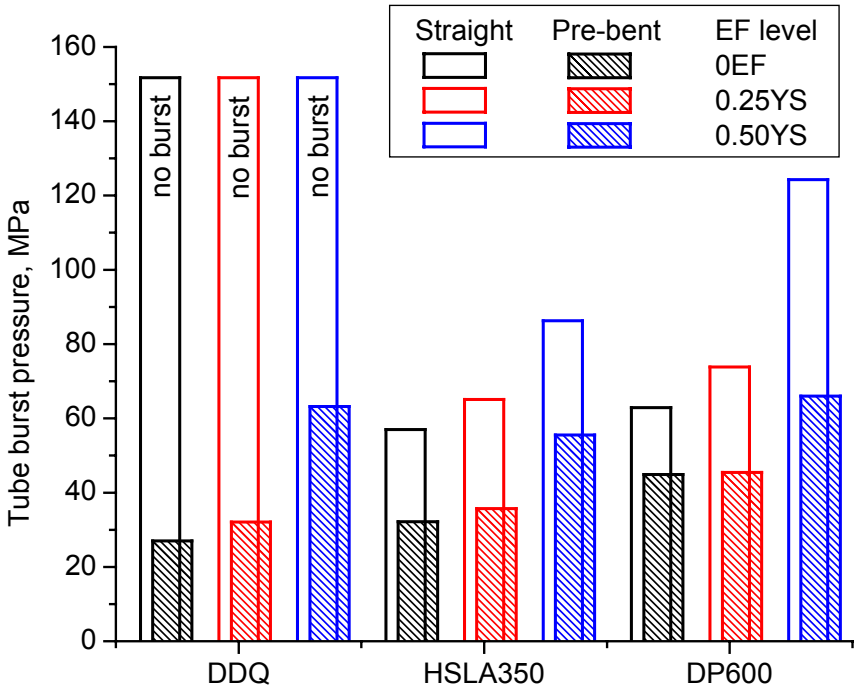

Figure 123: Measured tube burst pressure for straight versus pre-bent tube hydroforming

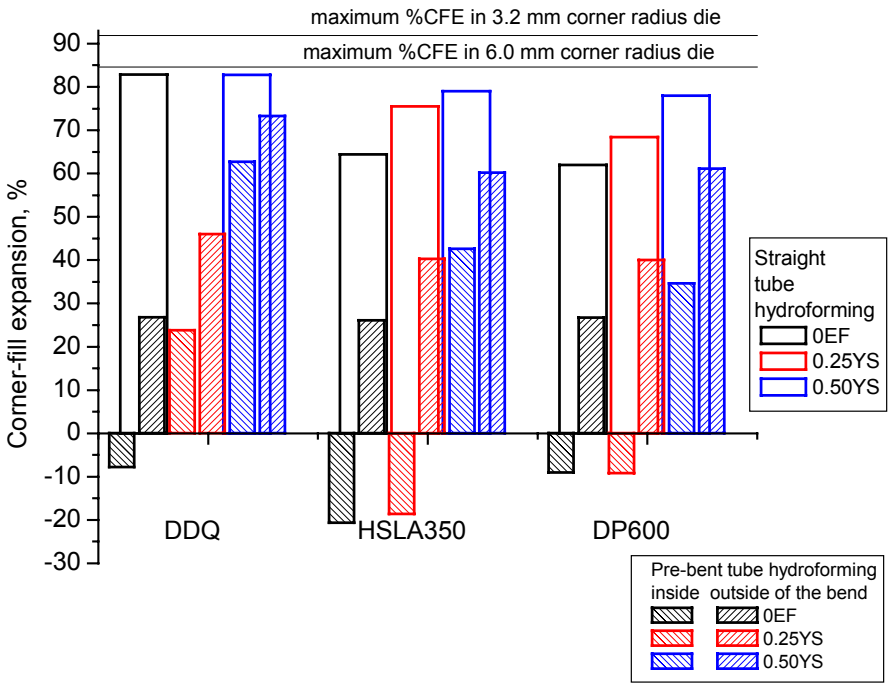

Figure 124: Measured tube corner-fill expansion at burst in straight versus pre-bent tube hydroforming

As suggested by Dwyer *et al.* [19], the results of tube free expansion tests were utilized to verify input stress-strain curves for the subsequent FE tube bending and hydroforming models. FE simulations of the tube free expansion test successfully predicted the experimental tube radial expansion, confirming the tube material properties obtained from uni-axial quasi-static tensile tests for all three alloys.

The straight tube hydroforming simulations enabled investigation of the effect of friction coefficient variation and comparison of the COF measured in TCT to that required for an accurate FE tube hydroforming model. The effect of COF between the tube and the hydroforming die was significant for tube end displacement, which allowed determination of the value of COF predicting accurate tube end displacement for each alloy and end-feed level. The tube corner-fill expansion versus pressure response appeared to be less sensitive to the variation of COF in straight tube hydroforming. Therefore, when validating numerical models, the predicted and experimental tube corner-fill expansion together with tube end displacement must be verified. Values of COF were selected for each alloy and then validated using tube end displacement, tube corner-fill expansion and strain and thickness distributions.

The results of the tube free expansion test were also utilized to estimate upper and lower limits for the tube strain-based FLC. The idea of tube strain-based FLC estimation using the results of tube free expansion test was expressed by Groche *et al.* [16,38]. In the current research, strain measurements at the onset of necking in interrupted tube free expansion tests with various amounts of end-feed were

unavailable. Therefore only lower and upper tube strain-based FLC limits were estimated. Those limits assumed the Keeler-Goodwin shape of the strain-based FLC [55,56]. Subsequent predictions of failure using upper and lower XSFLC estimates, obtained using the tube free expansion test results, were in a good agreement with the experimental results for straight tube hydroforming. For pre-bent tube hydroforming, additional work on calibration of additional assumptions in the XSFLC method should be conducted.

Failure prediction using the XSFLC method appeared to be very sensitive to the COF between the tube and the die. In the current work, values of COF were calculated for each case to enable accurate prediction of deformation (end-feed displacement) and strains. This, in turn, allowed accurate prediction of burst pressure and corner-fill expansion using the XSFLC method. Unfortunately, such an approach is not practical in the general case and a more rigorous method to capture COF in the FE models is desired.

Chapter 8
Conclusions

8.1 Conclusions

The following conclusions were made as a result of the current research:

- The pre-bending operation significantly decreased the tube corner-fill expansion and internal pressure at burst in pre-bent tube hydroforming compared to straight tube hydroforming;

- Application of end-feed load postponed failure, increased internal pressure and amount of tube corner-fill expansion at burst for both straight and pre-bent tube hydroforming. Excessive levels of end-feed, above 1.0YS, can lead to excessive thickening requiring very high pressure to form sharp corners, which can be undesirable;

- The finite element simulations accurately predicted the strain and thickness distributions in tube bending, as well as in the straight and pre-bent tube hydroforming operations;

- The XSFLC method provided quantitatively accurate predictions of the tube internal pressure at the onset of necking and the failure location for straight tube hydroforming. For pre-bent tube hydroforming, the predictions were qualitative in nature, predicting multiple necking locations. The method requires further development for multi-stage forming cases when the

material is loaded along different stress axes. The method did correctly capture the trends of the increase in tube internal pressure at the onset of necking with the increase of end-feed;

- The tube free expansion test was successfully utilized to confirm the tube material properties for further FE simulations and to estimate upper and lower bounds of the tube strain-based FLCs;

- The straight tube hydroforming simulations allowed investigation of the effect of COF and its relation to the values obtained from twist compression test.

8.2 Recommendations for future work

The following studies should be conducted in order to improve the obtained results:

- Interrupted tube free expansion tests with various amounts of end-feed should be conducted in order to obtain a measured strain-based FLC for tube materials that can be further transformed into the XSFLC;

- Further study should be conducted in order to investigate the correlation between measured COF between the tube and the die and the value of COF required for the contact algorithm within the FE tube hydroforming simulations;

- Optimization of the end-feed load versus internal pressure hydroforming schedule should be performed in order to further postpone failure and increase the tube corner-fill expansion

- Further study of the XSFLC method is required for multi-stage forming cases when the material is loaded along different stress axes.

References

1. Koc M., Advances in tube hydroforming – an enabling technology for low-mass vehicle manufacturing – material, lubrication, loading, simulation issues and alternatives, Tsinghua Science and technology, 9(5), 2004, pp. 527-545

2. Ahmetoglu M., Sutter K., Li X.J., Altan T., Tube hydroforming: current research, applications and need for training, J. of Materials Processing Technology, 98, 2000, pp. 224-231

3. Hwang Y., Altan T., Finite element analysis of tube hydroforming processes in a rectangular die, Finite element in analysis and design, 39, 2002, pp. 1071-1082

4. Zhang S., Developments in hydroforming, J. of Materials Processing Technology, 91, 1999, pp. 236-244

5. Ahmetoglu M., Altan T., Tube hydroforming: state-of-the-art and future trends, J. of Materials Processing Technology, 98, 2000, pp. 25-33

6. Xia Z.C., Failure analysis of tubular hydroforming, J. of Engineering Materials and Technology, 123, 2001, pp. 423-429

7. Koc M., Altan T., An overall review of the tube hydroforming (THF) technology, J. of Materials Processing Technology, 108, 2001, pp. 384-393

8. Koc M., Tribological issues in the tube hydroforming process – Selection of a lubricant for robust process conditions for an automotive structural frame part, ASME J. of Manufacturing Science and Engineering, 2003, 125 (3), pp. 484-492

9. Dohmann F., Hartl Ch., Tube hydroforming – research and practical applications, J. of Materials Processing Technology, 71, 1997, pp. 174-186

10. Koc. M., Aue-u-lan Y., Altan T., On the characteristics of tubular materials for hydroforming experimentation and analysis, Int. J. of Machine Tools & Manufacture, 41, 2001, pp. 761-772

11. Koc M., Investigation of the effect of loading path and variation in material properties on robustness of the tube hydroforming process, J. of Materials Processing Technology, 133, 2003, pp. 276-281

12. Dohmann F., Hartl Ch., Hydroforming – a method to manufacture light-weight parts, J. of Materials Processing Technology, 60, 1996, pp. 669-676

13. Dohmann F., Hartl Ch., Hydroforming – applications of coherent FE-simulations to the development of products and processes, J. of Materials Processing Technology, 150, 2004, pp. 18-24

14. Rimkus W., Bauer H., Mihsein M.J.A., Design of load-curves for hydroforming applications, J. of Materials Processing Technology, 108, 2000, pp. 97-105

15. Koc M., Allen T., Jirathearanat S., Altan T., The use of FEA and design of experiments to establish guidelines for simple hydroformed parts, Int. J. of Machine Tools and Manufacture, 40, 2000, pp. 2249-2266

16. Groche P., v. Breitenbach G., Steinheimer R., Investigation of the influence of the pre-hydroforming processes and development of characterization methods for the testing of steel semi-products for hydroforming, Proceedings of Tube Veracruz, 8.-10. October 2003, Veracruz, Mexico

17. Gao L., Motsch S., Strano M., Classification and analysis of tube hydroforming processes with respect to adaptive FEM simulations, J. of Materials Processing Technology, 129, 2002 pp. 261-267

18. Strano M., Jirathearanat S., Shr S., Altan T., Virtual process development in tube hydroforming, J. of Materials Processing Technology, 146, 2004, pp. 130-136

19. Dwyer N., Worswick M., Gholipour J., Xia C., Khodayari G., Pre-bending and subsequent hydroforming of tube: simulation and experiment, Proceedings of IBEC2003, Japan, October 2003

20. Dyment J., Worswick M.J., Normani F., Oliveira D., Khodayari G., Effect of endfeed on strains and thickness during bending and on the subsequent hydroformability of steel tubes, SAE Paper No. 2003-01-2837, 2003

21. Bardelcik A., Worswick M.J., The effect of element formulation on the prediction of boost in numerical tube bending, Proceedings of Numisheet 2005, pp. 775-780, 2005.

22. Bardelcik A., Worswick M.J., Numerical investigation into the effects of bending boost and hydroforming end-feed on the hydroformability of DP600 tube, 2005-01-0094, Proceedings of SAE 2005 Conference, 2005

23. Oliveira D.A., Worswick M.J., Grantab R., Effect of lubricant in mandrel-rotary draw tube bending of steel and aluminum, Canadian Metallurgical Quarterly, 44(1), 2205, pp. 71-78

24. Kridli G.T., Bao L., Mallick P.K., Yian Y., Investigation of thickness variation and corner filling in tube hydroforming, J. of Materials Processing Technology, 133, 2003, pp. 287-296

25. Trana K., Finite element simulation of the tube hydroforming process – bending, performing and hydroforming, J. of Materials Processing Technology, 127, 2002, pp. 401-408

26. Koc M., Altan T., Prediction of forming limits and parameters in the tube hydroforming processes, J. of Machine Tools & Manufacture, 42, 2002, pp. 123-138

27. Ahmed M., Hashmi M.S.J., Finite element analysis of bulge forming applying pressure and in-plane compressive load, J. of Materials Processing Technology, 77, 1998, pp. 95-102

28. Manabe K., Amino M., Effects of process parameters and material properties on deformation process in tube hydroforming, J. of Materials Processing Technology, 123 2002, pp. 285-291

29. Carleer B., van der Kevie G., de Winter L., van Veldhuizen B., Analysis of the effect of material properties on the hydroforming processes of tubes, J. of Materials Processing Technology, 104, 2000, pp. 158-166

30. Yang J., Jeon B., Oh S., The tube bending technology of a hydroforming process for an automotive part, J. of Materials Processing Technology, 111, 2001, pp. 175-181

31. Dwyer N., Worswick M., Gholipour J., Khodayari G., The effect of pre-bend on the tubular hydroforming of aluminium, Proceedings of IBEC2003, Japan, 2003

32. Gao L., Strano M., FEM analysis of tube pre-bending and hydroforming, J. of Materials Processing Technology, 151, 2004, pp. 294-297

33. Sokolwski T., Gerke K., Ahmetoglu M., Altan T., Evaluation of tube formability and material characteristics: hydraulic bulge testing of tubes, J. of Materials Processing Technology, 98, 2000, pp. 34-40

34. Strano M., Altan T., An inverse energy approach to determine the flow stress of tubular materials for hydroforming applications, J. of Materials Processing Technology, 146, 2004, pp. 92-96

35. Levy B.S., Van Tyne C.J., Strinfield J.M., Characterizing steel tube for hydroforming applications, J. of Materials Processing Technology, 150, 2004, pp. 280-289

36. Isadora van Riemsdijk and Bruce Farrand, Dofasco, Personal communication, 2005

37. v. Breitenbach G., Groche P., Steinheimer R., Investigation of the influence of the pre-hydroforming processes and development of characterization methods for the testing of steel semi-products for hydroforming, Presentation at Tube Veracruz, 8.-10. October 2003, Veracruz, Mexico

38. Groche P., v. Breitenbach G., Tubular semi-finished product characterisation and optimisation for tube hydroforming, Proceedings of International Conference on Innovations in Metal Forming 2004, 23-24 Sept. 2004, Brescia, Italy

39. v. Breitenbach G., Groche P., Tubular semi-finished product characterisation and optimisation for tube hydroforming, Prresentation at the International Conference on Innovations in Metal Forming 2004, 23-24 Sept. 2004, Brescia, Italy

40. Advanced high strength steel application guidelines, International Iron and Steel Institute, Committee on automotive applications, March 2005 (www.worldautosteel.org)

41. Dyment J.N., Effect of the Bending Process on Hydroformability of Steel Tubes, Master Thesis, University of Waterloo, 2004

42. Fuchizawa S., Narazaki M., Bulge test for determining stress-strain characteristics of thin tubes, Advanced technology of plasticity, Proceedings of the Fourth International Conference on Technology of Plasticity, Beijing, China, Septmeber 5-9 1993, pp. 488-493

43. Altan T., Aue-u-lan Y., Formability and flow stress determination by hydraulic bulge test, presentation, www.ercnsm.org

44. Li H.Y., Wang X.S., Yuan S.J., Miao Q.,B., Wang Z.R., Typical stress states of tube hydroforming and their distribution on the yield ellipse, J. of Materials Processing Technology, 151, 2004, pp. 345-349

45. Nedler J.A., Mead R., A simplex method for function minimization, Computer Journa, 7 (4), 1965, pp. 308-313

46. Stange R.R., Tube and pipe bending: principles, methods, tooling, techniques, developments, Tools for bending Inc., 1997

47. Inoue K., Mellor P.B., Radial draw bending of stainless steel tube, J. of Mechanical Working Technology, 3, 1979, pp. 151-166

48. Normani F.V., Analytical modeling of tube bending with hydroforming, Master Thesis, University of Waterloo, 2004

49. Kim S., KimY., Analytical study for tube hydroforming, J. of Materials Processing Technology, 128, 2002, pp. 232-239

50. Chu E., Xu Y., Hydroforming of aluminum extrusion tubes for automotive applications. Part I: buckling, wrinkling and bursting analyses of aluminum tubes, International Journal of Mechanical Sciences, 46, 2004, pp. 263–283

51. Chu E., Xu Y., Hydroforming of aluminum extrusion tubes for automotive applications. Part II: process window diagram, International Journal of Mechanical Sciences, 46, 2004, pp. 285–297

52. Chu E., Xu Y., Daxies R.W., Grant G.J., Failure predictions for aluminum tube hydroforming Processes, Proceedings of SAE2006, SAE Paper No. 2006-01-0543

53. Jirathearanat S., Hartl Ch., Altan T., Hydroforming of Y shapes – product and process design using FEA simulation and experiments, J. of Materials Processing Technology, 146, 2004, pp. 124-129

54. Chen K., Soldaat R.J., Moses R.M., Free Expansion Bulge Testing of Tubes For Automotive Hydroforming Applications, proceedings of SAE 2004 Conference, SAE Paper No. 2004-01-0832, 2004

55. Keeler S.P., Brazier W.G., Relationship between Laboratory Material Characterization and Press-Shop Formability, Proceedings of MicroAlloying75

56. Keeler S.P, On the origins of the FLD, Forming limit diagrams: concepts, methods and applications, 1989

57. Stoughton T.B., A general forming limit criterion for sheet metal forming, International Journal of Mechanical Sciences, 42, 2000, pp. 1-27

58. Simha C.H.M, Gholipour J., Bardelcik A., Worswick M.J., Prediction of Necking in Tubular Hydroforming Using an Extended Stress-Based Forming Limit Curve, in preparation

59. Simha, C.H.M., Gholipour, J., Bardelcik, A, Worswick M.J., Application of an Extended Stress-Based Flow Limit Curve to Predict Necking in Tubular Hydroforming, Proceedings of Numisheet 2005, 2005, pp. 551-516

60. Graf A., Hosford W., Effect of changing strain paths on forming limit diagrams of Al 2008-T4, Metallurgical transactions A, 24A, 1993, pp. 2503-2512

61. Ghosh A.K., Laukomis J.V., The influence of strain-path changes on the formability of sheet steel. 9th Biennial Congress of the International Deep Drawing Research Group, Sheet Metal Forming and Energy Conservation, ASM Publication, 1976

62. Simha C.H.M., Grantab R., Worswick M.J., Computational analysis of stress-based forming limit curve, in preparation

63. Ozturk F., Lee D., Experimental and numerical analysis of out-of-plane formability test, J. of Material Processing Technology, 170, 2005, pp. 247-253

64. Green, D. and Stoughton, T. B.: Evaluation of hydroforming severity using stress-based forming limits. In 2nd annual North American hydroforming conference and exhibition, 2004.

65. Maciniak Z., Duncan J.L., Hu S.J., Mechanics of sheet metal forming, Butterworth-Heinemann, 2002

66. Chen K., The bulge of tubes and a failure criterion for tube hydroforming, proceedings of SAE 2001 Conference, SAE Paper No. 2001-01-1132, 2001

67. Chen K., A bursting failure criterion for tube hydroforming, 2002-01-0794, proceedings of SAE 2002 Conference, 2002

68. Bardelcik, A., Worswick, M.J., Evaluation of load control end-feed in hydroforming of pre-bent DP600 steel tube using the extended stress-based forming limit curve failure criterion, J. of Computational and Applied Mechanics, 5, 2004, pp.1-9

69. Hallquist J. O., LS-DYNA Keyword Users Manual, Version 970, 2003

70. Grantab R., Interaction Between Forming and Crashworthiness of Advanced High Strength Steel S-Rails, Master Thesis, University of Waterloo, 2006

71. Bardelcik A., Effect of pre-bending and hydroforming parameters on the formability of advanced high strength steel tubes, Master Thesis, University of Waterloo, 2006